

1989

# The interaction of small oxygenated fluorocarbons and hydrocarbons with the Ru(001) surface

Mary Margaret Walczak  
*Iowa State University*

Follow this and additional works at: <https://lib.dr.iastate.edu/rtd>

 Part of the [Physical Chemistry Commons](#)

## Recommended Citation

Walczak, Mary Margaret, "The interaction of small oxygenated fluorocarbons and hydrocarbons with the Ru(001) surface " (1989).  
*Retrospective Theses and Dissertations*. 9249.  
<https://lib.dr.iastate.edu/rtd/9249>

This Dissertation is brought to you for free and open access by the Iowa State University Capstones, Theses and Dissertations at Iowa State University Digital Repository. It has been accepted for inclusion in Retrospective Theses and Dissertations by an authorized administrator of Iowa State University Digital Repository. For more information, please contact [digirep@iastate.edu](mailto:digirep@iastate.edu).

## INFORMATION TO USERS

The most advanced technology has been used to photograph and reproduce this manuscript from the microfilm master. UMI films the text directly from the original or copy submitted. Thus, some thesis and dissertation copies are in typewriter face, while others may be from any type of computer printer.

The quality of this reproduction is dependent upon the quality of the copy submitted. Broken or indistinct print, colored or poor quality illustrations and photographs, print bleedthrough, substandard margins, and improper alignment can adversely affect reproduction.

In the unlikely event that the author did not send UMI a complete manuscript and there are missing pages, these will be noted. Also, if unauthorized copyright material had to be removed, a note will indicate the deletion.

Oversize materials (e.g., maps, drawings, charts) are reproduced by sectioning the original, beginning at the upper left-hand corner and continuing from left to right in equal sections with small overlaps. Each original is also photographed in one exposure and is included in reduced form at the back of the book. These are also available as one exposure on a standard 35mm slide or as a 17" x 23" black and white photographic print for an additional charge.

Photographs included in the original manuscript have been reproduced xerographically in this copy. Higher quality 6" x 9" black and white photographic prints are available for any photographs or illustrations appearing in this copy for an additional charge. Contact UMI directly to order.

# U·M·I

University Microfilms International  
A Bell & Howell Information Company  
300 North Zeeb Road, Ann Arbor, MI 48106-1346 USA  
313/761-4700 800/521-0600



Order Number 8920194

**The interaction of small oxygenated fluorocarbons and  
hydrocarbons with the Ru(001) surface**

Walczak, Mary Margaret, Ph.D.

Iowa State University, 1989

**U·M·I**

300 N. Zeeb Rd.  
Ann Arbor, MI 48106

---



The interaction of small oxygenated fluorocarbons and  
hydrocarbons with the Ru(001) surface

by

Mary Margaret Walczak

A Dissertation Submitted to the  
Graduate Faculty in Partial Fulfillment of the  
Requirements for the Degree of  
DOCTOR OF PHILOSOPHY

Department: Chemistry

Major: Physical Chemistry

**Approved:**

Signature was redacted for privacy.

**In Charge of Major Work**

Signature was redacted for privacy.

**For the Major Department**

Signature was redacted for privacy.

**For the Graduate College**

Iowa State University  
Ames, Iowa  
1989

## TABLE OF CONTENTS

	Page
DEDICATION	iii
GENERAL INTRODUCTION	1
PAPER I: OXYGENATED FLUOROCARBONS ADSORBED AT METAL SURFACES: CHEMISORPTION BOND STRENGTHS AND DECOMPOSITION	6
PAPER II: THE BONDING OF FLUORINATED AND HYDROGENATED DIETHERS TO RU(001)	47
PAPER III: CYCLIC ETHERS ADSORBED ON Ru(001): CHEMISORBED AND METASTABLE ADSORPTION STATES	104
CONCLUSIONS	139
REFERENCES	142
APPENDIX A: A COMPUTER PROGRAM FOR THERMAL DESORPTION EXPERIMENTS	145
APPENDIX B: THE INTERACTION OF $\text{NF}_3$ WITH RU(001): ORDER AT STEPS	179
ACKNOWLEDGEMENTS	211

DEDICATION

To my parents,  
Michael and Agathe Selner



## GENERAL INTRODUCTION

Tribology involves the study of the interaction between two surfaces in relative motion with or without intervening lubricating material. The field of tribology is directly relevant to all areas in which surfaces interact mechanically, such as computer technology, mechanical engineering and aerospace engineering. Until now, tribological studies have mainly involved the measurement of friction, wear and related quantities [1-3]. However, since tribology involves the study of interacting surfaces, information from surface science measurements should also be able to make major contributions to the field.

Surface science techniques were first applied to tribology by Buckley [4,5]. Buckley and coworkers Pepper, Miyoshi, Yamamoto and Rengstorff have used Low Energy Electron Diffraction (LEED) [4], Auger Electron Spectroscopy (AES) [6-16] and X-ray Photoelectron Spectroscopy (XPS) [14-17] to study the interaction of two surfaces in contact under vacuum conditions. Two general observations are made in their work. In some studies [4,6,11-13,15], AES detects the transfer of material between surfaces during sliding experiments. Other studies [7-10,14-17] determine the effects of intentionally-introduced impurities, such as oxygen, hydrocarbons or halocarbons, on the frictional characteristics of the sliding surfaces. In the presence of halocarbons [7,8,10], the coefficient of friction is 20% to 35% lower than for the clean surfaces. This result is not surprising since perfluorinated polyethers, such as

Krytox [18], Demnum [19] and Fomblin [20] are widely used as industrial lubricants.

The attractive properties of these polymeric lubricants are their oxidative and thermal stability [21-30]. In the presence of titanium or aluminum surfaces these polymers are effective lubricants up to 590 K in an oxidizing atmosphere [21,22]. The addition of phosphorous-containing stabilizers, such as perfluoroalkyl ether substituted perfluorophenyl phosphine, is found to inhibit the degradation rate of the lubricant [21,22]. Alternatively, thermal oxidative pretreatment to remove the part of the lubricant which is responsible for the degradation results in better thermal stability in the presence of alloys [23,24]. Understanding the interaction between lubricant molecules and surfaces may allow custom-tailoring of lubricants for specific applications.

One application where perfluorinated polyethers are used is in the lubrication of computer disks. In operation, the disk is read by a "head" that is nominally 5  $\mu\text{m}$  away from the disk surface. In conventional disk drives, the head "floats" above the disk on a cushion of air. Disk "crashes" (i.e., physical contact between the disk and the head) primarily occur during power-up and -down procedures because the air flow stops as the disk stops spinning. Perfluorinated, polymeric ether lubricants are coated on the disk to prevent disk destruction by the head, especially during start and stop procedures.

Lubricant molecules must bond strongly to the substrate to avoid being swept off the disk under the influence of centrifugal force caused

by disk rotation. A fourteen inch disk, for instance, typically rotates at 3600 rpm during operation. As a crude approximation, a 10,000 amu polymer molecule at the edge of this disk must be bound by at least 22 kJ/mol to stay in place on the rotating disk. More precisely, the molecule must have a bond component parallel to the plane of rotation which is at least 22 kJ/mol. The lubricant molecules must also be stable under the operating conditions of the disk. Often, a ketone, ester, alcohol or aromatic group is synthesized at the end of the perfluoroether polymeric chain to "anchor" the lubricant molecule to the surface.

The purpose of this dissertation is to use surface science techniques to understand the adhesion and thermal stability of perfluorinated lubricants. We want to answer fundamental questions about the lubricant-surface interaction: How strongly do prototypical lubricant molecules bond to surfaces? Which functional groups bond? Does the molecule decompose? What are the decomposition products and how do they interact with the surface? To break this complex problem into a realistic experimental system, we make two simplifications. First, we model the polymeric lubricant with small ether or ketone molecules; second we model the complex disk surface with a well characterized single crystal surface of a metal.

In the past, surface science was used extensively in heterogeneous catalysis studies. As a result, a large body of information has been compiled regarding the interaction of oxygenated hydrocarbons with surfaces. The bonding of hydrogenated ethers and ketones to surfaces,

for example, is fairly well understood [31-37]. However, only two studies of the interaction between oxygenated fluorocarbons and surfaces are reported in the literature [38,39]. Avery reports that hexafluoroacetone molecules bond more weakly to Pt(111) than the hydrogenated analog, acetone [38]. Ng et al. [39] compare the adsorption of dimethyl ether and a partially fluorinated analog,  $(CF_2H)_2O$ , on an aluminum oxide surface. In this case as well, the fluorinated molecule bonds more weakly to the surface than the hydrogenated analog. As a result of the lack of information regarding the surface chemistry of oxygenated fluorocarbons, our study involves comparison between the surface chemistry of oxygenated fluorocarbons and analogous oxygenated hydrocarbons.

This dissertation describes a study of the adsorption and desorption of both fluorinated and hydrogenated ethers and ketones on the Ru(001) surface. Ethers are models of the polymeric "backbone" of the lubricant; ketones are models of a particular kind of anchoring end-group. The Ru(001) surface is selected due to the wealth of information regarding the interaction of oxygenated hydrocarbons with this atomically smooth substrate [34,36,37,40]. Acetone, in particular, has been well characterized on this surface [34]. The information available regarding the surface chemistry of oxygenated hydrocarbons on Ru(001), therefore, serves as a starting point for the studies of oxygenated fluorocarbons.

### Explanation of Dissertation Format

This dissertation is arranged according to the alternate style format. Three papers are included. Paper I, "Oxygenated Fluorocarbons Adsorbed at Metal Surfaces: Chemisorption Bond Strengths and Decomposition", appears in volume 109 of the Journal of the American Chemical Society on pages 5621-5627, 1987. Paper II, "The Bonding of Fluorinated and Hydrogenated Diethers to Ru(001)", is submitted to Surface Science. Paper III, "Cyclic Ethers Adsorbed on Ru(001): Chemisorbed and Metastable Adsorption States", will be submitted to Surface Science.

PAPER I:

OXYGENATED FLUOROCARBONS ADSORBED AT METAL SURFACES:  
CHEMISORPTION BOND STRENGTHS AND DECOMPOSITION

OXYGENATED FLUOROCARBONS ADSORBED AT METAL SURFACES:  
CHEMISORPTION BOND STRENGTHS AND DECOMPOSITION

M. M. Walczak, P. K. Leavitt and P. A. Thiel

Department of Chemistry and Ames Laboratory  
Iowa State University  
Ames, Iowa 50011

## ABSTRACT

We report studies of the adsorption bond strengths and decomposition of perfluorodiethyl ether and hexafluoroacetone on clean and oxygen-dosed Ru(001). Perfluorodiethyl ether bonds weakly to Ru(001) (42-43 kJ/mol) without decomposing. This binding energy is typical for a metal-adsorbate interaction in which the adsorbate donates electrons to the metal from the oxygen lone pair. Hexafluoroacetone bonds to the surface in both a weakly bonded configuration (37-38 kJ/mol) and a strongly bonded configuration (57-87 kJ/mol), and there is insignificant decomposition. We compare the chemistry of these oxygenated fluorocarbons to analogous oxygenated hydrocarbons. We propose that the net effect of fluorination is to weaken those chemisorption bonds which rely upon electron donation from the oxygen lone pairs to the metal, but to strengthen the chemisorption bonds which rely primarily upon electron donation from the metal into antibonding C-O orbitals. Both phenomena can be explained by electronic effects resulting from fluorination.



## I. INTRODUCTION

Adhesion and thermal stability of common lubricants, such as fluorinated polymeric ethers, at surfaces are not understood on a molecular scale. Important questions remain to be addressed at a fundamental level: How strongly is the molecule bonded to the surface? Which functional groups of the molecule bond? Does the molecule decompose? What are the decomposition products, and how do they interact with the surface? We have studied the adsorption and decomposition of simple oxygenated fluorocarbons at a metal surface, Ru(001), as part of a larger effort to understand the answers to these questions. We have chosen oxygenated molecules for which the surface chemistry of the nonfluorinated analogs is already well understood in order to determine the way in which substitution of fluorine for hydrogen changes adsorption bond strengths and decomposition pathways.

It is well-established that simple, oxygen-containing organic molecules form bonds to transition-metal centers (including surfaces) via the oxygen-containing functional group. However, the mechanism of the interaction depends largely on whether the C-O bond is saturated or unsaturated. In molecules which contain saturated C-O bonds, such as ethers and alcohols (or, by analogy, water), a weak bond to the surface is formed by electron donation from an oxygen lone pair to the metal [1-4]. Such an interaction typically contributes 40 kJ/mol to the chemisorption bond [2-4]. Fluorination may be expected to weaken the

metal-oxygen bond of a molecule such as an ether by inductively depleting electron density at the oxygen lone pairs.

Molecules which contain unsaturated carbon-oxygen bonds, e.g. ketones and aldehydes, exhibit two types of bonding to metals,  $\eta^1$  and  $\eta^2$ . The first involves electron donation from oxygen lone pairs ( $sp^2$  orbitals) to the metal, similar to the case for saturated C-O bonds. In this configuration, the molecule is tilted with an M-O-C angle (M = metal center of metal surface) of about  $150^\circ$  [5]. The bond to the surface is weak and comparable in magnitude to those formed by the ethers:  $34 \pm 3$  kJ/mol for  $\eta^1(O)$ -methanal (hereafter referred to as formaldehyde) on Ru(001) [6], 47-52 kJ/mol for  $\eta^1(O)$ -propanone (hereafter referred to as acetone) on Ru(001) [7; present work], and 49 kJ/mol for  $\eta^1(O)$ -acetone on Pt(111) [8,9]. Fluorination is expected to weaken this bond, and indeed, Avery reports a chemisorption bond of 35 kJ/mol for  $\eta^1(O)$ -1,1,1,3,3,3-hexafluoropropanone (hereafter referred to as hexafluoroacetone) on Pt(111) [10], lower by 12-17 kJ/mol than for the nonfluorinated molecule. These values are summarized in Table 1.

The second possible configuration is one in which the molecule bonds with the C=O bond more nearly parallel to the metal surface, or with C and O atoms nearly equidistant from a metal center. This bonding configuration can be understood through the Chatt-Dewar-Duncanson model of hydrocarbon bonding, in which an unsaturated hydrocarbon donates electron density into vacant metal orbitals while the metal backbonds into geometrically and energetically accessible antibonding orbitals.

Table 1. Desorption characteristics of  $\eta^1$ - and  $\eta^2$ - carbonyls on metal surfaces

Molecule	Substrate	Coordination	$T_p$ , K	$E_d$ , kJ/mol	Thermal Decomposition	Reference
$(CH_3)_2CO$	Pt(111)	$\eta^1$ (majority)	185	49 <sup>a</sup>	none	8
$(CF_3)_2CO$	Pt(111)	$\eta^1$ (majority)	135	35 <sup>a</sup>	none	10
$(CH_3)_2CO$	Ru(001)	$\eta^1$ (minority)	200-400	42-62 <sup>a</sup>	none	7
			195-210	48-52 <sup>b</sup>	none	present work
$(CH_3)_2CO$	O/Ru(001)	$\eta^1$ (minority)	200-450	42-79 <sup>a</sup>	none	7
$(CF_3)_2CO$	Ru(001)	( $\alpha_2$ )	157	38 <sup>b</sup>		present work
$H_2CP$	Ru(001)	$\eta^1$ (minority)	130-155	31-37 <sup>a</sup>	none	6
$H_2CO$	O/Ru(001)	$\eta^1$ (majority)	130-155	31-37 <sup>a</sup>	none	6
$(CH_3)_2CO$	Pt(111)	$\eta^2$ (minority)	220-240	58-64 <sup>b</sup>	extensive	8
$(CH_3)_2CO$	Ru(001)	$\eta^2$ (majority)	---		extensive	7
$(CH_3)_2CO$	O/Ru(001)	$\eta^2$ (minority)	---		extensive	7
$(CH_3)_2CO$	Ru(001)	( $\alpha_1$ )	346	87 <sup>b</sup>		present work
$H_2CO$	Ru(001)	$\eta^2$ (majority)	275	67 <sup>a</sup>	extensive	6

<sup>a</sup>Taken from literature reference cited.

<sup>b</sup>Calculated from  $T_p$  according to Ref. 17, assuming  $\nu = 10^{13} \text{ s}^{-1}$  and simple first-order kinetics.

Overlap between the metal orbitals and the carbonyl group's low-lying, vacant  $\pi^*$  orbital is maximized by a  $\eta^2$ -geometry. In short, the observation of  $\eta^2$ -carbonyl means that backbonding into  $\pi^*$  orbitals is a major component of the metal-carbonyl bond. Consequently, C=O vibrational stretching frequencies are lower and C=O equilibrium bond lengths are longer for  $\eta^2$ -carbonyl than for  $\eta^1$ -carbonyl [e.g., 6-13], indicative of a weaker C=O bond in the former case.

A saturated molecule, such as an ether, does not have empty low-lying orbitals which can accept backdonation from the metal, so the  $\eta^2$ -form is not observed for ethers. In molecules which contain carbonyl groups, both  $\eta^1$ - and  $\eta^2$ -bonds can form. The  $\eta^2$ -bond is favored over  $\eta^1$  by electropositive metal centers and/or electron-withdrawing groups adjacent to the carbonyl, such as fluorine [6-13]. These two factors presumably favor  $\eta^2$ -bonds due to a relative lowering of the carbonyl  $\pi^*$  orbital acceptor energy levels on fluorination [14] providing a better match to the energy levels of the metal donor orbitals. This picture is supported by the work of Deffeyes et al. [15,16], who have studied adsorption of propene and 3,3,3-trifluoropropene on oxygen-dosed Mo(100). They find that the fluorinated molecule is more strongly bound by about 11 kJ/mol, which they attribute to enhancement of backdonation from the metal into the  $\pi^*$  C=C bond of the undissociated molecule [15,16].

On metal surfaces,  $\eta^2$ -carbonyls tend to decompose via C-H or C-C bond cleavage rather than desorb [6-9], but there is one report that  $\eta^2(\text{C},\text{O})$ -acetone desorbs intact from Pt(111) at 220-240 K [8], which

corresponds to a chemisorption bond of  $61 \pm 3$  kJ/mol [17]. This is 12 kJ/mol higher than for  $\eta^1(0)$ -acetone on the same surface, consistent with the idea that  $\eta^2$ -coordination provides a stronger bond with the metal than  $\eta^1$  (see Table 1).

In addition to the metal-oxygen bond, there appears to be a weak attractive interaction between hydrocarbon groups and the surface. Sexton and coworkers have shown that the desorption energy of chemisorbed ethers, alcohols, and alkanes on Cu and Pt surfaces is proportional to the number of carbon atoms in the aliphatic portion of the molecule [2,3]. As the hydrocarbon chain length increases, desorption energy increases (and is reflected by an increase in desorption peak temperature) because the metal can interact favorably with more  $\text{CH}_2$  groups. Sexton and Hughes have shown that this interaction contributes 5 to 6.5 kJ/mol per  $\text{CH}_2$  group for ethers adsorbed on Pt(111) [2]. A similar phenomenon has been observed for saturated cyclic hydrocarbons adsorbed on Ru(001), where desorption energy increases linearly with the number of  $\text{CH}_2$  groups [18,19]. Hoffmann and Upton report that this interaction is not attributable to hydrogen bonding between the hydrocarbon and the metal, but rather due to a more complex interaction with several opposing components [19]. The net interaction is probably less favorable for a  $\text{CF}_2$  group than for a  $\text{CH}_2$  group, partly because the C-F bond is longer than the C-H bond (1.32 Å in  $\text{C}_2\text{F}_6$  vs. 1.10 Å in  $\text{C}_2\text{H}_6$  [20]), and partly because fluorine is more electron-rich than hydrogen

[21]. The carbon is held farther away from the surface by the first factor; fluorine-metal repulsion is important due to the second factor.

In the case of a  $\eta^2$ -carbonyl there is an additional factor to consider: on an atomically flat metal surface, the  $\eta^2$ -geometry requires either that the aliphatic portions of the molecule approach the metal surface closely, or else that there is some rehybridization about the acyl carbon. The latter is believed to take place in  $\eta^2(\text{C},\text{O})$ -acetone on Ru(001) [7]. As described above, we expect that it is more difficult for a bulky fluorinated aliphatic group to approach a metal surface than for a hydrogenated group. In turn, this may require that the carbonyl carbon atom rehybridize for a  $\eta^2$ -molecule to keep the fluorinated aliphatic groups away from the surface. Alternatively, an  $\eta^2$ -configuration may be entirely prevented for a fluorinated molecule. Indeed, Avery observes that  $\eta^1$ -coordination predominates for hexafluoroacetone on Pt(111) [10] even though fluorination is known to favor  $\eta^2$ -coordination in inorganic complexes of hexafluoroacetone [12]. This may represent the effect of steric hindrance.

In summary, a fluorinated ether is expected to bind more weakly to a transition metal surface than its nonfluorinated analog, because fluorination weakens both the oxygen-metal interaction and the carbon-metal interaction. A fluorinated carbonyl may bind more or less strongly to a metal surface, depending upon which of two coordinations is adopted: Repulsive interactions between the bulky fluorocarbon chain(s) and the metal may force the molecule into the  $\eta^1$ -form, even though

inductive electron withdrawal from the carbonyl group favors  $\eta^2$ -coordination. In the former case, a  $\eta^1$ -bond is expected to be weaker for the fluorocarbon than for the hydrocarbon, but a  $\eta^2$ -bond (if formed) should be stronger when the same comparison is made, and may lead to decomposition of the molecule [Z-9]. The purpose of the present work is to test these hypotheses.

We find that the chemisorption bond of 1,1'-oxybis(perfluoroethane) (hereafter referred to as perfluorodiethyl ether) on Ru(001) is relatively weak, as expected (42-43 kJ/mol). Less than 0.02 monolayer of both perfluorodiethyl ether and hexafluoroacetone decompose. The chemisorbed hexafluoroacetone molecules desorb from several states. One with relatively high binding energy, 87 kJ/mol, is suppressed by co-adsorbed oxygen. These findings suggest a  $\eta^2$ -coordination within the first layer.

## II. EXPERIMENTAL PROCEDURES

The experiments are performed in two stainless steel UHV chambers with base pressures of  $4 \times 10^{-10}$  Torr and  $1 \times 10^{-10}$  Torr. Both chambers are equipped with a mass spectrometer, an ion gun and gas inlet manifold. One chamber is also equipped with an Auger spectrometer. The two Ru(001) samples, about  $1 \text{ cm}^2$  in area, are grown at the Ames Laboratory Materials Preparation Center. They are oriented and polished to within  $1^\circ$  of the (001) face on both sides. The initial crystal cleaning procedure in vacuum includes successive heating, ion bombardment and oxidation cycling [22]. The sample cleanliness is checked by measuring the thermal desorption spectrum of CO following oxygen exposure, and by Auger electron spectroscopy (AES). Two 0.020 inch diameter Ta wires are spotwelded to the edges of the sample. The Ta wires are attached to a liquid-nitrogen-coolable coldfinger and are used to resistively heat the sample [23]. The crystal temperature is measured with a W-5% Re vs. W-26% Re thermocouple spotwelded to the edge of the sample. The sample can be cooled from 1600 K to 90 K in five minutes.

The oxygenated hydrocarbons used in this study, acetone and 1,1'-oxybisethane (hereafter referred to as diethyl ether), are reagent grade. The acetone, from Mallinckrodt, is specified as 99.88% pure. The anhydrous diethyl ether, from Fisher Scientific, is specified as 99.9% pure. These compounds are further purified by repeated freeze-pump-thaw cycles on the gas-handling manifold. After three freeze-pump-thaw cycles



the diethyl ether is determined by gas chromatography mass spectrometry to be 100% pure.

The oxygenated fluorocarbons are purchased from Strem Chemical Co. The vendor specifies that the ether is 98% pure and the hexafluoroacetone is at least 97% pure; these chemicals are used without further purification. A mass spectrum of each compound is obtained *in situ* and compared with a reference spectrum to check for decomposition in the stainless steel gas handling lines. The mass spectrum of perfluorodiethyl ether is not available in the literature. Therefore, it is measured independently using a Kratos MS50TC magnetic sector mass spectrometer, and is shown in Figure 1. A hexafluoroacetone mass spectrum is also obtained on the Kratos system and compared with a published spectrum [24]. Upon comparison, the *in situ* spectra show no evidence for decomposition of any of the fluorocarbons in the gas lines.

Special safety precautions are deemed necessary for handling these gases. Hexafluoroacetone, for instance, is "highly toxic by inhalation", with human tolerance reported to be 0.1 ppm in air [25]. (Specific toxicity data is not available for the fluorinated ether.) Within the gas manifold, most of the volume is evacuated by condensation into a liquid nitrogen trap, followed by evaporation of the trap contents into a hood; mechanical pump exhausts are also vented into the hood. The manifold and the venting system are tested for leaks by purging with H<sub>2</sub>S. The human nose is sensitive to H<sub>2</sub>S at levels of 0.03 ppm [26], below the tolerance level of hexafluoroacetone. The absence of detectable odor

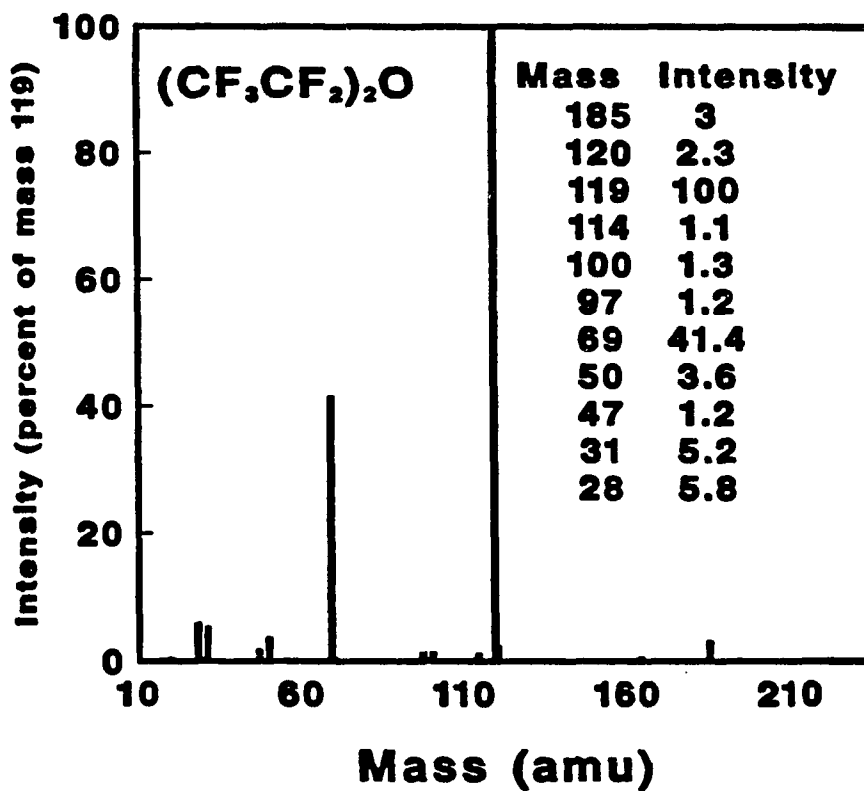


Figure 1. Mass spectrum of perfluorodiethyl ether

Electron energy is 70 eV; accelerating voltage is 8 kV.

during the test is therefore taken as evidence that fluorocarbons cannot escape at a rate sufficient to build up toxic levels. [There is no consequent evidence for sulfur contamination in the gas manifold following this procedure.]

The oxygenated fluorocarbons and hydrocarbons are introduced into the UHV chamber via a directed capillary array doser. The exposure units reported are Langmuir (L,  $1 \text{ L} \equiv 10^{-6} \text{ Torr*s}$ ), arrived at by comparing exposures of CO through the doser with exposures from backfilling the chamber and correcting for relative molecular weight of CO and the gases in the study.

Between experiments the sample is cleaned by heating to 1300 K in  $5 \times 10^{-8} \text{ Torr O}_2$  or by exposing the sample repeatedly to 5 L  $\text{O}_2$  and monitoring mass 28 ( $\text{CO}^+$ ) as the sample is heated. It is then flashed in vacuum and held for 30 seconds at 1600 K to desorb remaining oxygen. The high-temperature anneal is repeated until no oxygen Auger signal is seen. The sample is cooled to 90 K prior to each exposure to a fluorinated gas. Thermal desorption measurements are taken using an EAI Quad 150 mass spectrometer interfaced to a Commodore 64 computer or a PDP-11/23 computer. The computer program used for data acquisition with the PDP-11/23 computer is described in Appendix A of this dissertation. The spectrometer ionizer is in direct line-of-sight with the sample and about 10 cm removed. The computer allows (effectively) simultaneous detection of up to four masses (eight masses for the PDP-11/23) as a function of time and temperature. The sample temperature is controlled by a feedback

circuit described previously by Herz et al. [27]. The sample heating rate varies between 12 and 6 K/s for the ketones and between 2.6 and 1.9 K/s for the ethers.

The extent of decomposition of the organic molecules is measured by monitoring CO desorption (28 amu) and, for the hydrogenated compounds, H<sub>2</sub> desorption (2 amu) during each thermal desorption experiment. These areas are compared with those which result from saturation of the surface with CO or H<sub>2</sub>, and are also corrected for adsorption of background CO or H<sub>2</sub>. The area which results from a saturation coverage of CO or H<sub>2</sub> is known to represent an absolute coverage of 0.67 monolayers [22] or 2 monolayers [28,29], respectively. For each experiment with the organic molecules, the small area attributable to adsorption from the background is subtracted from the total area of the CO or H<sub>2</sub> desorption peak. Our detection limit for decomposition products is 0.02 and 0.3 monolayers for CO and H<sub>2</sub>, respectively. These values correspond to the surface coverage of CO or H<sub>2</sub> when the thermal desorption peak intensity is three times the noise intensity, and this is used to calibrate all other decomposition peak areas.

We adopt the following nomenclature: Desorption states which represent molecules measurably influenced by the metal surface (i.e., resolved from the bulk-like multilayer) are labelled  $\alpha$  (majority state) or  $\beta$  (minority state), with a numerical subscript which corresponds to the sequence of population with increasing exposure. Desorption states

which represent sublimation from bulk-like multilayers are labelled  $\gamma$ . Peak temperatures in the text and Figures are rounded to the nearest 5 K.

In some cases, the thermal desorption spectra of the fluorinated compounds are quite difficult to reproduce, particularly the high-temperature states. In order to distinguish questionable states from possible experimental artifacts, such as desorption from heating wires or desorption from the back side of the crystal, the following experiments are done. The Auger spectrum of the clean sample is recorded, showing no detectable oxygen. The Ru sample is then cooled to 90 K, exposed to the fluorinated gas, and heated to a temperature which stops short of desorbing the state in question. The O/Ru Auger peak ratio is recorded. The entire sequence is then repeated, except that the thermal ramp is stopped after the questionable state has desorbed, and an Auger spectrum is again measured. In this way, we have shown that the  $\alpha_1$ -state of hexafluoroacetone is indeed due to desorption from the Ru(001) surface. The difficult reproducibility is most probably due to occasional inadequate cleaning procedures, specifically incomplete oxygen removal.

### III. RESULTS

#### A. Perfluorodiethyl Ether

Thermal desorption spectra following adsorption of perfluorodiethyl ether,  $(\text{CF}_3\text{CF}_2)_2\text{O}$ , at 90 K on Ru(001) are shown in Figure 2. The spectra are obtained by monitoring mass 69,  $\text{CF}_3^+$ , an intense molecular fragment, as a function of temperature. At low exposures a state at 165 K, which we denote  $\alpha_1$ , is observed. As exposure increases a second state at 130 K,  $\gamma$ , begins to fill. The  $\gamma$ -state does not saturate with increasing exposure.

The  $\alpha_1$ -state displays some of the features characteristic of simple first-order desorption kinetics [17]: the peak temperature of  $165 \pm 2$  K and the peak full-width at half-maximum (FWHM) of  $7 \pm 1$  K are invariant with coverage, within the stated experimental error. We thus assume first order kinetics, although the highly asymmetric peak shape of the  $\alpha_1$ -state suggests a reaction order less than unity. We interpret the  $\alpha_1$ -state to represent molecular desorption from a chemisorbed layer. Assuming a pre-exponential factor  $\nu$  of  $10^{13} \text{ s}^{-1}$  [17], the peak temperature of  $165 \pm 2$  K corresponds to a desorption barrier ( $E_d$ ) of 42-43 kJ/mol.

The inability to saturate the  $\gamma$ -state at high exposures indicates that this state is due to bulk sublimation. An Arrhenius plot of  $\ln(\text{Intensity})$  vs.  $1/T$  of the leading edge of the  $\gamma$ -peak at high coverage, shown in Figure 3, yields a value for the heat of sublimation ( $E_s$ ) of

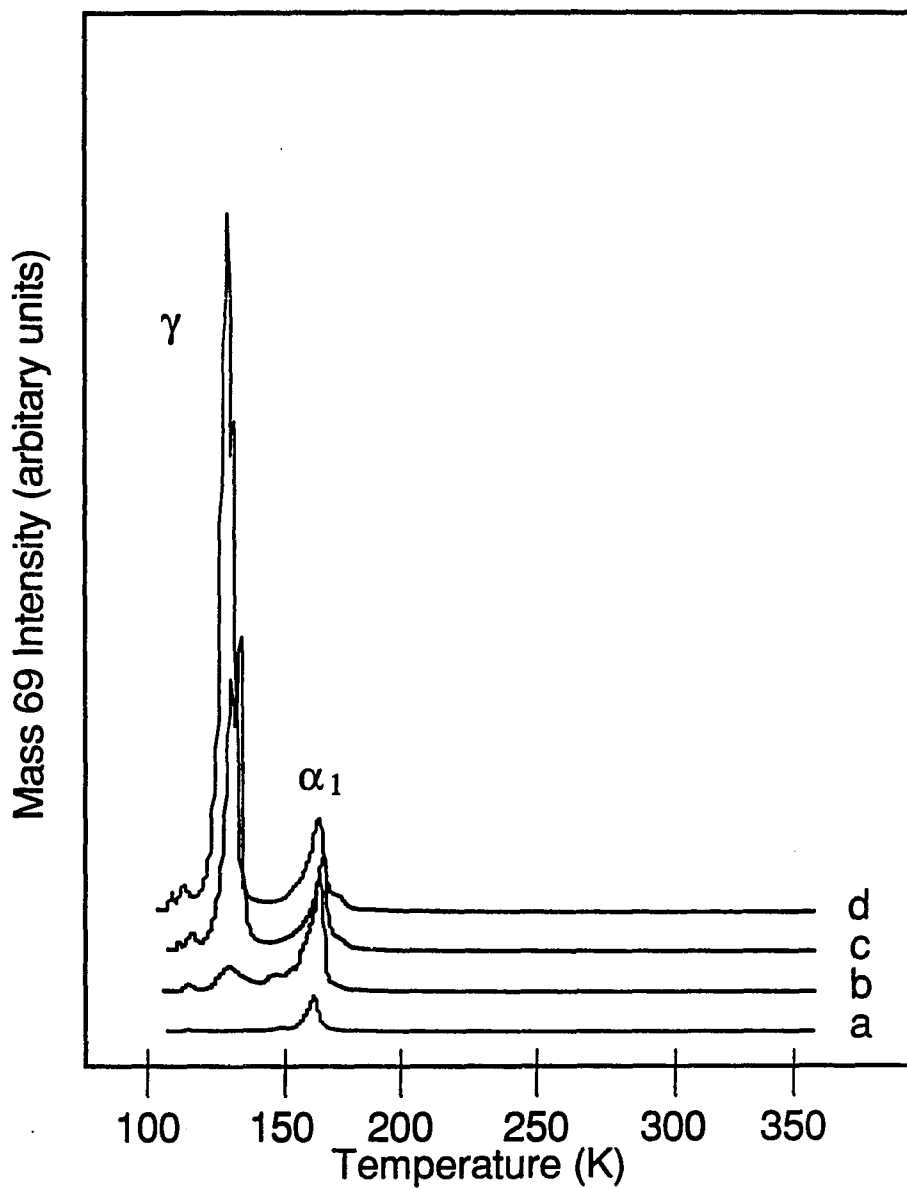


Figure 2. Thermal desorption spectra of perfluorodiethyl ether from Ru(001)

The spectra are obtained by monitoring mass 69 ( $\text{CF}_3^+$ ) following exposure to a) 0.07, b) 0.27, c) 0.67 and d) 1.0 L perfluorodiethyl ether. Equivalent spectra are obtained if other, less-intense fragments are monitored. The sample heating rate varies between 2.6 and 1.9 K/s.

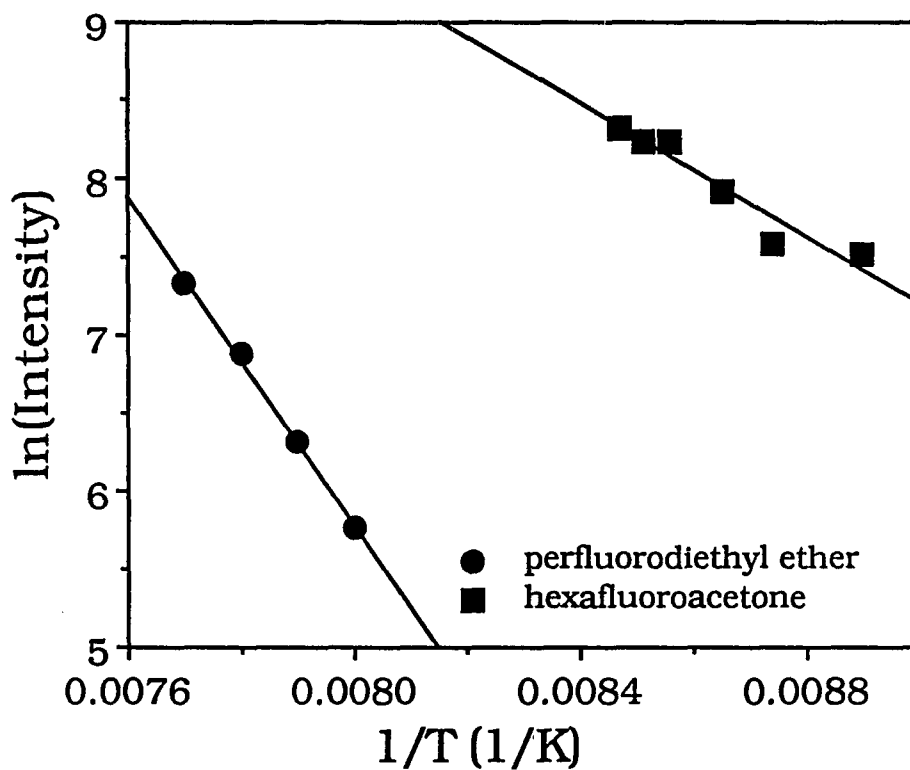


Figure 3. Arrhenius plot of the leading edges of the multilayer ( $\gamma$ ) peaks for the oxygenated fluorocarbons  
Circles correspond to perfluorodiethyl ether; squares correspond to hexafluoroacetone.



$50 \pm 10$  kJ/mol, where the uncertainty of  $\pm 10$  kJ/mol represents the standard deviation in  $E_s$  obtained from two separate experiments.

The shape of the  $\gamma$ -peak suggests resolution of a state corresponding to second-layer perfluorodiethyl ether molecules desorbing from the first condensed layer adsorbed on top of the monolayer. Such "second layer" desorption features have been observed previously [18].

The integrated desorption peak intensity is a linear function of exposure throughout the filling of the  $\alpha_1$ - and  $\gamma$ -states, as shown in Figure 4. Note that the line intersects the origin, which suggests that there is no decomposition. This is supported by the fact that the molecule adsorbs and desorbs reversibly, i.e., the desorption data can be reproduced repetitively without sample cleaning between successive experiments. In addition, there are no desorption peaks associated with masses 38, 66, 78, 88, 100, and 119, which would be the masses expected for  $F_2$ ,  $F_2C=O$ ,  $F_2C=C=O$ ,  $CF_4$ ,  $CF_2=CF_2$  or  $CF_3CF_2$  (an intense molecular fragment of  $CF_3CF_3$ ), respectively. Calibration of the CO desorption peak, as described in Section II, indicates that less than 0.02 monolayer of perfluorodiethyl ether decomposes.

For comparison, the thermal desorption spectra of diethyl ether from Ru(001) have also been measured, and are shown in Figure 5. These spectra are obtained by monitoring  $CH_3O^+$  at 31 amu, the most abundant molecular fragment.

At low exposures (curve a) the  $\alpha_1$ -state, at ca. 200 K, desorbs. The full-width at half maximum and desorption energy [17] of this peak are

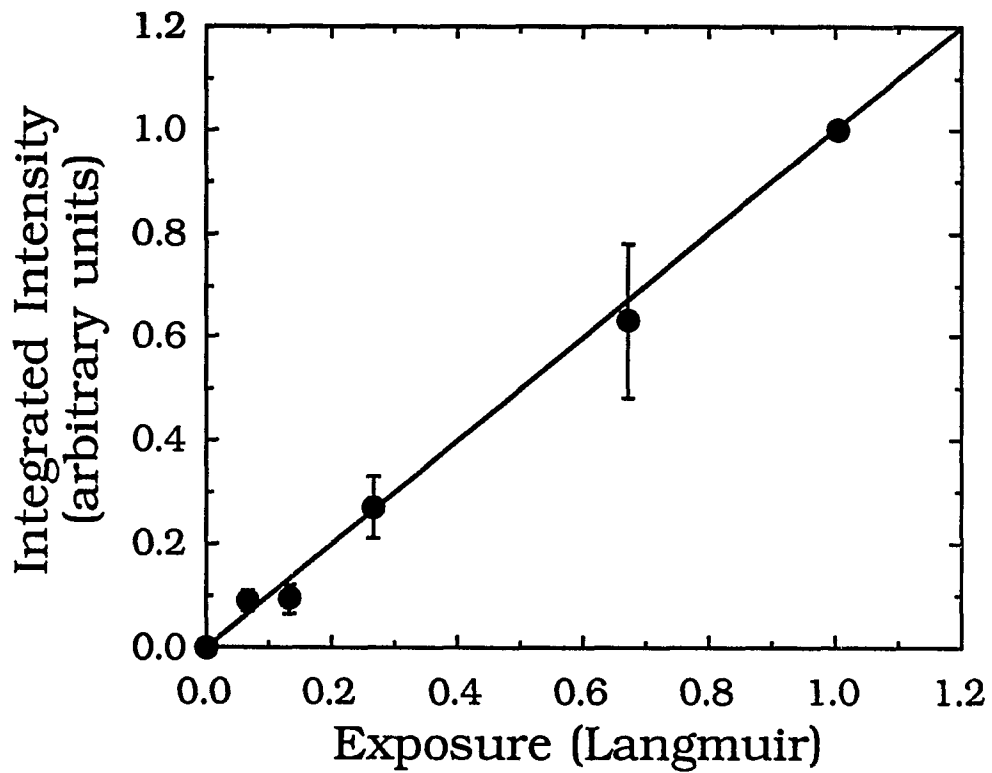


Figure 4. Integrated intensity of mass 69 ( $\text{CF}_3^+$ ) desorption as a function of exposure of perfluorodiethyl ether

The function increases monotonically over the entire exposure range.

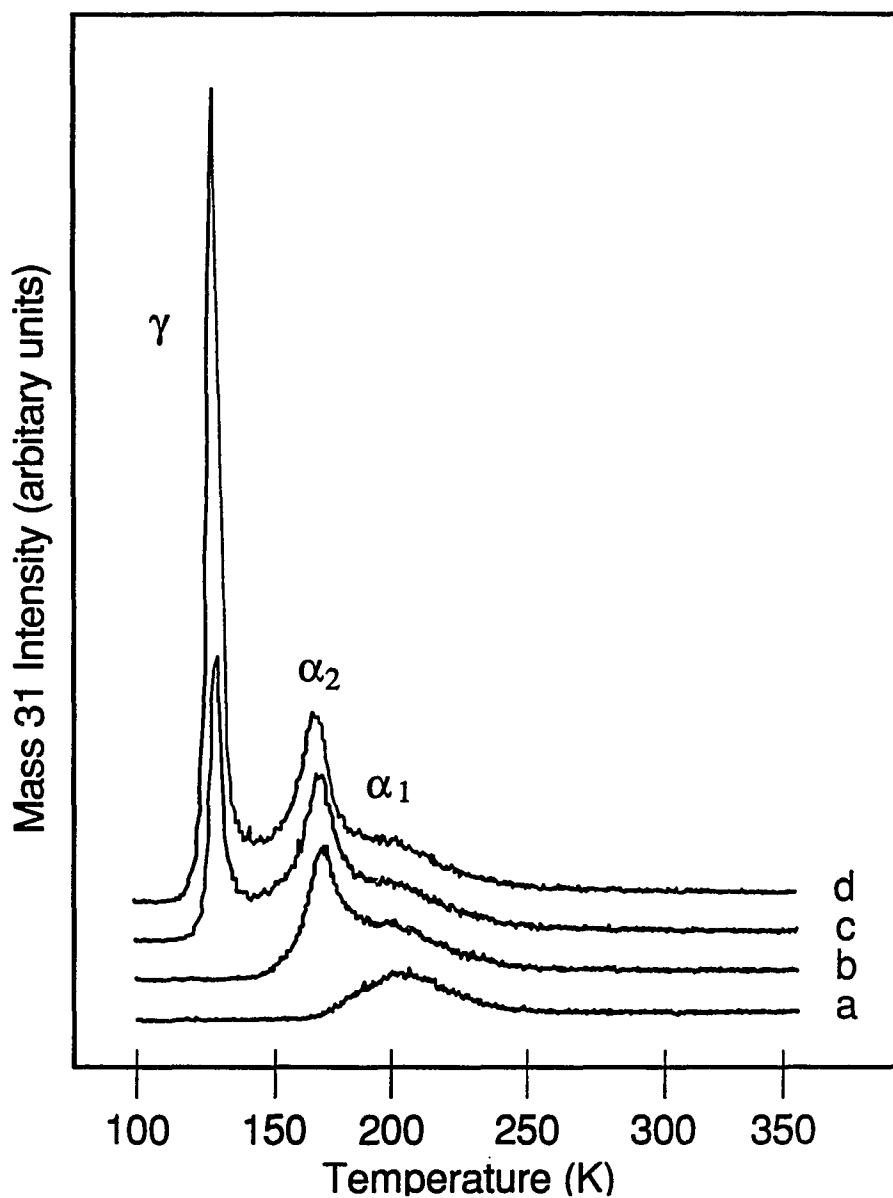


Figure 5. Thermal desorption spectra of diethyl ether from Ru(001). The spectra are obtained by monitoring mass 31 ( $\text{CH}_3\text{O}^+$ ) following exposure to a) 0.13, b) 0.25, c) 0.38 and d) 0.50 L diethyl ether. Equivalent spectra are obtained if other, less-intense fragments are monitored. The sample heating rate varies between 2.6 and 1.9 K/s.

$54 \pm 13$  K and  $51$ - $53$  kJ/mol, respectively. As exposure increases a second chemisorbed state,  $\alpha_2$ , desorbs at ca.  $170$  K. The full width at half maximum and desorption energy [17] of this peak are  $20 \pm 3$  K and  $43$ - $44$  kJ/mol respectively. At still higher exposures the multilayer state, labeled  $\gamma$ , desorbs at ca.  $130$  K. We attribute both  $\alpha$ -states to chemisorbed diethyl ether molecules. The amount of ether decomposition is summarized in Table 2. The value for the fluorinated ether corresponds to the evolution of CO; the extent of hydrogenated ether decomposition is based on hydrogen evolution.

#### B. Hexafluoroacetone

Thermal desorption spectra obtained after adsorption of  $(CF_3)_2CO$  on Ru(001) at  $90$  K are shown in Figure 6. The most abundant molecular fragment,  $CF_3^+$  at  $69$  amu [24], is monitored as a function of temperature. At low exposure, a single peak at  $345$  K is populated ( $\alpha_1$ ), as shown in curves a and b. With increasing exposure two other features develop simultaneously at  $265$  and  $155$  K which we designate  $\beta_1$  and  $\alpha_2$ , respectively. Finally, at high exposures, the  $\alpha_1$ -,  $\beta_1$ - and  $\alpha_2$ -features saturate and a narrow peak at ca.  $120$  K emerges. The latter state ( $\gamma$ ) cannot be saturated with increasing exposure.

The  $\alpha_1$ -,  $\beta_1$ - and  $\alpha_2$ -states exhibit the same characteristics of first-order desorption as described for perfluorodiethyl ether. The peak characteristics, relative populations and the corresponding values of  $E_d$  (assuming  $\nu = 10^{13} \text{ s}^{-1}$ ), are summarized in Table 3 for these three states.

Table 2. Decomposition of oxygenated fluorocarbons and hydrocarbons on Ru(001)

Molecule	Hydrogenated	Fluorinated
Diethyl ether	0.17	<0.02
Acetone	0.17,0.12[Z]	<0.02

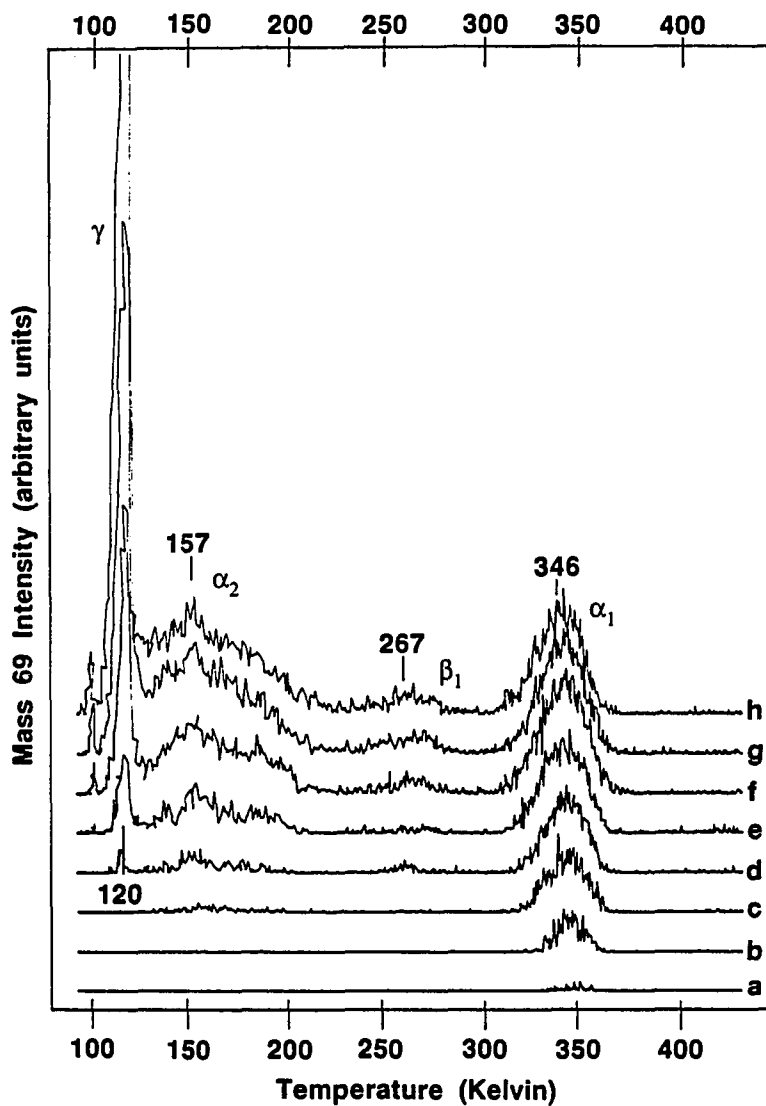


Figure 6. Thermal desorption spectra of hexafluoroacetone from Ru(001). Spectra are recorded by monitoring mass 69 ( $\text{CF}_3^+$ ) following a) 0.27, b) 0.53, c) 0.80, d) 1.1, e) 1.3, f) 1.6, g) 2.1 and h) 2.7 L of hexafluoroacetone. Equivalent spectra are obtained if other, less-intense fragments are monitored. The sample heating rate varies between 12 and 6 K/s.

Table 3. Desorption parameters for first-order states of hexafluoroacetone

These values were calculated according to Ref. 17 assuming  $\nu = 10^{13} \text{ s}^{-1}$ ,  $\beta = 10 \text{ K/s}$  and simple first-order kinetics

State	$T_p^a$ , K	FWHM <sup>a</sup> , K	Relative Population	$E_d$ , kJ/mol
$\alpha_1$	$346 \pm 1$	$22 \pm 2$	0.38	$86.5 \pm 0.3$
$\beta_2$	$267 \pm 4$	$34 \pm 7$	0.06	$66 \pm 2$
$\beta_3$	$157 \pm 1$	$61 \pm 3$	0.56	$38.3 \pm 0.4$

<sup>a</sup>The range of values indicates the variation over all coverages. For a simple first-order desorption peak, both  $T_p$  and the full width at half maximum (FWHM) remain constant [17].

The integrated area under the  $\alpha_2$ -peak, which is proportional to the number of molecules desorbing from that state, is 1.5 times larger than the area encompassed by the  $\alpha_1$ -peak. Curves g and h of Figure 6 are used for this analysis since at these exposures both the  $\alpha_1$ - and  $\alpha_2$ -peaks are saturated. The  $\alpha_1$ -,  $\beta_1$ -, and  $\alpha_2$ -features clearly represent states which are strongly influenced by the metal surface.

The  $\gamma$ -state is attributed to sublimation from the bulk-like multilayer. An Arrhenius plot of  $\ln(\text{Intensity})$  vs.  $1/T$  of the  $\gamma$ -peak leading edge, illustrated in Figure 3, indicates that the heat of sublimation at high coverage is  $22 \pm 2$  kJ/mol. [The uncertainty given is the standard deviation in the heat of sublimation evaluated from three separate spectra.] This is somewhat lower than the heat of sublimation of the bulk compound at the triple point, 147.70 K: 30 kJ/mol [30]. The integrated intensity of the total hexafluoroacetone spectrum is shown as a function of exposure in Figure 7. The changes in slope at exposures of ca. 0.6 and 1 L coincide with the onset of filling of the  $\beta_1$ - and  $\alpha_2$ -states (curve c of Figure 7) and with the onset of population of the multilayer (curve d of Figure 7), respectively. No desorption of mass 69 is observed at exposures less than 0.12 L. This suggests that some decomposition occurs, supported by the observation that thermal desorption spectra are not reproducible unless the sample is carefully cleaned between each adsorption-desorption cycle. However, no peaks are present in the desorption traces of masses 38, 66, 78, 88, and 100 amu, corresponding to  $F_2$ ,  $F_2C=O$ ,  $F_2C=C=O$ ,  $CF_4$ , and  $CF_2=CF_2$ . CO thermal



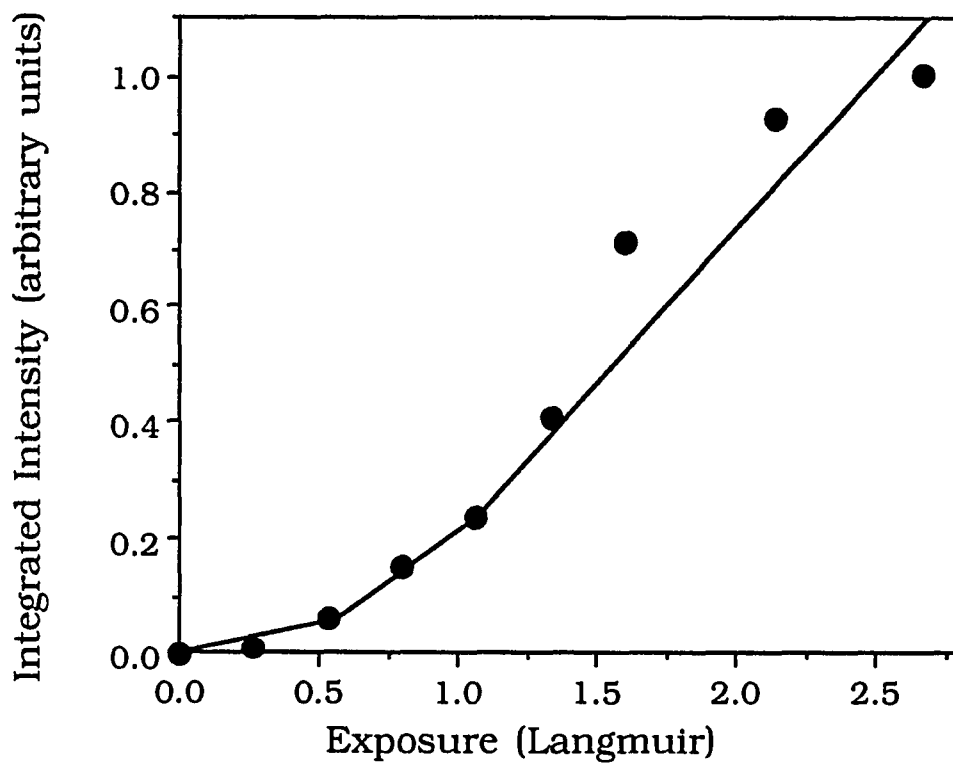


Figure 7. Integrated intensity of mass 69 desorption as a function of exposure of hexafluoroacetone

The breaks at ca. 0.6 and 1.0 L correspond to the onset of filling the  $\alpha_2$ - and  $\gamma$ -states, respectively.

desorption, however, indicates that less than 0.02 monolayer (our detection limit) of hexafluoroacetone decomposes (see Table 2). Auger electron spectroscopy does not detect a fluorine residue following the TDS experiments, perhaps because the cross-section for electron-stimulated desorption is prohibitively high.

Adsorption of 0.5 L oxygen at room temperature, with subsequent cooling to 90 K and exposure to ca. 2.1 L of hexafluoroacetone, results in suppression of the  $\alpha_1$ -hexafluoroacetone state and desorption from a new state between the  $\beta_1$ - and  $\alpha_2$ -states as shown in Figure 8. Coadsorption of 1 L  $O_2$  completely suppresses the  $\alpha_1$ -state in favor of the new feature at ca. 215 K.

For comparison, thermal desorption spectra of acetone have also been measured and are shown in Figure 9. These spectra are obtained by monitoring  $CH_3CO^+$ , 43 amu, the most plentiful molecular fragment. The high temperature state ( $\alpha_1$ ) desorbs between 195 and 210 K corresponding to  $E_d = 48$ -52 kJ/mol. Another notable feature in the desorption spectrum is the long, high temperature tail on the peak. At high exposures a multilayer state at 150 K is populated. We find that 0.17 monolayers of acetone decompose on the saturated surface (Table 2).

These data agree well with previous work by Anton et al. [Z], where acetone is reported to desorb in a broad peak between 200 and 400 K ( $E_d = 42$ -62 kJ/mol). Our desorption spectra are similar except that we resolve a peak at ca. 195 to 210 K ( $E_d = 47$ -52 kJ/mol). Anton et al. also report that 0.12 monolayer of acetone decompose [Z], which is reasonably close

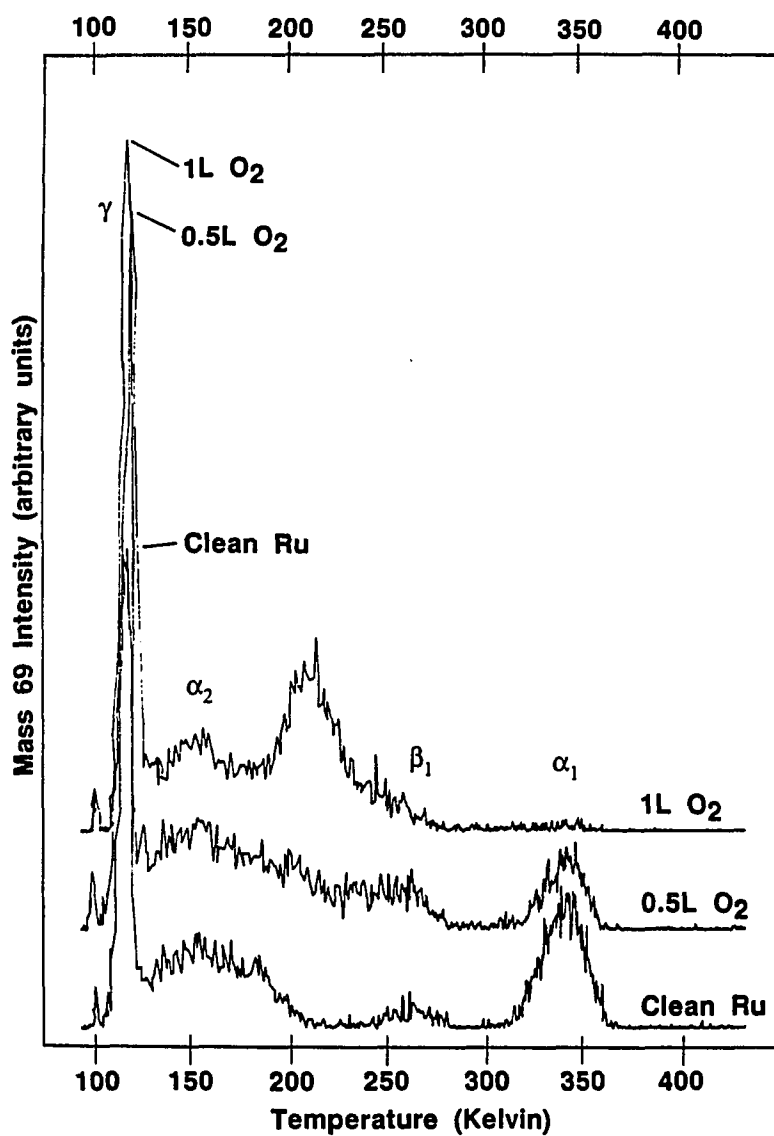


Figure 8. The effect of preadsorbed oxygen on thermal desorption states of hexafluoroacetone

Oxygen exposure occurs at 300 K. Upon cooling to 90 K, the sample is exposed to 2.1 L of hexafluoroacetone. As oxygen exposure increases a new desorption state at ca. 215 K is populated at the expense of the  $\alpha_1$ -state.

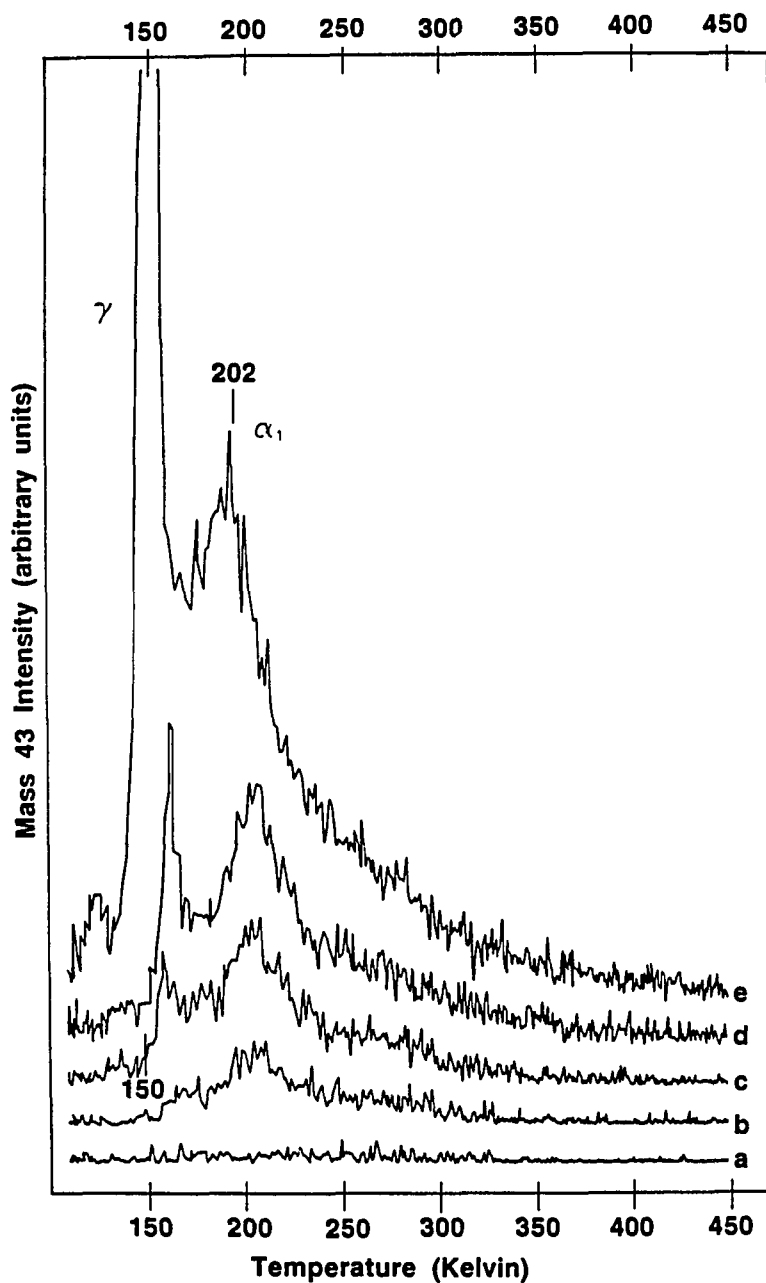


Figure 9. Thermal desorption spectra of acetone from Ru(001). Spectra are recorded after exposure to a) 0.76, b) 1.2, c) 1.5, d) 1.7 and e) 2.6 L of acetone. Equivalent spectra are obtained if other, less-intense fragments are monitored. The sample heating rate varies between 12 and 6 K/s.

to our value of 0.17. EELS results confirm the presence of both  $\eta^1(0)$ - and  $\eta^2(C,0)$ -acetone on Ru(001) in the chemisorbed layer [7].

## IV. DISCUSSION

### A. Perfluorodiethyl Ether

Perfluorodiethyl ether is a simple chemical model for commercially used polymeric perfluorinated lubricants, which are often ethers. Our present work shows that the chemisorption bond of the fluorinated ether on Ru(001) is rather weak, 42-43 kJ/mol, and is lower by 8-11 kJ/mol than the nonfluorinated ether in the limit of low exposures, where intermolecular interactions are minimized. This is consistent with the ideas discussed in the Introduction, i.e., fluorination can only weaken one or both of the attractions between the molecule and the surface: electron donation from the oxygen lone pairs to the metal, and attraction between CH<sub>2</sub> groups and the metal.

We find that less than 0.02 monolayer of perfluorodiethyl ether decomposes. In contrast, about 0.17 monolayer of diethyl ether decomposes on Ru(001) (see Table 2) and 0.1 of a full layer of diethyl ether decomposes on Pt(111) to yield CO, H<sub>2</sub>, and CH<sub>x</sub> [2,3]. A possible explanation is the difference between the C-H bond strength (406 kJ/mol in C<sub>2</sub>H<sub>6</sub> [31]) and the C-F bond strength (480 kJ/mol in C<sub>2</sub>F<sub>6</sub> [32]). This stabilization of the C-F bond may be important if decomposition of the molecule is limited by the rate of C-F or C-H bond breaking. Furthermore, the fluorinated ethers, since they desorb at low temperatures, may not remain on the surface to the temperatures required

to initiate decomposition. The hydrogenated ethers, on the other hand, are chemisorbed on the surface to higher temperatures.

A second possible explanation is that the hydrocarbon portion(s) of the molecule must approach the metal rather closely in order for the first internal molecular bond to break, whether that is the C-O, C-C or C-H (C-F) bond. For the reasons given the Introduction, we believe it is not as favorable for a saturated fluorocarbon segment to approach a metal surface as closely as the analogous saturated hydrocarbon segment. This would effectively increase the energy barrier for metal-catalyzed decomposition of a fluorinated ether relative to the nonfluorinated molecule.

#### B. Hexafluoroacetone

Inspection of previously published data for ketones and aldehydes adsorbed on Pt(111) [9,10], Ru(001) [6,7,9], and oxygen predosed Ru(001) [6,7], summarized in Table 1, shows that the following generalizations are true:

- 1) When a majority of molecules are bonded as  $\eta^1$ , the extent of decomposition is small or undetectable. Significant decomposition is associated with  $\eta^2$ -coordination.
- 2) The chemisorption bond strengths of  $\eta^1$ -carbonyls are generally below 50 kJ/mol ( $T_p < 200$  K), whereas the bond strengths of  $\eta^2$ -carbonyls are generally 60-70 kJ/mol and above ( $T_p > 200$  K).

- 3) The fraction of chemisorbed molecules bonded in the  $\eta^2$ -coordination, which requires electron donation from the metal into a  $\pi^*$  orbital of the carbonyl, is suppressed by co-adsorption of oxygen. This has been attributed to competition between the electronegative oxygen and the  $\eta^2$ -carbonyl for electron withdrawal from the metal [6,7].

We find that less than 0.02 monolayer hexafluoroacetone decomposes on Ru(001). Our detection limit for decomposition (0.02 monolayer) is perhaps not low enough to detect decomposition. Other facts, such as no desorption of hexafluoroacetone below a 0.12 L exposure and irreproducible spectra without carefully cleaning the crystal, suggest that some hexafluoroacetone decomposes, albeit less than we can detect. There are three desorption states which are distinguishable from the multilayer:  $\alpha_1$  (87 kJ/mol),  $\beta_1$  (66 kJ/mol), and  $\alpha_2$  (38 kJ/mol). The  $\alpha_1$ -state is suppressed by coadsorbed oxygen, while a new state midway between  $\beta_1$  and  $\alpha_2$  is created. The fact that oxygen induces a conversion between chemisorbed states indicates that the oxygen exerts an electronic effect rather than simple site-blocking. All three of these observations, taken together, indicate that the  $\alpha_1$ -state represents molecules bonded to the metal via  $\eta^2$ -coordination, whereas the  $\alpha_2$ -state represents molecules in the  $\eta^1$ -configuration.

Within the context of this model, a comparison between the chemisorption bond strengths of hydrogenated acetone [7 and this work] and fluorinated acetone (this work) indicates that fluorination weakens



the  $\eta^1$ -bond of the chemisorbed carbonyl by 12 kJ/mol, whereas fluorination strengthens the  $\eta^2$ -bond by ca. 20 kJ/mol. The rationale for these trends has been presented in the Introduction. Fluorination also changes the relative distribution of  $\eta^1$ - and  $\eta^2$ -molecules which desorb (cf. Figures 6 and 9), but at this point we cannot say whether that represents a change in the initial populations of adsorbed molecules, or a change in the relative rates of competing processes such as desorption and decomposition. In either case, if this model is correct, it is clear that the  $\eta^2$ -bond can form for both the fluorinated and hydrogenated species, i.e., steric hindrance between the  $\text{CF}_3$  groups and the metal is not prohibitive in this case. The withdrawal of electron density by the fluorine atoms from the oxygen functional group appears to outweigh steric hindrance in determining how the molecule bonds to the Ru surface, in contrast to the observations made by Avery for the Pt(111) surface [10].

## IV. CONCLUSIONS

Perfluorodiethyl ether bonds to Ru(001) with a lower binding energy than the nonfluorinated compound in the low-exposure limit. This is explained by inductive withdrawal of electron density from the oxygen lone pairs by the fluorine atoms, which weakens the primary chemisorption bond. The CF<sub>2</sub>-metal interaction is probably also repulsive due to steric repulsion between the metal and the fluorine atoms. Hexafluoroacetone, with its unsaturated carbonyl group, can form stronger metal-surface bonds, which suggests that some of the molecules bond in a  $\eta^2$ -geometry. Fluorination decreases the chemisorption bond strength of the  $\eta^1$ -molecules by about 10 kJ/mol and increases that of the  $\eta^2$ -species by about 20 kJ/mol.

## V. ACKNOWLEDGEMENTS

We thank R. J. Angelici and T. Upton for valuable discussions. This research has been supported by the Director for Energy Research, Office of Basic Energy Sciences. Ames Laboratory is operated for the U.S. Department of Energy by Iowa State University under Contract No. W-7405-ENG-82.

## VI. REFERENCES

1. H. Lüth, G. W. Rubloff and W. D. Grobman, *Surface Science*, 63 (1977) 325.
2. B. A. Sexton and A. E. Hughes, *Surface Science*, 140 (1984) 227.
3. K. D. Rendulić and B. A. Sexton, *J. Catalysis*, 78 (1982) 126.
4. P. A. Thiel and T. E. Madey, *Surface Sci. Reports*, 7 (1987).
5. R. O. Gould, W. J. Sime and T. A. Stephenson, *J. Chem. Soc. Dalton*, 1 (1978) 76.
6. A. B. Anton, J. E. Parmeter and W. H. Weinberg, *J. Am. Chem. Soc.*, 108 (1986) 1823.
7. A. B. Anton, N. R. Avery, B. H. Toby and W. H. Weinberg, *J. Am. Chem. Soc.*, 108 (1986) 684.
8. N. R. Avery, *Surface Science*, 125 (1983) 771.
9. N. R. Avery, W. H. Weinberg, A. B. Anton and B. H. Toby, *Phys. Rev. Lett.*, 51 (1983) 682.
10. N. R. Avery, *Langmuir*, 1 (1985) 162.
11. C. D. Wood and R. R. Schrock, *J. Am. Chem. Soc.*, 101 (1979) 5421.
12. R. Countryman and B. R. Penfold, *J. Cryst. Mol. Struct.*, 2 (1972) 281.
13. T. T. Tsou, J. C. Huffman and J. K. Kochi, *Inorg. Chem.*, 18 (1979) 2311.
14. W. L. Jorgensen and L. Salem, *The Organic Chemists' Book of Orbitals* (Academic Press, New York, 1973). Comparison of the energy of the

- 2B<sub>2</sub> orbital of formaldehyde and the 3A" orbital of formyl fluoride.
15. J. E. Deffeyes, A. H. Smith and P. C. Stair, *Surface Science*, 163 (1985) 79.
  16. J. E. Deffeyes, A. H. Smith and P. C. Stair, *Appl. Surface Science*, 26 (1986) 517.
  17. P. A. Redhead, *Vacuum*, 12 (1962) 203.
  18. T. E. Madey and J. T. Yates, Jr., *Surface Science*, 76 (1978) 397.
  19. F. M. Hoffmann and T. H. Upton, *J. Phys. Chem.*, 88 (1984) 6209.
  20. A. D. Mitchell and L. C. Cross, Eds., Tables of Interatomic Distances and Configurations in Molecules and Ions (Burlington House, London, 1958).
  21. R. D. Chambers, Fluorine in Organic Chemistry (John Wiley and Sons, New York, 1973).
  22. E. D. Williams and W. H. Weinberg, *Surface Science*, 82 (1979) 93.
  23. P. A. Thiel and J. W. Anderegg, *Rev. Sci. Instrum.*, 55 (1984) 1669.
  24. S. R. Heller and G. W. A. Milne, EPA/NIH Mass Spectral Data Base NSRDS-NBS63, Vol. 1 (U.S. Government Printing Office, Washington, D. C., 1978).
  25. G. G. Hawley, Condensed Chemical Dictionary 10th edition (Van Nostrand Reinhold Co., New York, 1981).
  26. J. M. Neilsen, Compilation of Material Safety Data Sheets Vol. 1 (Technology Marketing Operation, General Electric Corp., Schenectady, NY, 1980).
  27. H. Herz, H. Conrad and J. Küppers, *J. Phys. E*, 12 (1979) 369.

28. P. Feulner and D. Menzel, *Surface Science*, 154 (1985) 465.
29. M. Y. Chou and J. R. Chelikowsky, *Phys. Rev. Lett.*, 59 (1987) 1737.
30. A. C. Plaush and E. L. Pace, *J. Chem. Phys.*, 47 (1967) 44.
31. V. I. Vedeneyev, L. V. Gurvich, V. N. Kondratyev, V. A. Medvedev and Y. L. Frankevich, Bond Energies, Ionization Potentials and Electron Affinities (Edward Arnold, Ltd., London, 1966).
32. M. Stacey, J. C. Tatlow, and A. G. Sharpe, Advances in Fluorine Chemistry Vol. 2 (Butterworths, London, 1961).

PAPER II:

THE BONDING OF FLUORINATED AND HYDROGENATED DIETHERS TO RU(001)

THE BONDING OF FLUORINATED AND HYDROGENATED DIETHERS TO RU(001)

M.M. Walczak and P.A. Thiel

Department of Chemistry and Ames Laboratory

Iowa State University

Ames, Iowa 50011



## ABSTRACT

We describe studies of both fluorinated and hydrogenated diethers on the Ru(001) surface. We find that 1,1'-[methylenebis(oxy)]bisethane ( $\text{CH}_3\text{CH}_2\text{OCH}_2\text{OCH}_2\text{CH}_3$ ) chemisorbs on Ru(001) with a bond strength of 53-69 kJ/mol. About 0.05 monolayer decomposes. For comparison, 0.04 monolayer of 1,2-diethoxyethane ( $\text{CH}_3\text{CH}_2\text{OCH}_2\text{CH}_2\text{OCH}_2\text{CH}_3$ ) decomposes. The chemisorbed diethoxyethane molecules desorb in three states. The desorption energy of the majority state is 58-62 kJ/mol. 1,2-Perfluorodiethoxyethane ( $\text{CF}_3\text{CF}_2\text{OCF}_2\text{CF}_2\text{OCF}_2\text{CF}_3$ ) bonds less strongly (44-47 kJ/mol) to Ru(001) than its hydrogenated analog, diethoxyethane. No perfluorodiethoxyethane decomposes. The diethers bond between 12% and 35% more strongly than the monoether analogs.

## I. INTRODUCTION

The chemical interaction between lubricants and metals is not understood on a molecular scale. Fundamental information which may allow lubricants to be custom-tailored for specific applications is not available. Major unanswered questions include: How strongly do prototypical lubricant molecules bond to surfaces? Which functional group bonds? Does the molecule decompose? What are the decomposition products and how do they interact with the surface? Our approach to answering the foregoing questions is to compare the surface chemistry of fluorinated molecules with that of their hydrogenated analogs. Oxygenated hydrocarbons have been studied on many surfaces [1-7] and the surface chemistry of these molecules is fairly well understood.

Many commercial lubricants used in the computer and aerospace industries belong to the class known as perfluoropolyethers (PFPEs). This class of molecules is often chosen for use in environments where chemical degradation of the lubricant is a potential problem, since the fluorinated molecules exhibit excellent thermal and oxidative stability [8-11]. In at least one application, the bonding of fluorinated polymers to surfaces is an important key in the proper functioning of the lubricant. In this application, the computer industry uses liquid PFPEs, such as Fomblin, to coat hard disks, thus preventing "crashes". A disk "crash" occurs when the head cold welds to the bare substrate, usually during power up and down procedures. When the disk is operating the

lubricant coating must stay in place on the spinning disk. Since disks rotate at high speeds, lubricant molecules must be chemically bonded to the surface so they are not swept off by centrifugal force during disk rotation. To create a stronger lubricant-disk bond, the ethers often have an "anchoring" group, such as a carbonyl group or aromatic ring, synthesized at the end of the polymeric chain. Our approach to the surface chemistry of lubricants is to model the industrially-used lubricants with smaller, prototypical molecules.

In Paper I of this dissertation, we describe thermal desorption spectroscopy (TDS) results of perfluorodiethyl ether ( $\text{CF}_3\text{CF}_2\text{OCF}_2\text{CF}_3$ ) and hexafluoroacetone ( $(\text{CF}_3)_2\text{C}=\text{O}$ ) and their hydrogenated analogs on the hexagonal Ru(001) surface. These results show that perfluorodiethyl ether, representative of the ether linkage in a real lubricant, bonds to Ru(001) weakly and undergoes no significant decomposition. Hexafluoroacetone, representative of an end "anchoring" group, is also very stable against decomposition, and bonds to Ru(001) in two different configurations:  $\eta^2(\text{C},\text{O})$ - and  $\eta^1(\text{O})$ -hexafluoroacetone. The  $\eta^2$ -configuration, favored at low coverage, bonds more strongly to the surface than does the  $\eta^1$ -configuration.

In this paper, we extend our studies to fluorinated and hydrogenated diethers on Ru(001). Since many commercial lubricants are polymeric fluorinated ethers, dimeric ethers are a step closer to real, long-chain lubricant molecules. We believe the results presented in this paper have direct relevance to the industrially-used PFPEs.

## II. EXPERIMENTAL

The experiments are performed in an ion-pumped, stainless steel UHV chamber with a base pressure of  $7 \times 10^{-11}$  Torr. A cross section of the chamber is shown schematically in Figure 1A. Two perpendicular cross sectional schematics are shown in Figures 1B and C. The chamber is equipped with (clockwise from bottom center in Figure 1A) a pinhole-aperture gas doser, a UTI-100C mass spectrometer and cryogenic shield, a rotatable shutter at the entrance to the Auger spectrometer, an ion gun, and optics and electron gun for Electron-Stimulated Desorption Ion Angular Distribution (ESDIAD) experiments. The parts of the vacuum chamber relevant to the experiments discussed in this dissertation are described in more detail.

The gas doser contains a  $2 \mu\text{m}$ , conductance-limiting pinhole aperture, and is used for exposing the crystal to ether. During dosing, the sample is positioned between 0.25 and 0.50 inch from the end of the doser. For these experiments, pressures between 3 and 15 Torr of reactant gas behind the pinhole aperture are typical. For each exposure the sample is rotated in front of the doser and the valve to the gas supply is opened. After the desired time interval elapses, the sample is rotated away from the doser and the valves to the gas supply and pump are closed and opened, respectively. The doser is calibrated by comparing the area under the CO desorption peak as a result of exposure through the doser with that achieved by backfilling the chamber with CO. [The chamber has three variable leak values (not shown in Figure 1) for

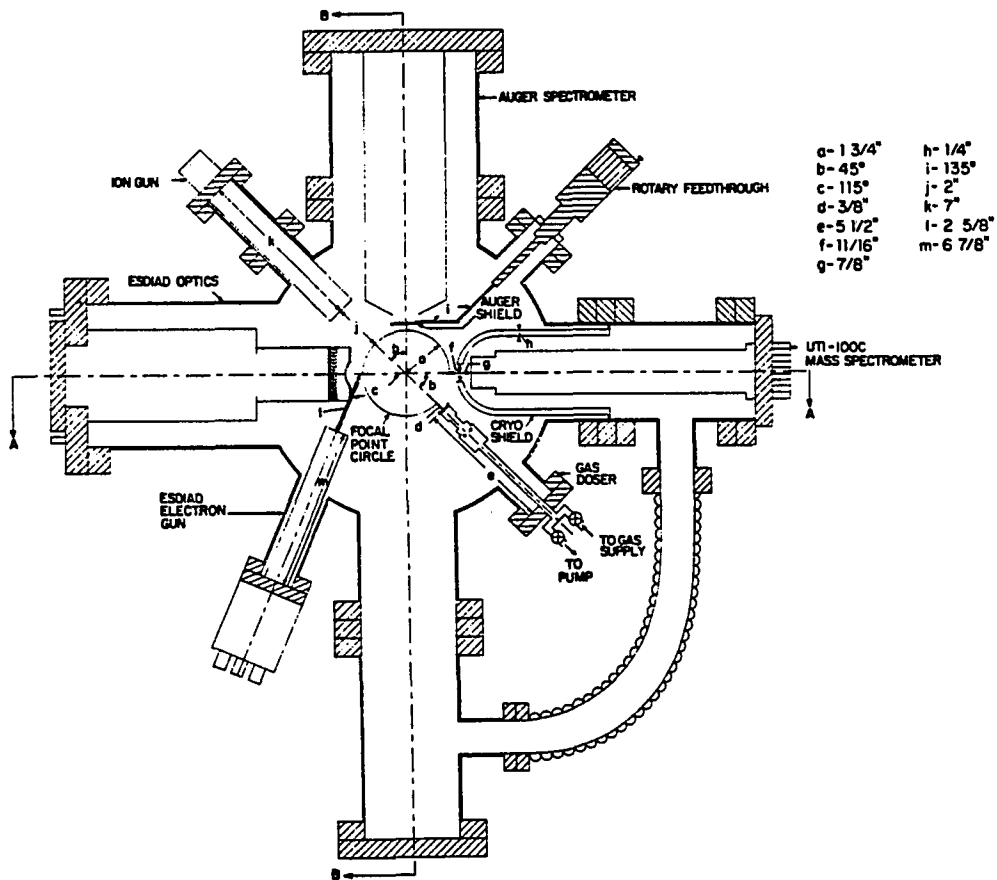


Figure 1A. Schematic cross section of vacuum chamber

The base pressure of the chamber is  $7 \times 10^{-11}$  Torr. The cross section is taken through the focal point circle.

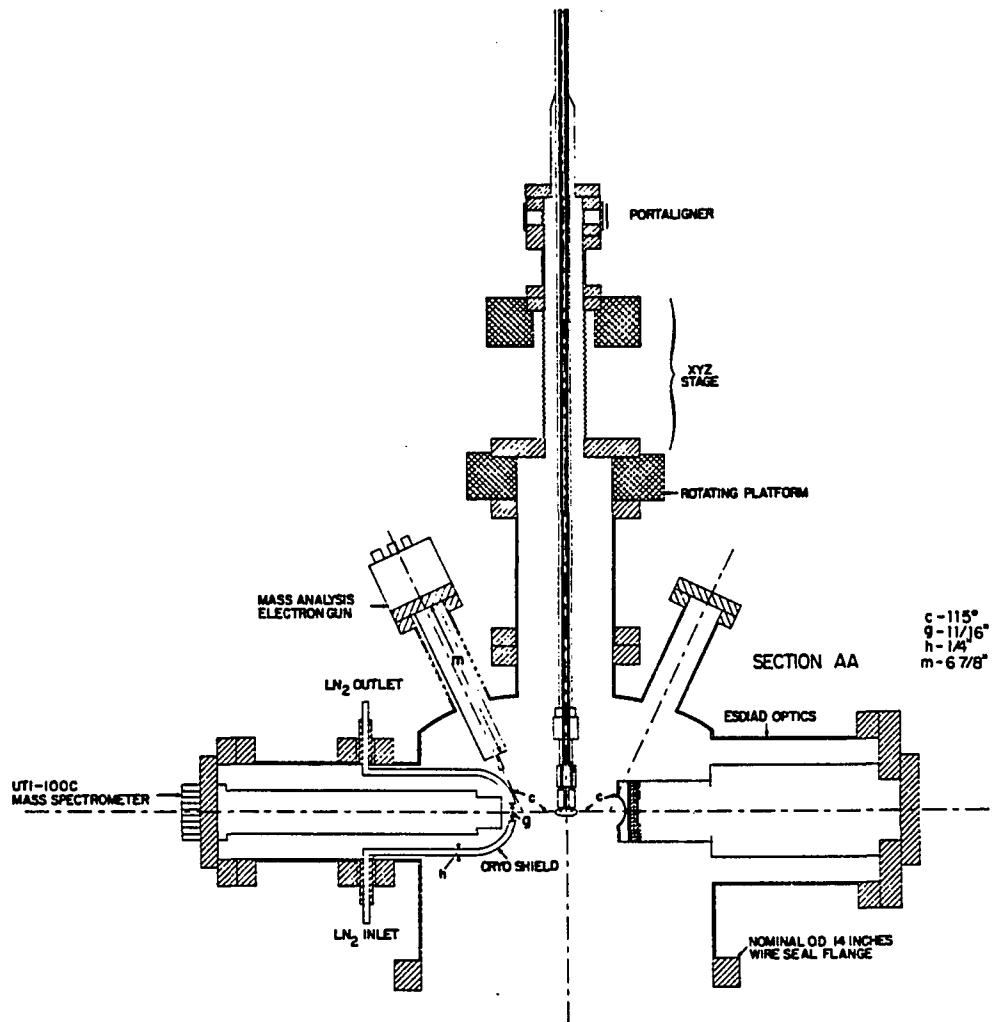


Figure 1B. Schematic cross section of vacuum chamber  
Cross section AA.

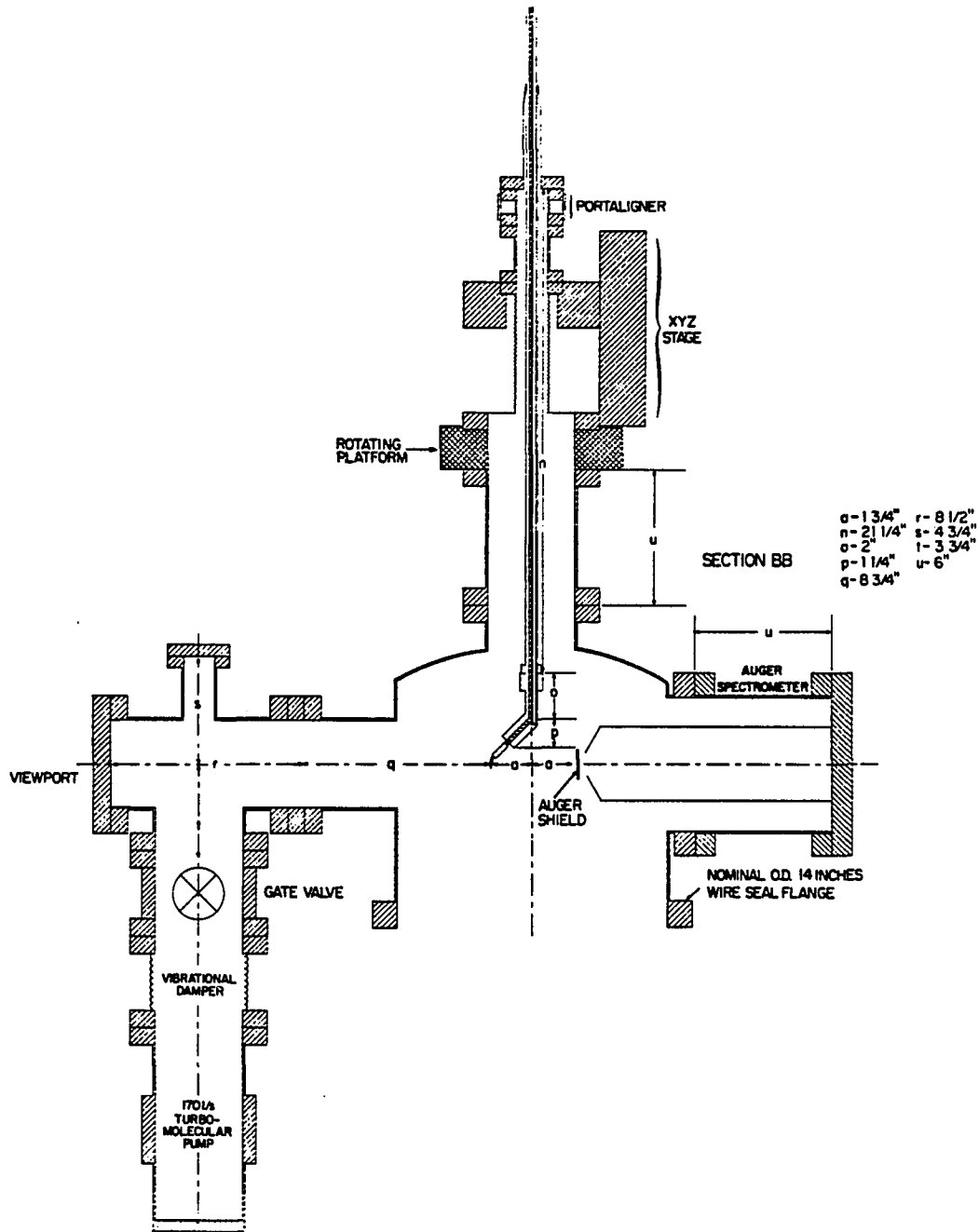


Figure 1C. Schematic cross section of vacuum chamber  
Cross section BB.

introducing oxygen, hydrogen, argon and carbon monoxide gas.] Since molecular flux is proportional to the inverse square root of molecular weight, the reactant gas exposures are also multiplied by the square root of the ratio of the molecular weight of CO (28 amu) to the molecular weight of the gas of interest. The exposures reported in this paper are in Langmuir, arrived at by correcting the exposures through the doser in this manner.

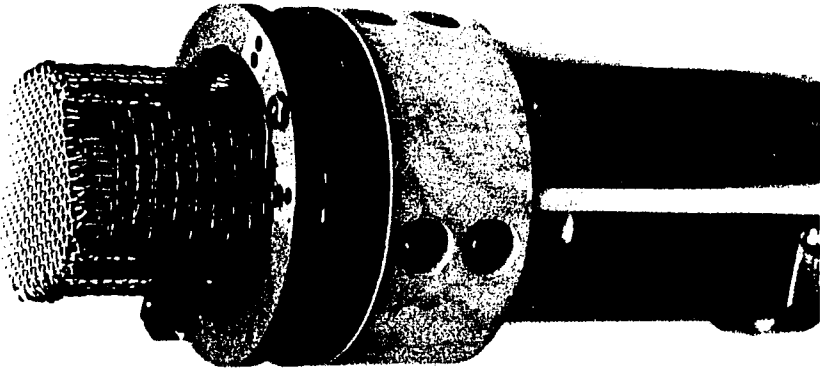
The Auger shield, which can be rotated in front of the cylindrical mirror analyzer (CMA) (see Figures 1A and C), is necessary to prevent directed streams of reactive gases from entering the CMA. After several days of experiments without the shield in front of the spectrometer, clean Auger spectra are unattainable. Baking the chamber remedies this situation. We believe that this problem is due to contamination of the CMA by reactive gases during sample exposures. To alleviate this problem, the shield is positioned in front of CMA when using the doser.

The ionizer of the mass spectrometer is modified to reduce the current at the sample due to electrons from the ionizer [12]. The two-part modification is shown in Figure 2. The first part of the modification is the fine mesh screen spot-welded to the top of the inner grid, shown in Figure 2a. The reflector grid added in Figure 2b reflects electrons into the ionizer region and also holds the filaments. The second modification is the addition of a floating cage mounted over the reflector assembly, shown in Figure 2c. During operation, the floating cage charges to a potential equal to the filament (electron) voltage (70

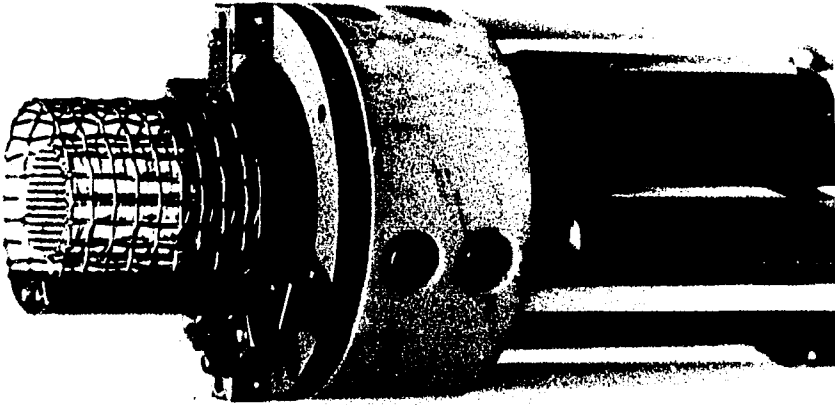


Figure 2. Mass spectrometer ionizer modification

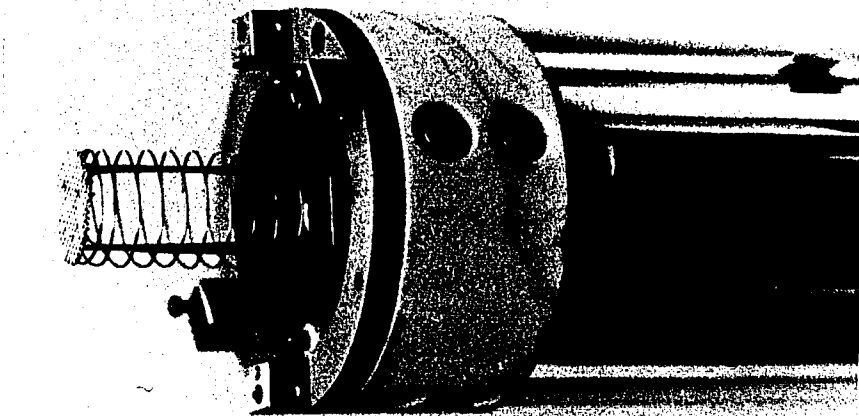
These photos show the stepwise assembly of the modified ionizer. (a) The inner grid. A piece of screen is spotwelded to the top of the inner grid to prevent the isolation cage from extracting too many ions from the source. (b) The repeller grid, which holds the filaments, is added. (c) The floating cage, which is electrically isolated from the ionizer, is attached. This cage charges to the potential of the electrons and, thus, prevents electrons from leaving the ionizer. As a result of this modification, the electron current at the sample is reduced from 10  $\mu\text{A}$  to less than 1 nA.



c)



b)



a)

eV) and repels stray electrons emitted from the ionizer and not reflected by the reflector grid.

As a result of the charge on the floating cage, the cage is capable of extracting ions from the ionizing region. Addition of the screen to the top of the inner grid alleviates this problem. The filament protection circuit in the UTI console is disabled for the unit to operate with this modification. Otherwise, the current lost to the floating cage reduces the current detected at the inner cage enough to trip the filament protection circuit.

A disadvantage of the ionizer modification is a persistent background mass 16 ( $O^+$ ) signal due to electron stimulated desorption of oxygen atoms from the ceramic ring support of the floating grid. Another problem encountered after operating for a period of time with this modification, is a large background mass 19 ( $F^+$ ) signal. This probably results from electron bombardment of the stainless steel components used in the ionizer modification, which eventually exposes surfaces which contain fluorine as a result of the chemical pretreatment of the material. Modifying the ionizer in this way reduces the current at the sample positioned in front of the mass spectrometer from 10  $\mu A$  to less than 1 nA. This minimizes electron-induced damage to the adsorbed molecules. [The fluorinated compounds are particularly sensitive [13-14].]

Figures 1A and B also show a cryo shield around the mass spectrometer ionizer. This shield, built on a six inch o.d. double sided

Conflat flange, is filled with liquid nitrogen to decrease background signals. Thermal desorption experiments conducted with the ionizer 7/8 inch from the focal point circle result in pressure bursts after the mass spectrometer is on approximately five minutes. The pressure bursts are, presumably, a result of the ionizer heating up the inside of the cryo shield. The mass spectrometer is therefore moved back an additional 0.69 inch by adding a double sided 4.5 inch flange between the mass spectrometer and the reducing flange. With this modification, experiments lasting as long as twenty minutes are not troubled by pressure bursts. Unfortunately, this increases the sample to ionizer distance to 1.56 inch and, therefore, reduces the signal intensity. The lower signal intensity does not seriously affect the thermal desorption experiments.

The Ru(001) sample (surface area about  $0.8 \text{ cm}^2$ ), is grown at the Ames Laboratory Materials Preparation Center. The crystal is oriented and polished to within 1 degree of the (001) face on both sides. The initial crystal cleaning procedure under vacuum includes successive heating (up to 1600 K), ion bombardment, and oxidation cycling [15]. Sample cleanliness is monitored by TDS of CO following oxygen exposure, and by Auger spectroscopy. The crystal is mounted with a swaged Ta wire measuring 0.051 inch in diameter on one end and 0.028 inch on the other end. The thin end is melted into a 0.066 inch diameter sphere. The sample is spotwelded to the Ta spheres and the thick ends are attached to a liquid-nitrogen-coolable cold finger [16]. The overall length of Ta

wire extending from the cold finger to the sample is 1.63 inch. The sample temperature is monitored by a W-5% Re vs. W-26% Re thermocouple pair spot welded to the back of the crystal. Temperatures between 85 and 1600 K are accessible via liquid nitrogen cooling and resistive heating, respectively. The sample can be cooled from 1600 to 85 K in seven minutes.

The feedback circuit [17], which controls the sample temperature, ramps linearly in millivolts. Since the conversion between millivolts and temperature is nonlinear for the W-5% Re vs. W-26% Re thermocouple, the sample heating rate varies between about 1.6 and 2.7 K/s over the temperature range of interest, 100-350 K.

The UTI-100C mass spectrometer is interfaced to a PDP-11/23 computer which allows multiplexing of up to eight different masses in a single TDS experiment. The computer program is described in more detail in Appendix A of this thesis. The temperatures recorded in the text and Figures of this paper are rounded to the nearest 5 K.

The purity of the ethers is determined in-house at the Chemistry Department Instrument Services Facility using gas chromatography mass spectroscopy (GCMS). A Finnigan 4000 quadrupole mass spectrometer (electron energy 70 eV) is used to measure the mass spectra of the ethers and their contaminants. The hydrogenated diethers, diethoxymethane and diethoxyethane are purchased from Aldrich and are 99.4% and 98.9% pure, respectively. All ethers are purified before use in a series of freeze-pump-thaw cycles on the gas-handling manifold.

The fluorinated diether, perfluorodiethoxyethane, is obtained from Exflor Research, Inc. GCMS analysis indicates the sample is 94% pure. This compound is purified further on the gas handling manifold as described above. The main impurity, determined by positive ion chemical ionization mass spectroscopy, is the monohydro compound  $C_6HF_{13}O_2$ .

We also measure the mass spectra of all compounds in our apparatus prior to adsorption-desorption experiments. The *in situ* spectra are not identical to those obtained on the Finnigan system, but the same peaks dominate both spectra. We typically allow the gas-handling lines to "condition" in 10-20 Torr of each gas overnight before using a particular gas for the first time. Fresh gas samples are used each day.

Ether decomposition, as a result of adsorption at the Ru(001) sample, is measured primarily by monitoring the amount of CO and H<sub>2</sub> which desorb molecularly from the surface during the thermal desorption experiment. After correcting for background adsorption, the area under the CO or H<sub>2</sub> desorption peak for a given experiment is compared to the area under the desorption peak for saturation coverage of CO (0.67 monolayer) [15] and H<sub>2</sub> (2 monolayers) [18,19]. Our detection limits for CO and H<sub>2</sub> desorption are 0.02 and 0.3 monolayer, respectively. These values correspond to the surface coverage of CO and H<sub>2</sub> when the thermal desorption peak intensity is three times the noise intensity.

After each thermal desorption experiment, the sample is cleaned by exposure to 5 L O<sub>2</sub> (1 L  $\equiv 10^{-6}$  Torr\*s) at 525 K and subsequent heating to desorb CO. The area under the resultant CO TDS peak (which we will call

"oxidative" CO) is used to determine how much decomposition to carbon occurred during the preceding adsorption-desorption experiment. The area under the oxidative CO peak usually corresponds to less than 0.06 monolayer, and the experiment never needs to be done more than once to deplete the surface of residual carbon entirely. After desorption of oxidative CO is complete, the sample is heated and held at 1600 K for 40 seconds to deplete the surface of excess oxygen. This is repeated 2 more times to ensure complete oxygen removal.

## III. RESULTS

The data presented below share several common features, which we introduce here. First, there are two fundamentally different types of desorption features. One of these, which we denote  $\gamma$ , represents sublimation of the bulk multilayer. This state does not saturate with increasing exposure. It also exhibits characteristics of zero-order kinetic behavior (i.e., the peak temperature and full width at half maximum increase with exposure). Arrhenius plots of  $\ln(\text{Intensity})$  vs.  $1/T$  of the leading edge of such a desorption peak should yield a straight line, with a slope proportional to the sublimation energy of the compound. We refer to this as "leading edge analysis".

Second, features which lie above the  $\gamma$ -state in temperature are always observed. These states are denoted  $\alpha$  and  $\beta$ , for majority and minority states, respectively, and they are assigned a subscript which corresponds to the order in which they are filled. [We arbitrarily define a minority state as one for which the maximum peak area is less than 30% of the peak area of all the  $\alpha$ - and  $\beta$ -states combined.] Because the  $\alpha$ - and  $\beta$ -states saturate and lie at relatively high temperatures, we assign them as chemisorption states. The desorption energies associated with such states are calculated by iterating Redhead's equation for first-order desorption kinetics [20], and by assuming a pre-exponential factor of  $10^{13} \text{ s}^{-1}$ . Since there is no evidence that adsorption into these states is appreciably activated, we equate the desorption barrier to the



adsorption bond strength. Table 1 lists the desorption energies for the majority ( $\alpha$ ) states of the compounds in this study.

Finally, the analysis of the yield of decomposition products (CO and H<sub>2</sub>) for the hydrogenated ethers bears mention. We assume that all hydrogen from the decomposition products is released as H<sub>2</sub>(g). This is supported by the fact that we never observe evolution of gaseous CH<sub>4</sub>, C<sub>2</sub>H<sub>6</sub>, C<sub>2</sub>H<sub>4</sub>, or other possible decomposition products. We then compare the amount of H<sub>2</sub>(g) released to the amount of molecular CO(g) released. [These quantities are converted to absolute monolayer coverages as described in Section II.] If the C-O bond remains intact during decomposition of the molecule, then the ratio of molecular CO to hydrogen released should be the same as the ratio of oxygen to hydrogen defined by molecular stoichiometry, and we repeatedly test this hypothesis. Also, the yield of oxidative CO should correspond to the amount of carbon remaining on the surface after the first thermal ramp. This yield, however, is consistently much less than expected from molecular stoichiometry, a phenomenon which we cannot presently explain. One possibility is that the extra carbon dissolves into the Ru crystal. There is, however, no evidence in our experiments or those of others [21-24] which suggests carbon dissolves into Ru.

#### A. Diethoxymethane

Thermal desorption spectra following diethoxymethane exposure at 85 K are shown in Figure 3. Low exposure data are contained in Figure

Table 1. Desorption energies for low exposures of hydrogenated and fluorinated ethers

The values are calculated according to Redhead's method of Ref. 20, assuming  $\nu = 10^{13} \text{ s}^{-1}$ . The range of energies reflect the range of desorption peak temperatures for the majority state.

Compound	Hydrogenated Molecule Desorption Energy (kJ/mol)	Fluorinated Molecule Desorption Energy (kJ/mol)
Diethyl Ether	51-53	42-43
Diethoxymethane	53-69	-----
Diethoxyethane	58-62	44-47

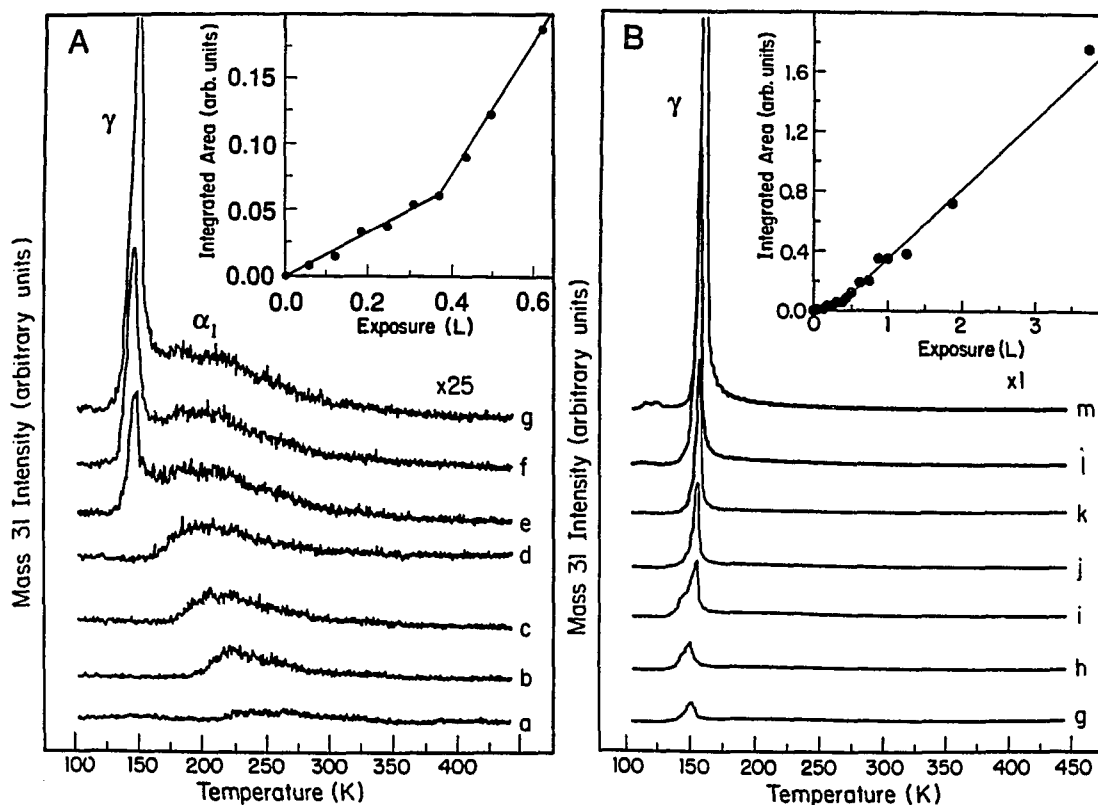


Figure 3. Thermal desorption spectra and desorption yields of diethoxymethane

(A) Thermal desorption spectra, obtained by monitoring mass 31, following exposure at 85 K to a) 0.13, b) 0.19, c) 0.25, d) 0.31, e) 0.44, f) 0.50, and g) 0.63 L diethoxymethane. The heating rate varies between 1.6 and 2.7 K/s over the temperature range 100-350 K. Inset shows the integrated area of mass 31 as a function of diethoxymethane exposure.

(B) Thermal desorption spectra, obtained by monitoring mass 31, following exposure at 85 K to g) 0.63, h) 0.75, i) 0.88, j) 1.0, k) 1.3, l) 1.9 and m) 3.8 L diethoxymethane. The heating rate varies between 1.6 and 2.7 K/s over the temperature range 100-350 K. Inset show the integrated area of mass 31 as a function of diethoxymethane exposure.

3A; higher exposure data are contained in Figure 3B. Spectra are obtained by monitoring mass 31,  $\text{CH}_3\text{O}^+$ , the most intense fragment in the cracking pattern. Experiments monitoring other fragments, such as mass 15,  $\text{CH}_3^+$ , yield equivalent spectra.

At lowest exposure, a single broad desorption state is observed, which we denote  $\alpha_1$ . This state shifts to lower temperature as exposure increases, and saturates at approximately 0.4 L as the  $\gamma$ -feature begins filling. At lowest exposure, the peak temperature of the  $\alpha_1$ -state is about 265 K. At saturation, the desorption peak maximum is about 205 K. The desorption energies associated with the  $\alpha_1$ -state are 69 to 53 kJ/mol, from low to high exposures.

For an ether exposure of 0.24 L, the  $\gamma$ -peak maximum occurs at about 145 K; at 1.9 L the peak occurs at about 160 K. Leading edge analyses of the  $\gamma$ -peak for 1.3, 1.9 and 3.8 L exposures yield a sublimation energy ( $E_s$ ) of  $55 \pm 11$  kJ/mol. For comparison, the vaporization energy of this liquid is  $35.6 \pm 0.2$  kJ/mol [25]. Sublimation energies are unavailable, but our measured value is higher than the published vaporization energy, as expected [26].

The integrated area of the mass 31 peak increases as a function of exposure, as shown by the insets of Figures 3A and B. The curve consists of two straight-line segments. The slope changes at about 0.4 L, which corresponds to first-layer completion and multilayer onset.

Decomposition of diethoxymethane is observed by molecular CO and  $\text{H}_2$  desorption, and by oxidative CO desorption following oxygen exposure, as

described in Section II. Table 2 lists the quantities measured. Table 3 shows a comparison of the ratio of molecular CO to hydrogen, based on experimental yields, with the ratio of oxygen to hydrogen based on molecular stoichiometry. This comparison shows that, within our experimental accuracy, the oxygen in diethoxymethane is quantitatively converted to CO. This implies that the C-O bond remains intact throughout decomposition of the ether. Since each ether molecule contains two oxygen atoms, the coverage of CO which desorbs is twice the coverage of diethoxymethane which decomposes. Thus, 0.05 monolayer of diethoxymethane decomposes on Ru(001). Carbon monoxide from diethoxymethane appears in a desorption-limited state [27] at ca. 465 K, similar to that shown in Figure 4A.

Hydrogen desorption after exposure to 0.88 L diethoxymethane is illustrated in Figure 4B. This exposure is sufficient to saturate the hydrogen yield. Desorption of H<sub>2</sub> begins at ca. 290-300 K and the peak maximum is at ca. 325 K. The peak exhibits a high-temperature tail. For comparison, the spectrum for a saturation coverage of hydrogen on the clean surface is shown in Figure 4E. This spectrum is in excellent agreement with results from other authors [18]. Hydrogen formed by diethoxymethane decomposition desorbs with maximum rate at temperatures about 10 K higher than for a saturation coverage of adsorbed hydrogen. Also, the peak shape of hydrogen released by the ether is significantly different.

Table 2. Decomposition of hydrogenated and fluorinated ethers

The values are calculated by comparing the peak areas to saturation coverage peak areas. The fluorinated ethers decompose to an extent below our detection limit (0.02 monolayer).

Compound	Molecular CO Monolayer	Oxidative CO Monolayer	Hydrogen Monolayer
Diethyl ether	0.04±0.02	0.02±0.01	1.7±0.5
Diethoxymethane	0.09±0.02	0.04±0.03	0.5±0.2
Diethoxyethane	0.07±0.02	0.06±0.01	0.7±0.1
Perfluorodiethyl ether	<0.02	0	-----
Perfluorodiethoxyethane	<0.02	0	-----

Table 3. Comparison between experimental and expected values of hydrogenated ether decomposition

The diether decomposition product ratio CO:H agrees, within experimental error, to the stoichiometric ratio O:H. For the monoether, however, the data do not agree with stoichiometry.

Molecule	Experimental Ratio CO:H	Stoichiometric Ratio O:H
Diethyl ether $C_4H_{10}O$	$1:43 \pm 26$ (0.4:1.7)	1:10
Diethoxymethane $C_5H_{12}O_2$	$1:6 \pm 2$ (0.09:0.5)	1:6
Diethoxyethane $C_6H_{14}O_2$	$1:10 \pm 3$ (0.07:0.7)	1:7

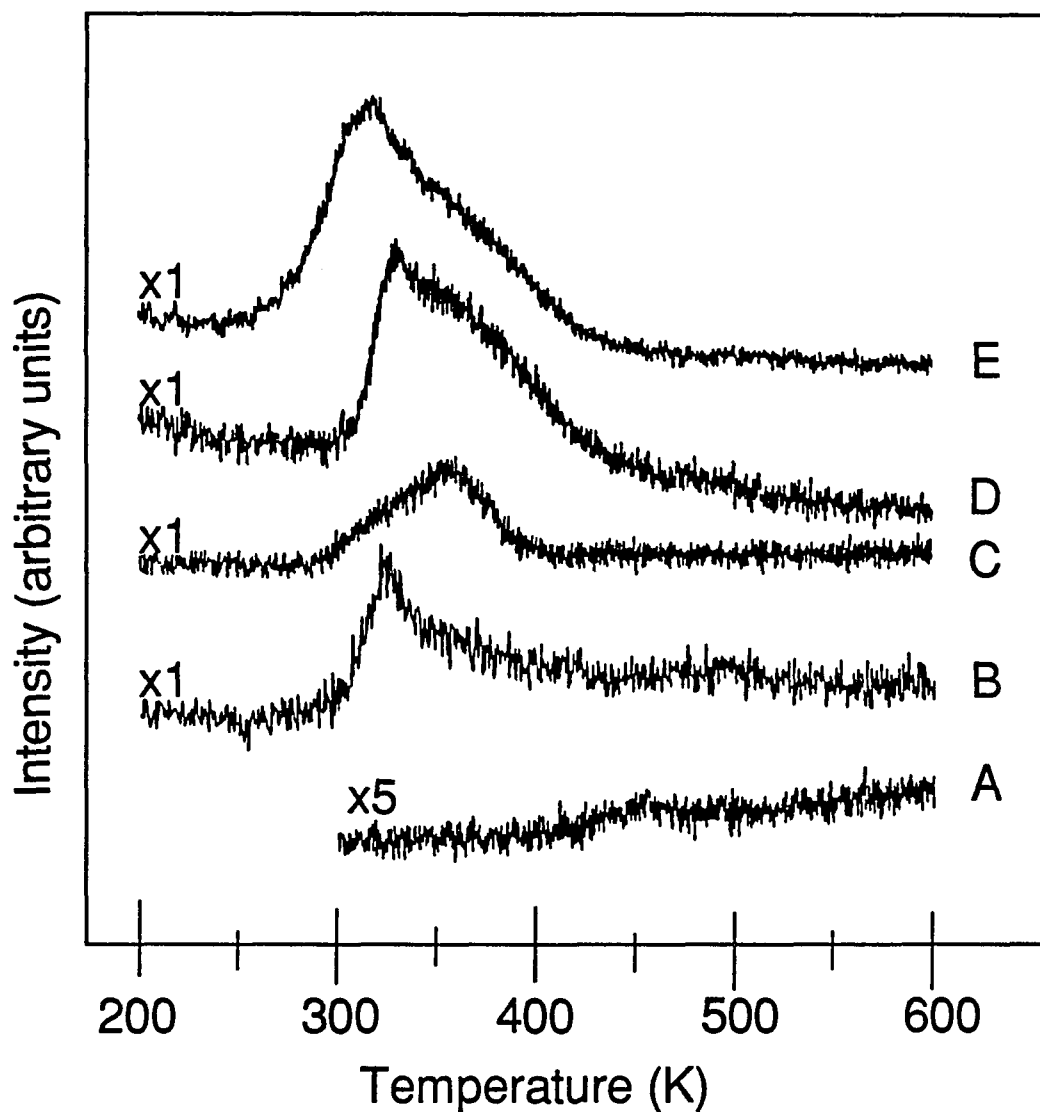


Figure 4. Decomposition product desorption

(A) Carbon monoxide desorption following exposure to 0.78 L diethoxyethane. Hydrogen desorption following (B) 0.88 L diethoxymethane, (C) 0.78 L diethoxyethane, (D) 0.25 L diethyl ether, and (E) 30 L  $H_2$ .



No desorption from masses 16, 26, 27, 29, 30, 32, 43, 44, 45, 58, or 60 is observed other than that due to cracking of diethoxymethane in the mass spectrometer ionizer. The yield of oxidative CO is a factor of five lower than expected based on molecular stoichiometry. We find, however, no evidence of methane, ethane or other hydrocarbon products, which could account for loss of the excess carbon.

### B. Diethoxyethane

Thermal desorption spectra following diethoxyethane exposure at 85 K are shown in Figure 5. Low exposure data are contained in Figure 5A; higher exposure data are contained in Figure 5B. Spectra are obtained by monitoring mass 31,  $\text{CH}_3\text{O}^+$ , the most intense fragment in the cracking pattern. Experiments monitoring other fragments, such as mass 59,  $\text{CH}_3\text{CH}_2\text{OCH}_2^+$ , yield equivalent spectra.

The low-exposure spectra for diethoxyethane contain three states. The first state,  $\beta_1$ , is observed at lowest exposures. Its peak temperature is constant at ca. 340 K. As exposure increases above 0.02 L a second peak,  $\beta_2$ , develops at about 280 K. The third state,  $\alpha_1$ , evolves at exposures greater than 0.1 L. Molecules in this state desorb at about 230 K. At exposures greater than about 0.2 L, a fourth desorption state,  $\gamma$ , is observed. This peak does not saturate with increasing exposure.

The desorption temperature of the  $\beta_1$ -state, 340 K, corresponds to a desorption energy of 90 kJ/mol. This is a minority state (hence, the  $\beta$ -

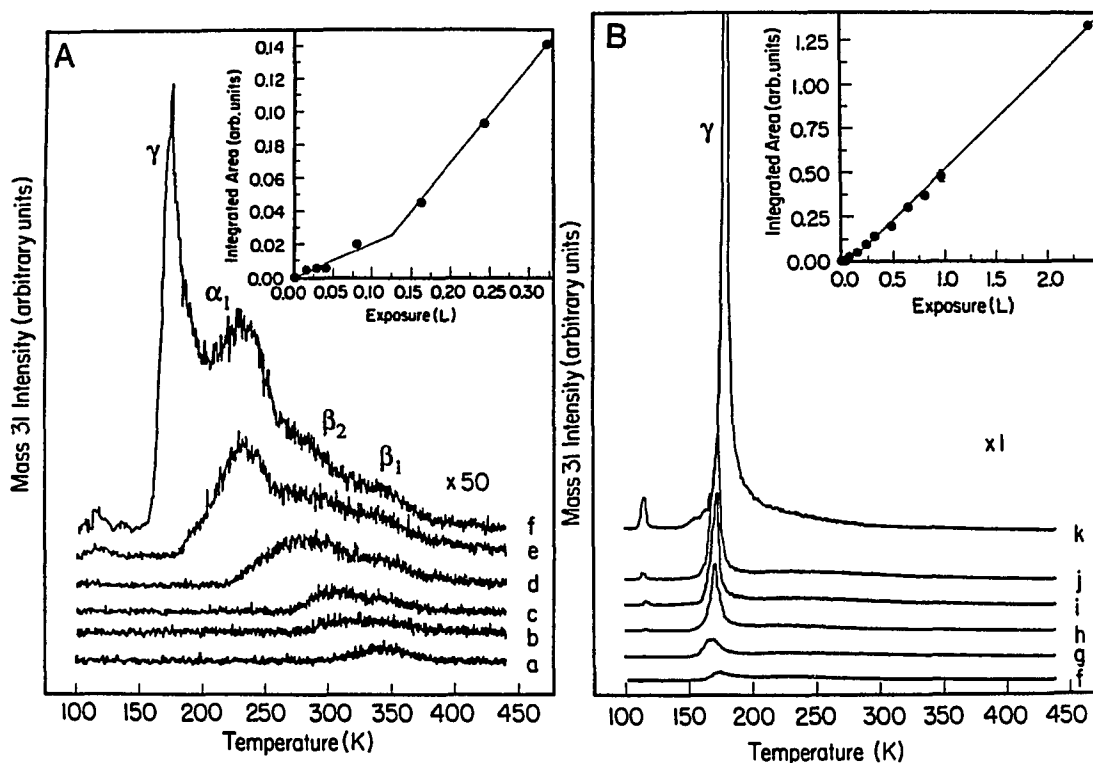


Figure 5. Thermal desorption spectra and desorption yields of diethoxyethane

(A) Thermal desorption spectra, obtained by monitoring mass 31, following exposure at 85 K to a) 0.02, b) 0.03, c) 0.04, d) 0.08, e) 0.16, and f) 0.24 L diethoxyethane. The heating rate varies between 1.6 and 2.7 K/s over the temperature range 100-350 K. Inset shows the integrated area of mass 31 as a function of diethoxyethane exposure.

(B) Thermal desorption spectra, obtained by monitoring mass 31, following exposure at 85 K to f) 0.24, g) 0.33, h) 0.49, i) 0.65, j) 0.81 and k) 2.4 L diethoxyethane. The heating rate varies between 1.6 and 2.7 K/s over the temperature range 100-350 K. Inset shows the integrated area of mass 31 as a function of diethoxyethane exposure.

designation), as it represents only 4% of the total desorption peak area of chemisorbed molecules.

The  $\beta_2$ -state also corresponds to a strongly-adsorbed species. The peak temperature, 280 K, is invariant over the exposure range studied and corresponds to a desorption energy of 73 kJ/mol. This minority state represents only 24% of the total desorption peak area of the chemisorption states.

The  $\alpha_1$ -state, the majority chemisorbed state, has a peak temperature of  $230 \pm 2$  K. The calculated desorption energy is 58-62 kJ/mol (see Table 1). The  $\alpha_1$ -state desorption peak area is 72% of the total area of the chemisorption states.

We assign the  $\gamma$ -state to desorption from a multilayer of diethoxyethane. The peak temperature of this state shifts from ca. 175 K at 0.24 L, to 180 K at 2.4 L. Leading-edge analysis of the peak from 0.81, 0.97 (not shown in Figure 5) and 2.4 L spectra yield  $E_s = 74 \pm 20$  kJ/mol, which is significantly higher than the literature value of the vaporization energy, 43.2 kJ/mol [25].

The integrated area of the mass 31 peak increases monotonically as a function of exposure, as shown in the insets of Figures 5A and B. The change in slope at about 0.12 L corresponds to the saturation of the  $\beta_1$ - and  $\beta_2$ -states and the beginning of the  $\alpha_1$ -state.

Table 2 lists the yields of molecular CO, molecular H<sub>2</sub>, and oxidative CO from decomposition of this molecule. Comparing the measured data with the molecular stoichiometry of diethoxyethane in Table 3 shows

that, within our experimental accuracy, oxygen is again converted quantitatively to CO, yielding 0.07 monolayer of molecular CO. This means that 0.04 monolayer of diethoxyethane decomposes on Ru(001). Carbon monoxide evolves in a desorption-limited state [27] at ca. 470 K, as shown in Figure 4A following a 0.78 L exposure of diethoxyethane. Hydrogen desorption after the same exposure of diethoxyethane is illustrated in Figure 4C. Higher exposures of ether do not yield increased amounts of decomposition products. Hydrogen desorption begins at 280-290 K and the peak maximum is at  $355 \pm 3$  K, over the range of exposure studied. The hydrogen desorption peak falls off sharply at higher temperature unlike the diethoxymethane-derived desorption peak (Figure 4B), which exhibits a high-temperature tail. The peak maximum for hydrogen from diethoxyethane is about 40 K higher than for a saturation coverage of adsorbed hydrogen, shown in Figure 4E, and the peak shape is significantly different. Desorption traces acquired using a variety of mass numbers including 15, 16, 18, 26, 27, 29, 30, 32, 41-46, 58-60, 72, or 74 show no features other than expected from the cracking pattern of diethoxyethane. The amount of oxidative CO measured is again a factor of five lower than expected from molecular stoichiometry. As in the case of diethoxymethane, no methane, ethane or other hydrocarbon molecules are observed desorbing from the surface.

### C. Perfluorodiethoxyethane

Since our sample of perfluorodiethoxyethane is only 94% pure and since the impurity (the monohydride) is chemically similar to the compound of interest, we compare the mass spectra for the main compound and the monohydro impurity measured via GCMS (see Section II). Figure 6 shows an abbreviated mass spectrum, both for the perfluorinated compound and the monohydro impurity. The normalized peak heights show which masses can be used to monitor perfluorodiethoxyethane, which represent the monohydro impurity and which represent both. Mass 119 is the most intense peak for both compounds. Masses 29 and 51 are unique, since they are present in the monohydro spectrum but insignificant in the perfluorodiethoxyethane spectrum. All the other masses in Figure 6 show a contribution from both compounds.

In the thermal desorption experiments, we choose to monitor masses 29, 51, 69, 100 and 185, since these provide the best opportunity to separate contributions from the two compounds. Thermal desorption spectra following perfluorodiethoxyethane exposure at 85 K are shown in Figures 7A and B. Spectra in this Figure are obtained by monitoring mass 69,  $\text{CF}_3^+$ . The integrated area of mass 69 is a linear function of exposure, as seen in the insets of Figures 7A and B. Experiments monitoring other fragments, such as masses 100,  $\text{C}_2\text{F}_4^+$ , 119,  $\text{CF}_3\text{CF}_2^+$ , and 185,  $\text{CF}_3\text{CF}_2\text{OCF}_2^+$ , yield equivalent spectra. Spectra obtained for masses 29 and 51 are different, as discussed below.

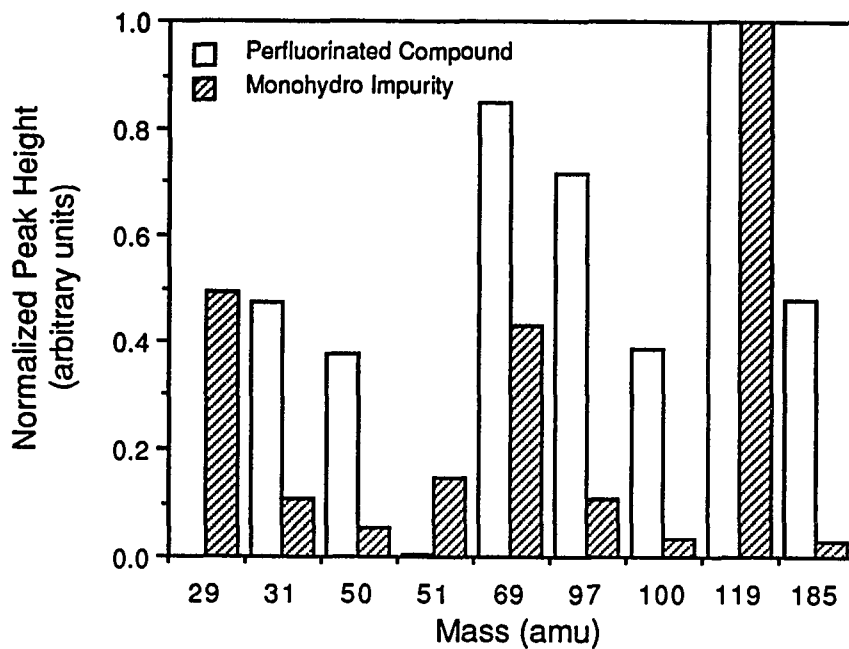


Figure 6. Mass spectrum of our sample of perfluorodiethoxyethane. Note only selected masses are shown. The dashed bars represent monohydro impurity signals; the solid bars represent signals from perfluorodiethoxyethane. The impurity signal dominates the compound signal for masses 29 and 51.

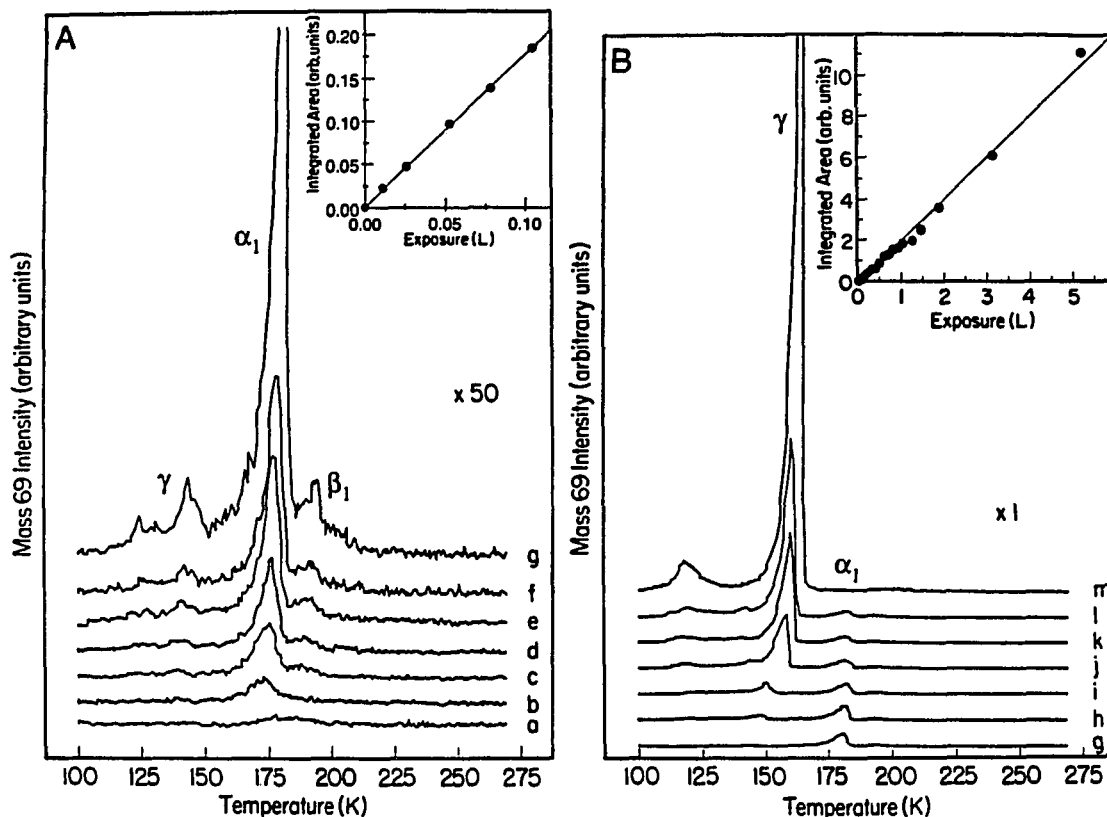


Figure 7. Thermal desorption spectra and desorption yield perfluorodiethoxyethane  
 (A) Thermal desorption spectra, obtained by monitoring mass 69, following exposure at 85 K a) 0.01, b) 0.02, c) 0.03, d) 0.04, e) 0.06, f) 0.08, and g) 0.11 L perfluorodiethoxyethane. The heating rate varies between 1.6 and 2.7 K/s over the temperature range 100-350 K. Inset shows the integrated area of mass 69 as a function of perfluorodiethoxyethane exposure.  
 (B) Thermal desorption spectra, obtained by monitoring mass 31, following exposure at 85 K to g) 0.11, h) 0.17, i) 0.22, j) 0.55, k) 0.89, l) 1.11, and m) 3.32 L perfluorodiethoxyethane. The heating rate varies between 1.6 and 2.7 K/s over the temperature range 100-350 K. Inset shows the integrated area of mass 69 as a function of perfluorodiethoxyethane exposure.

The low-exposure spectra for perfluorodiethoxyethane contain several states. The majority state,  $\alpha_1$ , begins filling at lowest exposures and saturates at about 0.1 L. A minority state,  $\beta_1$ , is observed above about 0.03 L. As exposure increases past 0.1 L, a new state at lower temperature appears initially at ca. 140 K. This state,  $\gamma$ , grows without bound as exposure increases.

We believe the  $\alpha_1$ -state corresponds to desorption from chemisorbed perfluorodiethoxyethane molecules. The peak temperature, initially at 175 K, shifts up to about 180 K at saturation, with a corresponding desorption energy of 44-47 kJ/mol. We assume first-order desorption kinetics for this state, although the highly asymmetric peak shape, visible especially in Figure 7B, suggests an effective reaction order less than unity.

The  $\beta_1$ -state, at about 195 K, is attributable to the monohydro impurity. This is based on data such as that shown in Figure 8, which displays desorption spectra for masses 29, 51, 69, 100, and 185 for a 0.89 L exposure of perfluorodiethoxyethane. The relative scales are shown at the right of the Figure. The  $\beta_1$ -peak, which is present for masses 29 and 51, clearly corresponds to desorption of the monohydro ether. The  $\alpha_1$ -state, on the other hand, is absent for these masses. This argument indicates that the  $\alpha_1$ -state corresponds to the perfluorinated ether and the  $\beta_1$ -state is from the monohydro ether. A small contribution from the monohydro ether is also observed at ca. 160 K, which overlaps with  $\gamma$ -state desorption. Thus, we conclude that



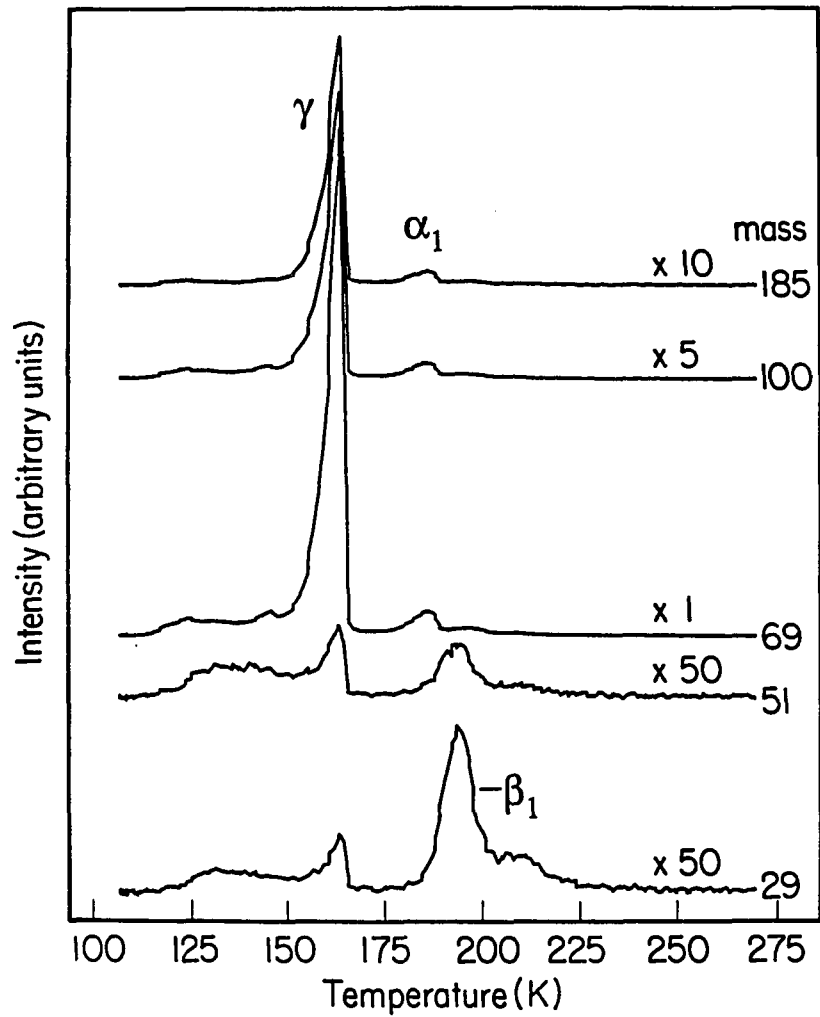


Figure 8. Thermal desorption of perfluorodiethoxyethane and the monohydro impurity

The masses shown are: 29, 51, 69, 100, and 185. The data shown follow a 0.89 L exposure.

the  $\gamma$ -state results from simultaneous sublimation of the perfluoro and monohydro compounds.

The  $\gamma$ -state exhibits multilayer characteristics. At 0.17 L the  $\gamma$ -peak desorbs at 140 K, and at 3.3 L the peak occurs at 165 K. Leading edge analysis of the 0.89, 1.1 and 3.3 L peaks yield  $E_s = 54 \pm 12$  kJ/mol. This sublimation energy actually reflects sublimation of a mixture of perfluorodiethoxyethane and the monohydro impurity. No literature values are available for the heat of vaporization of either of these compounds.

The integrated intensity of  $CF_3^+$  (mass 69) increases linearly over the entire exposure range studied. These data are shown in the insets to Figures 7A and 7B.

Decomposition of perfluorodiethoxyethane, measured by molecular and oxidative CO desorption, is less than our detection limit (0.02 monolayer). The decomposition data are listed in Table 2. No oxidative CO can be measured and this yield is, therefore, listed as zero monolayer. No desorption from masses 19, 38, 66, or 78 is observed, except that expected due to the molecular cracking pattern. Desorption of masses 29 and 51, as shown in Figure 8 and described above, is attributed to the presence of the monohydro impurity.

#### IV. DISCUSSION

In this section, we make two main comparisons. First, we contrast the measured properties of the fluorocarbons with the hydrocarbons; and second, we compare those of the diethers with the monoethers.

##### A. Fluorocarbon vs. Hydrocarbon

###### 1. Bond strength

Hydrogenated ethers are believed to bond to metal surfaces by a two-component interaction. The stronger interaction consists of electron donation from the oxygen lone pair to the metal [1-3,28], i.e., the ether acts as a simple Lewis base. The strength of this interaction is typically 40 kJ/mol [1-3,28]. Fluorination is expected to weaken this interaction because fluorine inductively depletes electron density at the oxygen.

The other component of the ether-metal bond is a weak interaction between the methylene groups and the surface. Much weaker than the oxygen-metal bond, this contributes 5 to 6.5 kJ/mol per CH<sub>2</sub> group [2,3,29,30]. This complex attraction is not attributable to hydrogen bonding, and has several opposing components [30]. Fluorination is expected to weaken this interaction as well since the C-F bond is longer than the C-H bond [31] and fluorine is more electron rich than hydrogen [32]. The carbon is held further away from the surface by the first factor; fluorine-metal repulsion is important due to the second factor.

The work reported in Paper I shows that fluorination does weaken the chemisorption bond of diethyl ether in the limit of low exposure. The bond between perfluorodiethyl ether and the Ru(001) surface is 8 to 11 kJ/mol lower than for the hydrogenated analog, diethyl ether (see Table 1). Based on the data presented in this paper (summarized in Table 1), we find that this trend is continued for fluorinated and hydrogenated diethers. The molecule-surface bond of perfluorodiethoxyethane is 11-18 kJ/mol less than the majority ( $\alpha_1$ ) chemisorption state of its hydrocarbon analog, diethoxyethane (see Table 1). Thus, we find fluorination also weakens the chemisorption bond of diethoxyethane.

## 2. Decomposition

A second characteristic difference between the hydrogenated and fluorinated ethers is that a greater extent of decomposition occurs for hydrogenated ethers. About 0.04 to 0.17 monolayer of these species undergo decomposition. As shown in Table 2, diethyl ether, diethoxymethane and diethoxyethane liberate 0.04, 0.09 and 0.07 monolayer of molecular CO and 1.7, 0.5 and 0.7 monolayers of hydrogen, respectively. On the other hand, the fluorinated ethers, perfluorodiethyl ether and perfluorodiethoxyethane, liberate less CO than we can detect (<0.02 monolayer). Table 3 illustrates the experimentally observed and stoichiometrically expected amounts of CO and H<sub>2</sub> for the hydrogenated ethers. The agreement between the measured ratio and the expected ratio is quite good for the diethers, allowing us to conclude

that oxygen is quantitatively released as molecular CO in the decomposition of the diethers. For diethyl ether, on the other hand, only about 20% of the decomposed diethyl ether molecules liberate CO. Clearly, the decomposition mechanism of the monoether differs from that of the diethers.

To estimate what fraction of adsorbed ether molecules decompose, we estimate the surface coverage of ether based on molecular cross section [33]. The molecular cross section is the area of the surface occupied by an adsorbed molecule [33]. If an ether molecule lies along the surface with a staggered antiperiplanar configuration about each C-C and C-O bond, it occupies the largest surface area of all possible configurations. As an upper bound, we will consider this orientation. From the procedures outlined in Reference 33, we estimate the molecular cross section of diethyl ether, diethoxymethane, diethoxyethane, perfluorodiethyl ether and perfluorodiethoxyethane as 32.1, 42.3, 47.4, 49.8 and 76.1 Å<sup>2</sup>, respectively. These molecules, oriented on the Ru(001) surface as described above, will exclude an area equal to 5.1, 6.7, 7.5, 7.9 and 12.1 Ru atoms, assuming perfect and nonsite-specific packing. Thus, the maximum absolute surface coverage of ether is 0.20, 0.15, 0.13, 0.13 and 0.08 monolayer, respectively. The extent of decomposition which we measure, relative to the maximum absolute coverage of ether in the first layer, is 0.85, 0.26, 0.38, <0.15 and <0.25, respectively. Perhaps the low absolute coverage of fluorinated ether molecules prevents the observation of decomposition products. The numbers listed above assume

the molecules lie flat on the surface and pack perfectly. Any deviation from either a flat orientation or perfect packing would decrease the absolute coverage of ether, and the relative extent of decomposition would be larger.

Hydrogen desorption from ether decomposition, illustrated in Figure 4, also indicates fundamental differences between the decomposition pathways of the hydrogenated ethers. The hydrogen desorption peak from diethyl ether decomposition, shown in Figure 4D, resembles the desorption peak from adsorbed hydrogen, shown in Figure 4E. The onset of hydrogen desorption resulting from diethyl ether decomposition is about 40 K higher than for a saturation coverage of pure hydrogen. This shift in the onset of hydrogen desorption may suggest that hydrogen evolution from the surface exposed to the ether is perturbed by co-adsorbed decomposition products or is reaction-limited.

Hydrogen desorption from decomposition of the two diethers (Figures 4B and 4C) is strikingly different. For diethoxymethane, in Figure 4B, the hydrogen desorption begins at ca. 290-300 K and peaks at ca. 325 K. On the other hand, hydrogen desorption from diethoxyethane, in Figure 4C, begins at ca. 280-290 K and peaks at ca. 355 K. These differences in the temperatures of hydrogen evolution and the desorption peak shapes suggest different decomposition mechanisms for these molecules as well.

Figure 9 illustrates the possible combinations of diether decomposition products which are consistent with stoichiometric evolution of oxygen as CO. As shown in Figure 9A, diethoxymethane can decompose to

give either one  $C_2$  and one  $C_1$  (Figure 9A scheme i) or three  $C_1$  (Figure 9A scheme ii) surface species. Diethoxyethane, shown in Figure 9B, can decompose to one  $C_2$  species and two  $C_1$  species in two ways (Figure 9B schemes i and ii) or to two  $C_2$  species (Figure 9B scheme iii).

The  $C_2$  species ethylidyne ( $\equiv C-CH_3$ ) is relatively stable on Ru(001) and decomposes to yield acetylide ( $-C\equiv CH$ ) and gaseous hydrogen at ca. 330 K [21-23]. The acetylide species decomposes at ca. 380 K to form methylidyne ( $\equiv CH$ ) [21-23]. The methylidyne decomposes at temperatures  $\geq 500$  K to give additional hydrogen and residual carbon [21,22,24]. Thus, for ether decomposition, if the principal decomposition product is a  $C_2$  species, hydrogen desorption is expected around 330-350 K with a higher temperature ( $\geq 500$  K) state. If decomposition yields only  $C_1$  fragments, presumably methylidyne among them, hydrogen desorption is expected at higher temperatures ( $\geq 500$  K).

In the hydrogen desorption spectra for diethoxymethane, illustrated in Figure 4B, there is a small feature at ca. 500 K. In the diethoxyethane hydrogen desorption spectra, represented in Figure 4C, no high-temperature feature is apparent. All the decomposition schemes proposed in Figure 9, however, require decomposition of surface methylidyne. In some cases the methylidyne results directly from ether fragmentation (e.g., Figure 9A path ii); in other cases it results from

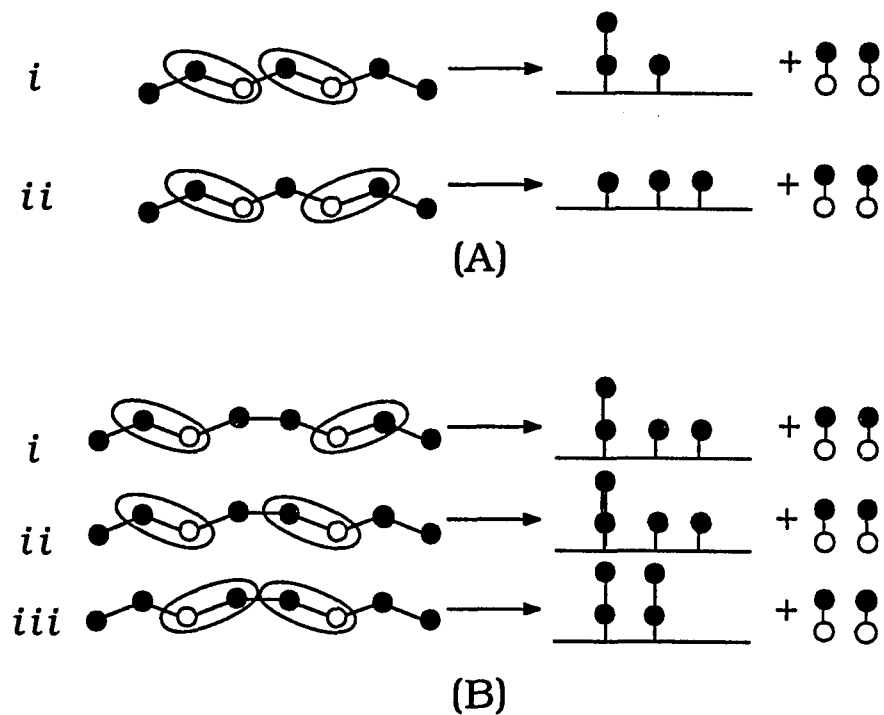


Figure 9. Possible decomposition products of diethers adsorbed on Ru(001)

(A) Diethoxymethane. (B) Diethoxyethane. The filled circles represent carbon atoms; the open circles represent oxygen atoms.



ethylidyne decomposition (e.g., Figure 9B path iii). Insight into why we observe no high-temperature hydrogen desorption feature for diethoxyethane may be gained by analysis of the relative areas of the low- and high-temperature hydrogen desorption features.

In the following argument, we consider ethylidyne, acetylide, methylidyne and hydrogen adatoms as candidates for the surface species produced in ether decomposition, with CO as a gas-phase product. As an illustration, consider the decomposition pathway specified in Figure 9A scheme i. When an ether molecule decomposes eight hydrogen atoms are liberated: two from the resulting ethylidyne fragment, two from the resulting methylidyne fragment, and two from each of the resulting CO molecules. The ethylidyne fragments decompose at ca. 330 K, yielding two hydrogen atoms and an acetylide fragment. The low-temperature (ca. 325-350 K) hydrogen desorption state of the hydrogenated ethers probably results from desorption of these ten hydrogen atoms. The adatoms resulting from ethylidyne decomposition would be expected to desorb at slightly higher temperatures than those evolved in ether fragmentation. Decomposition of acetylide to methylidyne fragments, at ca. 380 K, does not liberate any hydrogen atoms. The methylidyne fragments decompose at higher temperatures to provide the remaining two hydrogen atoms. These two hydrogen atoms desorb in the high-temperature state at ca. 500 K.

Thus, in this scheme, the relative areas of the low- and high-temperature hydrogen peaks are expected to be 5:1. For the other schemes

outlined in Figure 9, the expected relative peak areas are 3:1, 3.6:1, and 6:1 for schemes 9A ii, 9B i or ii, and 9B iii, respectively.

The measured relative areas of the low- and high-temperature hydrogen peaks for diethoxymethane (Figure 4B) is 5:1, suggesting decomposition occurs via the path specified in Figure 9A i. The main hydrogen desorption feature occurs at ca. 325 K, about the decomposition temperature of ethylidyne. This peak probably results from adatoms produced in a lower-temperature decomposition step (e.g., ether fragmentation). In other words, the hydrogen desorption peak at ca. 325 K is primarily desorption-limited. Note, however, that this feature has a long high-temperature tail. Hydrogen desorption from ethylidyne decomposition may occur in this temperature range. The high-temperature tailing of the low-temperature peak suggests that some ethylidyne fragments are formed in diethoxymethane decomposition (i.e., Figure 9A path i).

The high-temperature hydrogen state for diethoxyethane (Figure 4C) is not observed in the thermal desorption spectrum. This could result from a small relative population of the low-temperature state. If, for example, the relative areas are 6:1 as specified in the path illustrated in Figure 9B scheme iii, the high-temperature feature may not be observed.

In view of these facts, it appears that diethoxyethane decomposes to yield the products specified in Figure 9B path iii. This assignment is reasonable since hydrogen desorption occurs in the temperature range

expected for  $C_2$  fragment decomposition. This scheme yields a low relative area for the low- and high-temperature states. For this reason, hydrogen desorption resulting from  $C_1$  species decomposition may not be observed.

We believe the instability of the hydrogenated ethers with respect to the fluorinated ethers is also reflected in the desorption yield as a function of exposure. The desorption yield is obtained by integrating the area under the thermal desorption trace. These integrated area vs. exposure functions are plotted in the insets to Figures 3, 5, and 7 for diethoxymethane, diethoxyethane and perfluorodiethoxyethane, respectively. Figure 10 shows the desorption yield curves for the monoethers: diethyl ether and perfluorodiethyl ether. It is clear that, for the hydrogenated ethers, the desorption yield increases slowly at low exposures, and much more rapidly at higher exposures. The break in each curve approximately coincides with the beginning of adsorption into the  $\gamma$ -state (the multilayer). In contrast, the desorption yield of each fluorinated ether varies linearly with exposure over the entire exposure range (see Figures 7 and 10). This pattern suggests that the change in slope for the hydrogenated compounds is not due to a change in sticking coefficient, but rather reflects the fact that a constant fraction of the chemisorbed molecules dissociate rather than desorb. Thus, the number of hydrogenated molecules desorbing from the surface in the low exposure regime is less than the number adsorbed, leading to a relatively low desorption yield at low exposures.

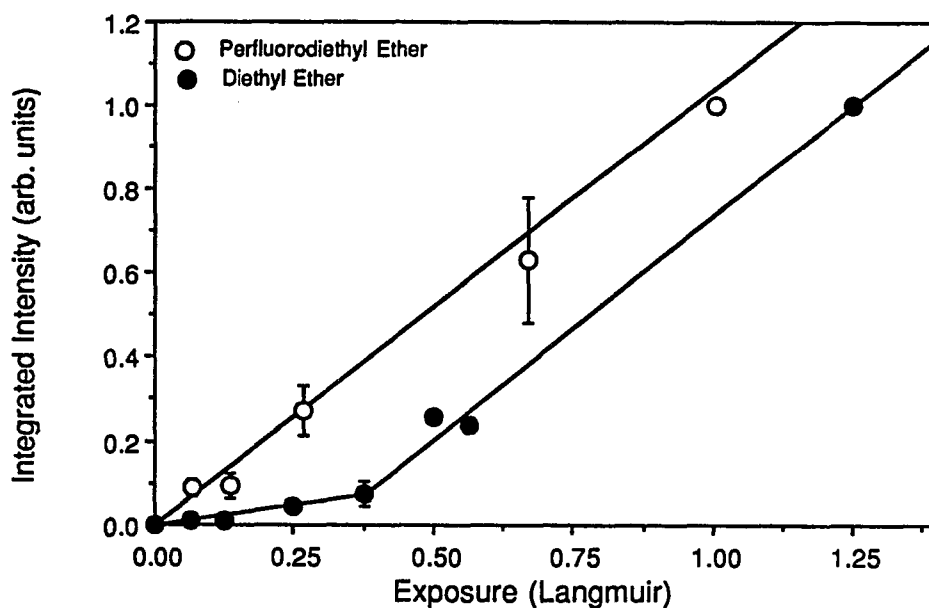


Figure 10. Desorption yield plots for the monoethers

The open circles represent perfluorodiethyl ether; the black circles represent diethyl ether. For the fluorinated compound, the desorption yield increases monotonically over the entire exposure range. For diethyl ether, the curve has a lower slope at low exposures, when the  $\alpha$ -states are populated.

We believe this decomposition trend is also reflected in the thermal desorption peak shapes. Thermal desorption spectra of fluorinated ethers show sharp peaks which do not shift in temperature significantly as exposure increases. The thermal desorption spectra of hydrogenated ethers, on the other hand, characteristically show broad peaks which may shift to lower temperatures as exposure increases. This trend is especially true for diethoxymethane. The peak broadness may be due to the changing condition of the surface during desorption: i.e., decomposition and desorption are competitive processes during the thermal desorption ramp.

The greater stability of chemisorbed fluorinated ethers, relative to hydrogenated ethers is supported by the experimental facts discussed above. In order to discuss the factors which might account for this, first consider the decomposition mechanism of an ether, which may resemble that of a chemisorbed alkoxide. The rate-determining step in the decomposition of surface ethoxide on Ni(111) is C-H bond breaking at the  $\alpha$ -carbon, which occurs at ca. 260 K [34]. Surface methoxide decomposes at ca. 220 K on Ru(001) to give CO and adsorbed hydrogen [35].

If a similar mechanism operates in the decomposition of ethers, we expect C-H bond cleavage to begin around 220 K on Ru(001). Chemisorbed diethoxymethane and diethoxyethane both remain on the surface up to this temperature. Decomposition via C-H bond breaking at an  $\alpha$ -carbon is, therefore, a reasonable decomposition mechanism for these diethers.

In the fluorinated ether case, however, decomposition via analogous C-F bond breaking would presumably require a higher substrate temperature because the C-F bond (480 kJ/mol in  $C_2F_6$  [36]) is stronger than the C-H bond (406 kJ/mol in  $C_2H_6$  [37]). This argument assumes the difference in activation barriers to dissociation for the adsorbed molecules are similar to the differences in bond dissociation energies for the gas phase species, which are the values listed above. Since both fluorinated ethers desorb below ca. 180 K, decomposition via C-F bond breaking may be circumvented because desorption precedes decomposition. This is contrary to the hydrogenated diether case, described above, where desorption and decomposition are probably competing processes during the thermal desorption experiment.

Alternatively, a difference in the bonding geometries of fluorinated and hydrogenated ethers could account for the fluorocarbon stability. Due to repulsion between electron-rich fluorine atoms and the metal surface, the alkyl side chains of a fluorinated ether may not approach the surface as closely as the alkyl groups of a hydrogenated ether (see Figure 11, described below), resulting in a lower propensity for C-F bond cleavage.

## B. Mono vs. Diethers

### 1. Bond Strength

Diethers, since they have two functional groups, can bond to the surface in a variety of ways. Figure 11 illustrates several bonding

possibilities for both mono- and diethers. The intramolecular strain in any of these configurations is very low. Diethyl ether, shown in Figure 11A, bonds primarily through the oxygen atom. The aliphatic side chains can either approach the surface closely, shown on the left, or be held remotely from the surface, shown on the right. A previous study by Rendulić and Sexton [3] suggests that only one ether side chain is involved in bonding to Pt(111) surfaces. An illustration of this type of bonding configuration is shown in the center of Figure 11A.

Diethers can bond to the surface in a number of configurations, two of which are illustrated in Figure 11B and C. As shown on the far left, both oxygen atoms can bond to the surface. The Ru(001) substrate provides a good match for the interatomic distances of the diethers. Thus, the diethers may bond to the surface via both oxygen atoms. Molecules bonded in such an  $\eta^2(0,0)$ -configuration should have strong ether-surface bonds: about 80 kJ/mol, as a first approximation. Alternatively, only one oxygen could bond to the surface. Such a  $\eta^1(0)$ -configuration is shown at the right of Figure 11B and C.

Diethers can (in principle) bond more strongly to surfaces than monoethers. For the hydrogenated monoether, diethyl ether, the strength of the chemisorption bond on Ru(001) is 51-53 kJ/mol (see Table 1). The majority species for both hydrogenated diethers, diethoxymethane and diethoxyethane, are significantly more strongly bonded (22% and 35% respectively) than diethyl ether. For the fluorinated ethers, on the other hand, perfluorodiethoxyethane-surface bonds are only 12% stronger

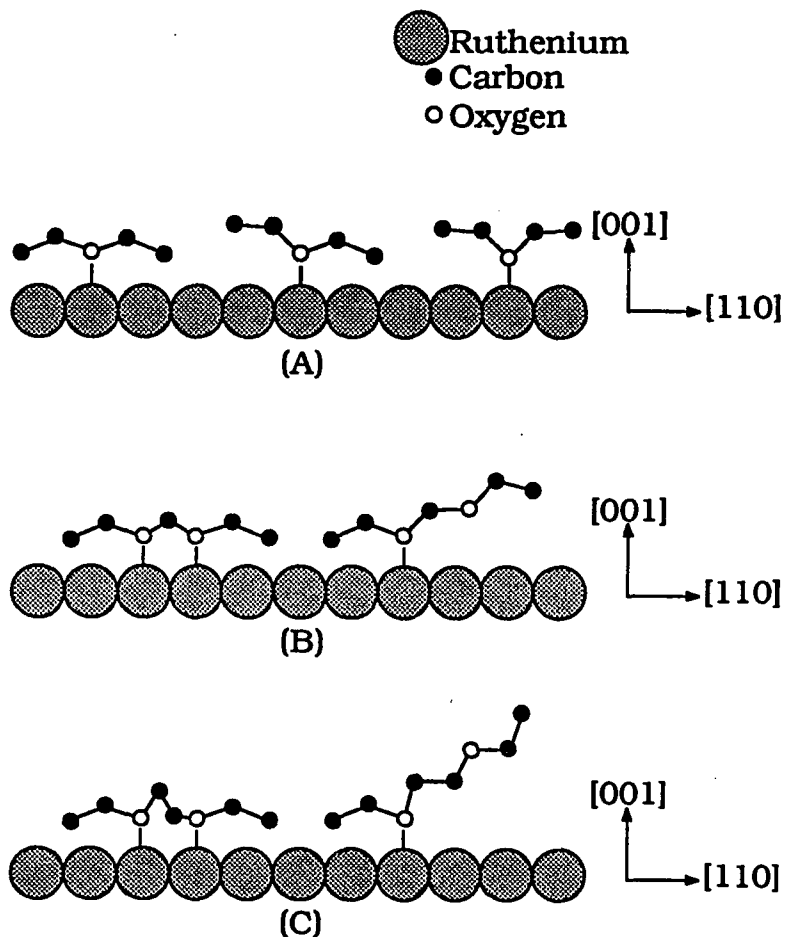


Figure 11. Scale model of ether molecules bonded to Ru(001)

(A) Diethyl ether bonds primarily through the oxygen. The side chains can approach the surface or stay away from it, depending on the circumstances (e.g., fluorinated vs. hydrogenated side chains, electronegativity of the substrate). (B) Diethoxymethane can bond to the surface via one or both oxygens. (C) Diethoxyethane can bond to the surface via one or both oxygens.



than perfluorodiethyl ether-surface bonds. Thus, the fluorinated mono- and diethers appear to both bond via one oxygen-metal interaction. The added bulk of the fluorine atoms may sterically prohibit both oxygen atoms from bonding to the surface.

The observed increase in hydrogenated diether bond strength may be attributed to either of two possible scenarios. First, the stronger diether-surface bonds can result from bonding through both oxygen atoms. Since the observed bond strengths are only ca. 60 kJ/mol, one or both oxygen-metal bonds are much weaker than 40 kJ/mol. An oxygen-metal bond is formed by electron donation to the metal by the oxygen lone pair electrons. It is reasonable, therefore, to expect a second oxygen-metal bond in close proximity to be weakened due to a locally high electron density.

Second, the increased bond strength for hydrogenated diethers may be attributed to the additional methylene groups in the diethers. This requires, however, that only one side chain of the monoethers interact with the surface while all the methylene groups in the alkyl chains of the diethers interact with the surface.

Although both of these bonding schemes are consistent with the data, we cannot distinguish between the two bonding modes. Other experimental data, such as that obtained from EELS experiments, are needed to confirm the diether bonding configuration.

## 2. Decomposition

We observe no appreciable difference between the amounts of decomposition of fluorinated monoethers and fluorinated diethers. Both molecules decompose less than our detection limit. For the hydrogenated ethers, on the other hand, the monoether decomposes about three times more than the diethers. This, as well as the fact that only about 20% of the oxygen atoms are released as CO molecules, suggests an alternate decomposition mechanism for diethyl ether. However, no other oxygen-containing desorption products, such as ethanol, methanol, acetaldehyde or formaldehyde, are observed. Hydrogen desorption data suggest that diethoxymethane decomposes to yield both adsorbed C<sub>1</sub> and C<sub>2</sub> species, while diethoxyethane decomposition gives primarily C<sub>2</sub> species.

## V. CONCLUSIONS

Fluorinated ethers bond more weakly to Ru(001) than hydrogenated ethers. This result includes diethers as well as monoethers. The relative bond strengths are explained primarily in terms of inductive depletion of electron density at the oxygen lone pair by the fluorine substituents. Fluorinated diethers are more stable toward decomposition on Ru(001) than are the hydrogenated species. This is attributed to the temperature required to activate the C-F or C-H bonds, the desorption temperature of the chemisorbed molecules or a difference in bonding geometry.

Hydrogenated diethers bond to Ru(001) between 22% and 35% more strongly than the monoether. This increase in bond strength can be attributed either to the extra methylene groups or the extra oxygen atom in the diethers. Only a small increase in bond strength is observed on adding an ether linkage to perfluorodiethyl ether. This suggests that both the fluorinated mono- and diether bond to Ru(001) in the same configuration.

Fluorinated mono- and diethers both decompose insignificantly. The hydrogenated mono- and diethers appear to decompose according to different mechanisms.

## VI. ACKNOWLEDGEMENTS

We sincerely thank Dr. Tom Bierschenk of Exfluor Research Corp. for providing the 1,2-perfluorodiethoxyethane. We thank T. J. Barton and J. L. Davis for valuable discussions and R. L. Lockridge for help in preparing Figures for this manuscript. This research is supported by the Director for Energy Research, Office of Basic Energy Sciences. Ames Laboratory is operated for the U.S. Department of Energy by Iowa State University under Contract No. W-7405-ENG-82.

## VII. REFERENCES

1. H. Lüth, G. W. Rubloff, W. D. Grobman, *Surface Science*, 63 (1977) 325.
2. B. A. Sexton and A. E. Hughes, *Surface Science*, 140 (1984) 227.
3. K. D. Rendulić and B. A. Sexton, *J. Catalysis*, 78 (1982) 126.
4. A. B. Anton, N. R. Avery, B. H. Toby and W. H. Weinberg, *J. Am. Chem. Soc.*, 108 (1986) 684.
5. J. L. Davis and M. A. Barteau, *Surface Science*, 187 (1987) 387.
6. M. A. Henderson, P. L. Radloff, J. M. White and C. A. Mims, *J. Phys. Chem.*, 92 (1988) 4111.
7. M. A. Henderson, P. L. Radloff, C. M. Greenlief, J. M. White and C. A. Mims, *J. Phys. Chem.*, 92 (1988) 4120.
8. T. J. Brice and R. I. Coon, *J. Am. Chem. Soc.*, 75 (1953) 2921.
9. W. R. Jones, Jr., K. J. L. Paciorek, T. I. Ito, and R. H. Kratzer, *Ind. Eng. Chem. Prod. Res. Dev.*, 22 (1983) 166.
10. W. R. Jones, Jr., K. J. L. Paciorek, D. H. Harris, M. E. Smythe, J. H. Nakahara and R. H. Kratzer, *Ind. Eng. Chem. Prod. Res. Dev.*, 24 (1985) 417.
11. W. R. Jones, Jr., K. J. L. Paciorek, J. H. Nakahara, M. E. Smythe and R. H. Kratzer, *Ind. Eng. Chem. Res.*, 26 (1987) 1930.
12. A. L. Johnson, Ph.D. Thesis, University of California, Berkeley, 1986.

13. L. Ng, J. G. Chen, P. Basu and J. T. Yates, Jr., *Langmuir*, 3 (1987) 1161.
14. M. A. B. DeMoraes and D. Lichtman, *Surface Science*, 160 (1985) 362.
15. E. D. Williams and W. H. Weinberg, *Surface Science*, 82 (1979) 93.
16. P. A. Thiel and J. W. Andereg, *Rev. Sci. Instrum.*, 55 (1984) 1669.
17. H. Herz, H. Conrad and J. Küppers, *J. Phys. E.*, 12 (1979) 369.
18. P. Feulner and D. Menzel, *Surface Science*, 154 (1985) 465.
19. M. Y. Chou and J. R. Chelikowsky, *Phys. Rev. Lett.*, 59 (1987) 1737.
20. P. A. Redhead, *Vacuum*, 12 (1962) 203.
21. M. M. Hills, J. E. Parmenter, C. B. Mullins and W. H. Weinberg, *J. Am. Chem. Soc.*, 108 (1986) 3554.
22. J. E. Parmenter, M. M. Hills and W. H. Weinberg, *J. Am. Chem. Soc.*, 108 (1986) 3563.
23. M. M. Hills, J. E. Parmenter and W. H. Weinberg, *J. Am. Chem. Soc.*, 108 (1986) 7215.
24. M. A. Barteau, P. Feulner, R. Stengl, J.Q. Broughton and D. Menzel, *J. Catalysis*, 94 (1985) 51.
25. J. B. Pedley, R. D. Naylor and S. P. Kirby, Thermochemical Data for Organic Compounds 2nd edition (Chapman and Hall Ltd., London, 1986).
26. P. W. Atkins, Physical Chemistry 2nd edition (W.K. Freeman and Co., San Francisco, 1978) 181.
27. T. E. Madey and D. Menzel, *Japanese J. Appl. Phys.*, 13 Supp. 2, Part 2 (1974) 229.
28. P. A. Thiel and T. E. Madey, *Surface Science Reports*, 7 (1987).

29. T. E. Madey and J. T. Yates, Jr., *Surface Science*, 76 (1978) 397.
30. F. M. Hoffmann and T. H. Upton, *J. Phys. Chem.*, 88 (1984) 6209.
31. A. D. Mitchell and L. C. Cross, Eds., Tables of Interatomic Distances and Configurations in Molecules and Ions (Burlington House, London, 1958).
32. R. D. Chambers, Fluorine in Organic Chemistry (John Wiley and Sons, New York, 1973).
33. A. Gavezzotti, M. Simonetta, M. A. Van Hove and G. A. Somorjai, *Surface Science*, 154 (1985) 109.
34. S. M. Gates, J. N. Russell, Jr., and J. T. Yates, Jr., *Surface Science*, 171 (1986) 111.
35. J. Hrbek, R. A. dePaola and F. M. Hoffmann, *J. Chem. Phys.*, 81 (1984) 2818.
36. M. Stacey, J. C. Tatlow and A. G. Sharpe, Advances in Fluorine Chemistry Vol. 2 (Butterworths, London, 1961).
37. V. I. Vedeneyev, L. V. Gurvich, V. N. Kondratyev, V. A. Medvedev and Y. L. Frankevich, Bond Energies, Ionization Potentials and Electron Affinities (Edward Arnold Ltd., London, 1966).

PAPER III:

CYCLIC ETHERS ADSORBED ON RU(001):  
CHEMISORBED AND METASTABLE ADSORPTION STATES



CYCLIC ETHERS ADSORBED ON RU(001):  
CHEMISORBED AND METASTABLE ADSORPTION STATES

M.M. Walczak and P.A. Thiel

Department of Chemistry and Ames Laboratory  
Iowa State University  
Ames, Iowa 50010

## ABSTRACT

The cyclic ethers 1,3-dioxane, 1,4-dioxane and 1,3,5-trioxane desorb from Ru(001) in several states. The thermal desorption spectra of each compound exhibit chemisorbed, metastable and multilayer states. The bond strengths of the majority chemisorption states fall between 45 and 58 kJ/mol. The two dioxanes exhibit low-temperature metastable states which, for fast heating rates, are populated at the expense of the true multilayer states. The low-temperature state of 1,3,5-trioxane, on the other hand, is not significantly influenced by changing the sample heating rate between 0.2 and 2.3 K/s. The inherent stability of the metastable state of 1,3,5-trioxane against conversion is attributed to the stable crystalline structure of the compound.

## I. INTRODUCTION

In Paper II of this dissertation we report that the linear hydrogenated diethers 1,2-diethoxyethane and 1,1'-[methylenebis(oxy)]-bisethane desorb from Ru(001) in a number of states. The desorption energy of the majority state falls in the range 53 to 69 kJ/mol for both of these compounds. This bond strength is up to 35% higher than that of the monoether, diethyl ether, on Ru(001) (see Paper I). This increase suggests the linear hydrogenated diethers may bond to the substrate either via two weak oxygen-metal bonds or via one oxygen-metal bond and several methylene groups. Both of these schemes can be explained by a local increase in electron density. Such an increase occurs on electron donation from the oxygen lone pair to the metal on formation of an oxygen-metal bond.

We also find that 0.04 to 0.05 monolayer of the linear hydrogenated diethers decompose on Ru(001). The decomposition of these molecules may be attributed to the strengths of the adsorption bond and/or the C-H bond. The ethers may decompose because they remain on the surface up to temperatures required to initiate decomposition, which may occur via C-H bond cleavage.

In this paper, we extend our studies of ether molecules adsorbed at the Ru(001) surface to include a series of cyclic ethers: 1,3-dioxane, 1,4-dioxane and 1,3,5-trioxane. Each compound is a six-membered-ring, with oxygen atoms at two or three of the positions occupied by carbon

atoms in cyclohexane, the related saturated hydrocarbon. By virtue of their molecular structure, cyclic ethers may bond to the substrate via two or three oxygen atoms which potentially can determine whether oxygen-metal bonds in close proximity are weaker than their isolated counterparts. Because cyclohexane is the natural analog of the cyclic ethers, we first review the established information about this compound.

Cyclohexane,  $C_6H_{12}$ , can exist in either the chair or boat conformation. The chair form, in which the carbon atoms alternate up and down around the ring, is thermodynamically favored at room temperature [1]. The energy difference between the chair and boat conformations of cyclohexane is 23 kJ/mol [2].

Cyclohexane has been studied extensively on Ru(001) [3-5]. Thermal desorption studies show a single chemisorbed state which has a desorption energy between 38 [5] and 59 [3] kJ/mol. Cyclohexane adsorbs on Ru(001) in the chair configuration, with the carbon skeleton oriented parallel to the surface. Three axial hydrogens are directed into threefold hollow sites in the Ru(001) lattice. This bonding configuration for cyclohexane is supported by Electron Energy Loss Spectroscopy (EELS) [4] and Electron Stimulated Desorption Ion Angular Distribution (ESDIAD) [3] data. The position of the Ru atoms in the substrate provides an excellent match to the geometry of the cyclohexane molecule [3,4].

The cyclic ethers are structurally similar to cyclohexane. The C-O bonds in the ethers (1.4 Å [6]), however, are slightly shorter than the C-C bonds in cyclohexane (1.5 Å [6]). As a result, the 1,3-dioxane, 1,4-

dioxane and 1,3,5-trioxane molecules are slightly smaller than the cyclohexane molecule.

A more significant difference between the cyclic ethers and cyclohexane is the replacement of methylene groups with oxygen atoms. This is expected to greatly influence the chemisorption of the ethers. The surface chemistry of other oxygen-containing molecules is dominated by the oxygen moiety. For example, the adsorption bond strength for *n*-butane on Cu(100) is 38 kJ/mol, while for the related oxygen-containing compound, *n*-propyl ether, the interaction is 54 kJ/mol [7]. Both of these molecules are believed to interact with the substrate via four bonds [7]. The hydrocarbon interacts via four CH<sub>x</sub> groups; the ether interacts with three CH<sub>x</sub> moieties and one oxygen atom. Thus, the oxygen-metal interaction strengthens the overall adsorption bond considerably compared to another CH<sub>x</sub>-metal interaction. The oxygen-metal bond is formed by electron donation from the oxygen lone pair to the metal [7-10]. As a result, the local electron density is increased. Based on data from other oxygen-containing molecules [7-10], we expect the surface chemistry of the cyclic ethers to be dominated by the oxygen atoms.

The cyclic ethers adsorb on Ru(001) in several states. In addition to the chemisorbed ether states, the cyclic ethers also desorb in very low-temperature (ca. 150-175 K) states. The population of some of these states changes as a function of sample heating rate. Such states are attributed to molecules which are kinetically "frozen" in a particular configuration on adsorption [11]. If the sample heating rate is slow,

conversion to a more-stable adsorption state can occur before desorption. Such metastable states are observed for 1,3- and 1,4-dioxane. Thermal desorption spectra of the third cyclic ether, 1,3,5-trioxane, also exhibit a low-temperature state. The population of this state, however, is not influenced by changing the sample heating rate from 0.2 to 2.3 K/s. The low-temperature state is, therefore, not metastable for 1,3,5-trioxane in this range of heating rates.

Similar metastable states have been reported also for benzene on Ru(001) [11,12], Mo(110) [13] and Ni(100) [14]. For benzene on Ru(001), the metastable state is attributed to a multilayer strongly influenced by chemisorbed phases of benzene [12]. At higher exposures, the metastable state is no longer observed; desorption from bulk-like benzene is observed. The metastable states of 1,3- and 1,4-dioxane are quite similar to those observed for benzene on Ru(001). The metastable states are observed only in a narrow exposure range (0.54 to 1.7 L) just as multilayer state formation begins.

## II. EXPERIMENTAL

The experiments are performed in an ion-pumped, stainless steel UHV chamber equipped with a pinhole-aperture gas doser, a UTI-100C mass spectrometer, an Auger spectrometer and ESDIAD/LEED optics. The experimental apparatus is described in detail in Paper II of this thesis. Of special interest in this paper are the sample heating rates. The crystal is heated resistively using a feedback circuit [15] which ramps linearly in millivolts. For the experiments reported in this paper, heating rates of 0.1, 0.2, 1.0 or 2.0 mV/min are used. Since, for the W-5% Re vs. W-26% Re thermocouple, the conversion between thermocouple output (mV) and temperature (K) is nonlinear [16,17], the heating rate (K/s) varies during the course of the experiment. Over the temperature range of interest (i.e., 140 to 300 K) the heating rate varies as specified in Table 1. The heating rate for the exposure variation experiments is nominally 2.3 K/s. For the heating rate variation experiments, discussed in the Metastable State section, the heating rate is deliberately varied between nominal values of 0.02 and 2.3 K/s. For simplicity, we report our results using the average heating rate over the range of interest.

The ethers are purchased from Aldrich. Gas chromatography mass spectroscopy (GCMS), performed in-house with a Finnigan 4000 quadrupole mass spectrometer (electron energy 70 eV), determines the purity of 1,3-dioxane, 1,4-dioxane and 1,3,5-trioxane as 99.3%, 100% and 100%, respectively. The ethers are further purified by a series of freeze-

Table 1. Experimental heating rates in the temperature range of interest

Rate, mV/min	Heating Rate, K/s		
	High	Low	Average
0.1	0.03	0.01	0.02±66%
0.2	0.05	0.03	0.04±36%
1.0	1.2	0.9	1.0±25%
2.0	2.6	1.9	2.3±32%



pump-thaw cycles on the gas handling lines. 1,3-Dioxane and 1,4-dioxane are liquids at room temperature; 1,3,5-trioxane is a solid at room temperature. The vapor above the condensed phase of ether is used as the gas source in these experiments. Sufficient pressures (ca. 10 to 20 Torr) are obtained without heating the solid or liquid samples.

The thermal desorption spectra of the cyclic ethers contain several distinct states. For simplicity, we adopt the following nomenclature for labeling the various desorption states. Minority chemisorption states, having peak areas less than 30% of the total area of all chemisorption states, are denoted  $\beta$ . Majority chemisorption states, which account for at least 30% of the total chemisorption peak area, are labeled  $\alpha$ . For some of these ethers, there exists more than one minority ( $\beta$ ) or majority ( $\alpha$ ) chemisorption state. For this reason, a subscript corresponding to the sequence of population with increasing exposure of the  $\alpha$ - and  $\beta$ -states is included. Multilayer and metastable states are labeled  $\gamma$  and  $\delta$ , respectively.

### III. RESULTS AND DISCUSSION

Thermal desorption spectra for 1,3-dioxane, 1,4-dioxane and 1,3,5-trioxane are shown in Figures 1, 2 and 3, respectively. Low exposures are plotted in Figures 1A, 2A and 3A; higher exposures are shown in Figures 1B, 2B and 3B. In each case, the spectra reported are obtained by monitoring the most abundant molecular fragment. Equivalent spectra are obtained if other, less-abundant molecular fragments are monitored.

The desorption spectra of the three ethers are similar. Each compound, for instance, desorbs in several distinct states. In addition to sharp, low-temperature features, the spectra also exhibit several broader higher-temperature states. Due to the similarities of these spectra, the data are discussed according to the type of desorption state (i.e., minority and majority chemisorption, multilayer or metastable).

#### A. Chemisorption States

Comparison of the thermal desorption spectra in Figures 1, 2 and 3 shows that all the cyclic ethers exhibit several chemisorption states. The peak temperatures, relative populations and desorption energies of the chemisorption peaks are listed in Table 2. The desorption energies are calculated by Redhead's method [18], assuming simple first-order desorption kinetics and a pre-exponential factor of  $10^{13} \text{ s}^{-1}$ .

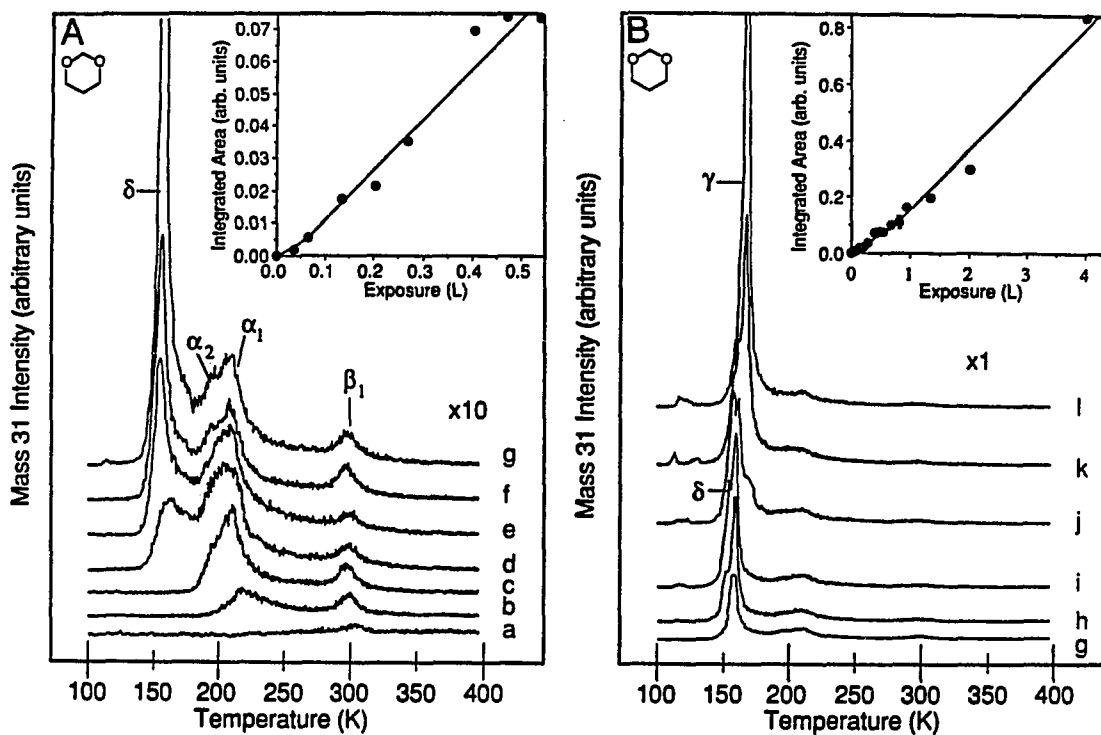


Figure 1. Thermal desorption spectra and uptake curves of 1,3-dioxane  
 (A) Thermal desorption spectra monitoring mass 31 ( $\text{CH}_3\text{O}^+$ ) following an a) 0.07, b) 0.14, c) 0.27, d) 0.41, e) 0.47, f) 0.54 and g) 0.68 L exposure of 1,3-dioxane at 85 K. (B) Thermal desorption spectra monitoring mass 31 ( $\text{CH}_3\text{O}^+$ ) following an g) 0.68, h) 0.81, i) 0.95, j) 1.4, k) 1.7 and l) 2.0 L exposure of 1,3-dioxane at 85 K. The nominal heating rate is 2.3 K/s. Insets show the integrated area of mass 31 as a function of 1,3-dioxane exposure.

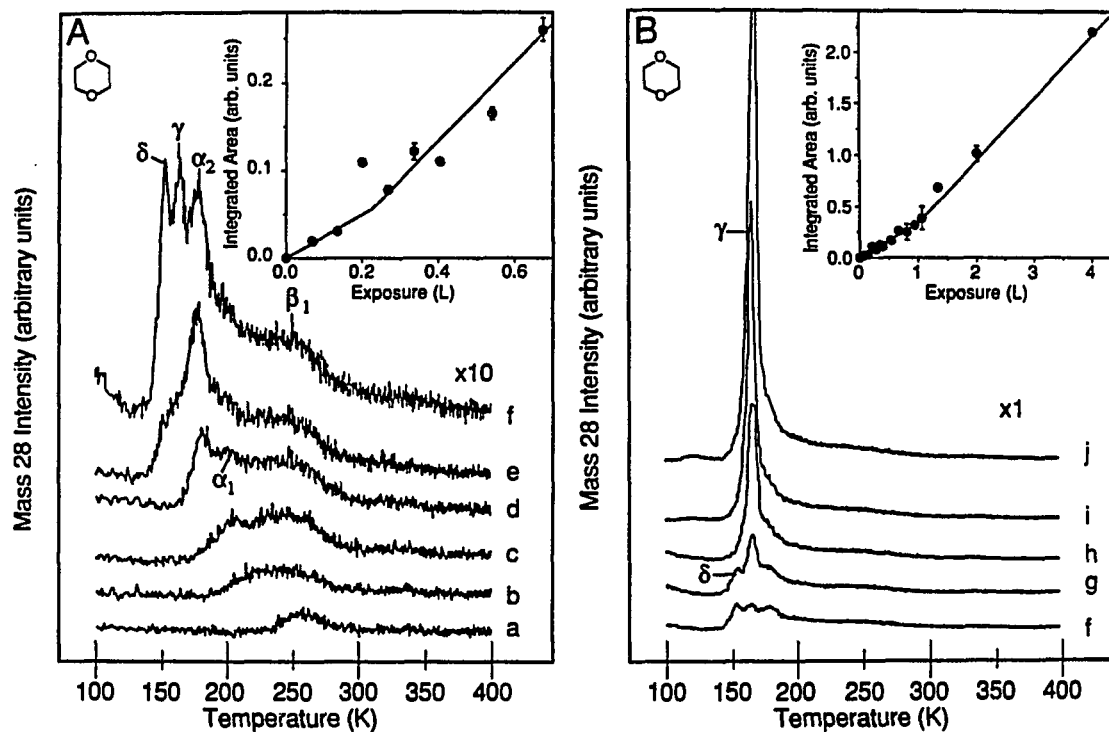


Figure 2. Thermal desorption spectra and uptake curves of 1,4-dioxane (A) Thermal desorption spectra monitoring mass 28 ( $\text{CO}^+$ ) following an a) 0.07, b) 0.20, c) 0.27, d) 0.34, e) 0.54 and f) 0.68 L exposure of 1,4-dioxane at 85 K. (B) Thermal desorption spectra monitoring mass 28 ( $\text{CO}^+$ ) following an f) 0.68, g) 0.81, h) 1.1, i) 1.4 and j) 2.0 L exposure of 1,4-dioxane at 85 K. Equivalent spectra are obtained if mass 31, the less-intense fragment  $\text{CH}_3\text{O}^+$ , is monitored. The nominal heating rate is 2.3 K/s. Insets show the integrated area of mass 28 as a function of 1,4-dioxane exposure.

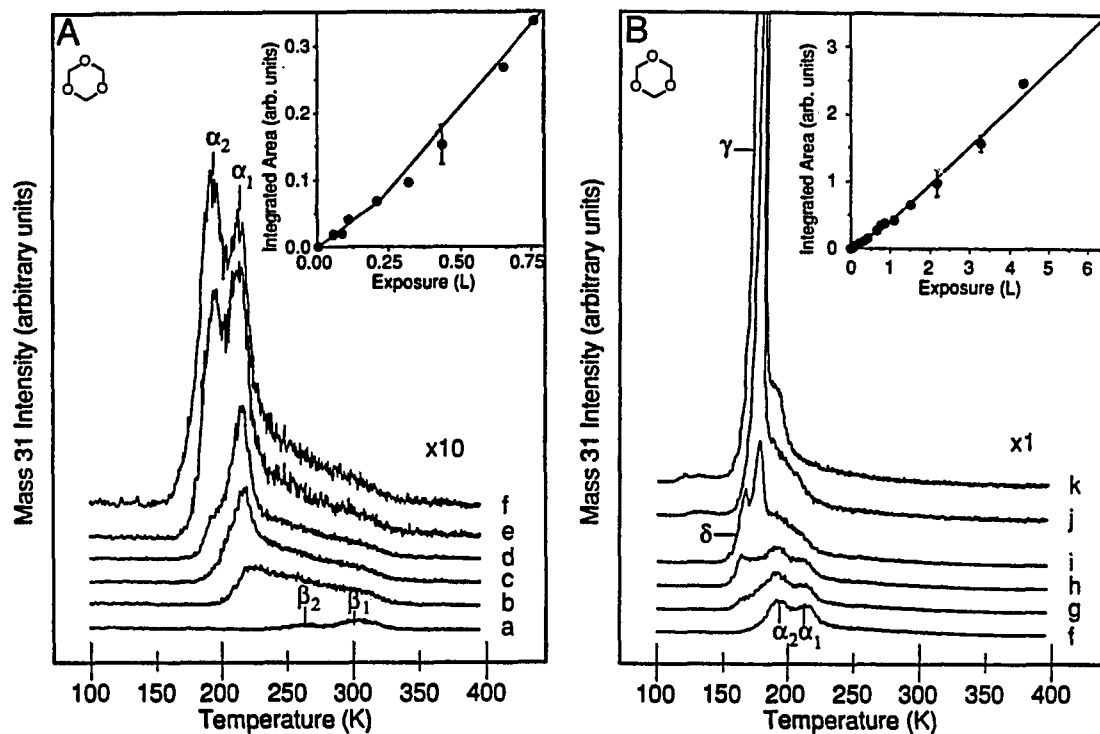


Figure 3. Thermal desorption spectra and uptake curves of 1,3,5-trioxane

(A) Thermal desorption spectra monitoring mass 31 ( $\text{CH}_3\text{O}^+$ ) following an a) 0.05, b) 0.22, c) 0.33, d) 0.44, e) 0.65 and f) 0.76 L exposure of 1,3,5-trioxane at 85 K. (B) Thermal desorption spectra monitoring mass 31 ( $\text{CH}_3\text{O}^+$ ) following an f) 0.76, g) 0.87, h) 1.1, i) 1.5, j) 2.2 and k) 3.3 L exposure of 1,3,5-trioxane at 85 K. The nominal heating rate is 2.3 K/s. Insets show the integrated area of mass 31 as a function of 1,3,5-trioxane exposure.

Table 2. Characteristics of the  $\alpha$ - and  $\beta$ -desorption states of cyclic ethers: peak temperatures, associated desorption energies and relative populations

Compound	$\beta_1$	$\beta_2$	$\alpha_1$	$\alpha_2$	
1,3-Dioxane	298-306	-----	208-216	190-194	Temperature (K)
	78-80	-----	54-56	49-50	Energy (kJ/mol)
	27	-----	38	35	Population (%)
1,4-Dioxane	247-255	-----	200-204	175-181	Temperature (K)
	64-67	-----	51-53	45-46	Energy (kJ/mol)
	18	-----	37	45	Population (%)
1,3,5-Trioxane	297-307	254-267	210-224	190-196	Temperature (K)
	78-81	66-70	54-58	49-50	Energy (kJ/mol)
	5	8	32	55	Population (%)

### A.1. Minority Chemisorption States

All the cyclic ethers desorb in minority chemisorption states ( $\beta$ -states) above ca. 250 K. Molecules which desorb in these states are bonded very strongly to the surface (see Table 2), but the population of these states is low, especially for the 1,3,5-trioxane  $\beta$ -states. A possible explanation for the low population of the  $\beta$ -states is that some of the molecules desorb while the remainder of the molecules decompose.

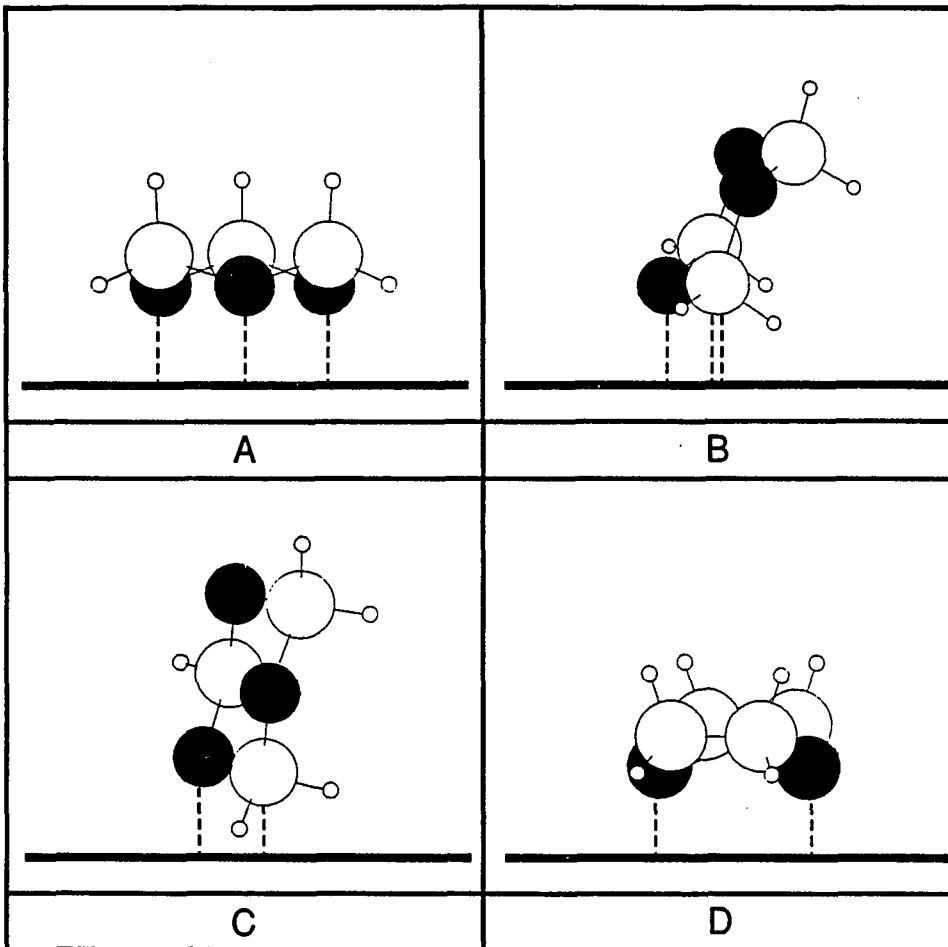
The extent of ether decomposition is measured by monitoring hydrogen and carbon monoxide evolution during the experiment. The method for expressing these values in monolayers of decomposed ether is described in Paper II of this thesis. Based on these data, we estimate less than 0.1 monolayer of ether decomposes. We note, however, that hydrogen and oxygen evolution are nonstoichiometric in the decomposition products. In each case, fewer oxygen atoms are evolved as CO than expected from the amount of hydrogen evolution and molecular stoichiometry. Nevertheless, desorption of other decomposition products is not observed.

To evaluate what fraction of adsorbed ether molecules decompose, we estimate the surface coverage of ethers based on the molecular cross section of cyclohexane,  $34.40 \text{ \AA}^2$  [19]. The molecular cross section is the area of the surface occupied by an adsorbed molecule [19]. This value is not especially sensitive to small changes in bond lengths and we approximate the size of the cyclic ethers with the value for cyclohexane. The ether potentially can adsorb in several different orientations, as

**Figure 4. Possible bonding configurations for adsorbed cyclic ether molecules**

The black circles, the large open circles and the small circles represent oxygen atoms, carbon atoms and hydrogen atoms, respectively. (A) Adsorption in the chair conformation with the oxygen and carbon skeleton parallel with the surface. (B) Adsorption in the chair conformation via one oxygen atom and two methylene groups with the molecular skeleton approximately perpendicular to the surface. (C) Adsorption in the chair conformation via one oxygen atom and one methylene group with the molecular skeleton approximately perpendicular to the surface. The configurations in A, B and C are illustrated using 1,3,5-trioxane, but equivalent structures are possible with 1,3- and 1,4-dioxane. (D) Adsorption of 1,4-dioxane in the boat conformation with the oxygen and carbon skeleton parallel with the surface.





illustrated for 1,3,5-trioxane in Figure 4. First, we will consider the configuration in which the carbon and oxygen skeleton is approximately parallel to the surface (Figure 4A). This configuration is analogous to that observed for cyclohexane [3-5]. In this orientation, an ether molecule excludes an area of the surface equivalent to ca. 5.5 Ru atoms. If we assume perfect and nonsite specific packing, the absolute coverage of ether on Ru(001) is 0.18 monolayer. Thus, the 0.10 monolayer of ether which decomposes corresponds to about half of the maximum coverage of ether in the first layer.

The other possible orientations are those in which the carbon and oxygen skeleton is more perpendicular to the surface. Two possible structures of this type are shown in Figures 4B and C. The areas of the surface excluded by the two orientations are approximately equal. We estimate that the molecular cross section of the upright molecules is 30 Å. The corresponding surface coverage of ether, assuming perfect and nonsite specific packing, is 0.21 monolayer. The relative amount of decomposition is, thus, about 0.50 monolayer for upright ether molecules.

The assumption that molecular packing is independent of the surface site is probably invalid. If site specificity is required, the absolute coverages of ether stated above are too high. Consequently, the relative coverage of ether which decomposes is probably greater than 0.5 monolayer.

Before interpreting the thermal desorption data in terms of bonding configuration we will briefly review what is known about the bonding of

ethers to surfaces. The main component of the ether-surface bond arises from electron donation from oxygen lone pair electrons to the surface. This bond is typically about 40 kJ/mol [7-10]. The ether-surface bond has a secondary component which involves the methylene groups. Each methylene group contributes 5 to 6.5 kJ/mol to the overall bond [3,7,9,20].

The minority  $\beta$ -state molecules bond to the surface very strongly. The bond strengths for the  $\beta_1$ -states of 1,3-dioxane and 1,3,5-trioxane are on the order of 80 kJ/mol. This value is consistent with bonding through two oxygen atoms. The  $\beta_1$ -state of 1,4-dioxane and the  $\beta_2$ -state of 1,3,5-trioxane bond strengths are 65-70 kJ/mol. This bond strength suggests bonding via one oxygen atom and several methylene groups. The  $\beta$ -states represent a small fraction of all the desorbing molecules. It is plausible that so few of the  $\beta$ -state molecules desorb from the surface because a substantial fraction decompose.

#### A.2. Majority Chemisorption States

The majority of the chemisorbed ether molecules desorb in the  $\alpha$ -states. The desorption spectra of each ether show two  $\alpha$ -states. The  $\alpha_1$ -states desorb between 200 and 225 K; the  $\alpha_2$ -states desorb between 175 and 200 K. The desorption temperatures, desorption energies and relative populations of the  $\alpha$ -states are listed in Table 2. For each compound, the  $\alpha_1$ -state is populated at lower exposures than the  $\alpha_2$ -state.

The  $\alpha_1$ -state chemisorption bonds are between 51 and 58 kJ/mol. The magnitude of this interaction is consistent with one oxygen-metal plus two methylene-metal interactions, as discussed above. The configuration postulated for  $\alpha_1$ -molecules is illustrated in Figure 4B.

Molecules in the  $\alpha_2$ -states are chemisorbed about 7 kJ/mol more weakly than the  $\alpha_1$ -molecules. One configuration which is consistent with this value is one oxygen-metal and one methylene-metal interaction. This configuration is illustrated in Figure 4C.

In light of the configurations presented in Figure 4, several questions immediately come to mind. First, do the majority of the adsorbed ether molecules bond primarily through a single oxygen atom, as proposed above, although there are several available in the molecule? The donation of electron density to the surface by the oxygen atom may prohibit the formation of a second (and third, in the case of 1,3,5-trioxane) oxygen-metal bond. Electron donation to the metal from the first oxygen atom may cause a locally high electron density which could prevent the formation of additional oxygen-metal bonds. Electron donation from the first oxygen atom may effectively create nearest-neighbor and next-nearest-neighbor repulsions. This is reasonable since this effect gives rise to ordered structures of oxygen overlayers [21].

Another possibility is that the oxygen-metal bonds are weaker than expected due to the close proximity of the oxygen atoms imposed by molecular structure. Perhaps the ethers bond through several oxygen atoms, but the oxygen-metal interactions are weaker than expected from

studies of monoethers [7-10]. The electron donation argument discussed above can account for weaker than expected oxygen-metal bonds in close proximity.

A second question rising from our proposed configurations is what causes the energy difference between the  $\alpha_1$ - and  $\alpha_2$ -states? At lower exposures, when the  $\alpha_1$ -state is populated, the surface is less crowded and the cyclic ethers perhaps can interact with the substrate without interference with neighboring ether molecules. As exposure increases and population of the  $\alpha_2$ -state begins, the surface contains more adsorbed ether molecules. For either steric or electronic reasons the  $\alpha_2$ -state molecules may not interact as strongly with the surface as the  $\alpha_1$ -molecules.

An electronic effect may result from increased electron density at the surface caused by oxygen lone pair electron donation. If the surface has an excess of electron density from adsorbed molecules, other molecules may bond less strongly. This may explain the weaker bond energy of the  $\alpha_1$ -states. A steric effect may also explain the lower bond strength of the  $\alpha_2$ -state. Adsorbed molecules may spatially block or electronically repel other molecules from adsorbing in a site which allows a strong adsorption bond. As a result, the newly adsorbed molecules may interact with the surface more weakly.

The final question which comes to mind is what molecular configuration is consistent with this bonding scheme? Although the boat conformation is not ruled out by our data, it is likely that these

molecules adsorb in the lower-energy chair configuration. The boat conformation of 1,4-dioxane, however, is particularly plausible because the oxygen atoms are opposite one another in the ring. In the chair configuration analogous to that represented in Figure 4A, only one oxygen atom of 1,4-dioxane approaches the surface. If the molecule adopts the boat conformation, as shown in Figure 4D, both oxygen atoms can interact with the surface. For chair configuration 1,4-dioxane, illustrated for 1,3,5-trioxane in Figure 4A, the structure prohibits bonding via both oxygen atoms.

Other data, such as that which may be obtained from ESDIAD or EELS experiments, are needed to confirm the chair conformation as well as the configurations proposed herein.

#### B. Multilayer States

As shown in Figures 1, 2 and 3, at high exposures the ethers all exhibit insatiable  $\gamma$ -states. The  $\gamma$ -states exhibit typical zero-order desorption kinetics (i.e., peak temperature and full-width-at-half-maximum increase with increased exposure). The  $\gamma$ -peak maximum, for an exposure greater than those when the  $\delta$ -state is observed, occurs at ca. 165, 160 and 175 K for 1,3-dioxane, 1,4-dioxane and 1,3,5-trioxane, respectively. We believe these states represent a condensed multilayer of ether because the  $\gamma$ -peaks do not saturate with increasing exposure. Arrhenius plots of  $\ln(\text{Intensity})$  vs.  $1/T$  for the leading edge of the  $\gamma$ -peaks yield sublimation energies of  $56 \pm 7$ ,  $50 \pm 3$  and  $55 \pm 2$  kJ/mol for

1,3-dioxane, 1,4-dioxane and 1,3,5-trioxane, respectively. The sublimation energy for 1,3,5-trioxane,  $48.5 \pm 2.5$  kJ/mol [22], is in reasonable agreement with our experimentally determined value. Literature values of the sublimation energies are not available for the two diethers. Vaporization energies for 1,3- and 1,4-dioxane are  $35.6 \pm 0.8$  and  $37.5 \pm 0.4$  kJ/mol [22], respectively. Our values for the sublimation energies of these compounds are higher than the literature values of the vaporization energies, as expected from thermodynamic considerations [23].

### C. Metastable States

Another consistent feature in the thermal desorption spectra of the cyclic ethers is a feature at temperatures slightly lower than the  $\gamma$ -state (see Figures 1, 2 and 3). These transient features are only observed for certain ether exposures. The  $\delta$ -states occur at ca. 160, 150 and 165 K for 1,3-dioxane, 1,4-dioxane and 1,3,5-trioxane, respectively. The  $\delta$ -states, although they desorb at lower temperatures than the  $\gamma$ -states, populate at lower exposures. This is unusual: higher temperature states are usually populated before lower temperature states, as exposure increases.

These low-temperature desorption states are evident in the thermal desorption spectra of all the cyclic ethers. In an effort to assess the metastability of these states, we conduct a series of thermal desorption experiments in which the experimental heating rate is varied over the

range of 0.2 to 2.3 K/s. These data are illustrated in Figures 5, 6 and 7 for 1,3-dioxane, 1,4-dioxane and 1,3,5-trioxane, respectively.

Thermal desorption data, obtained using different heating rates for a fixed exposure of 1,3-dioxane, are shown in Figure 5A. For this exposure, the  $\delta$ -state is actually comprised of two closely-spaced peaks. The two features behave in concert as heating rate changes, and we label them  $\delta_1$  and  $\delta_2$ . As heating rate increases, the  $\delta$ -states grow at the expense of the  $\gamma$ -state. This is also seen in Figure 5B, where the change in the normalized peak heights of the desorption features are plotted as a function of heating rate. The  $\delta_2$ -points are offset to the right for clarity. Note the similarity in the  $\delta_1$ - and  $\delta_2$ -state behavior. As heating rate increases the  $\delta_1$ -,  $\delta_2$ - and  $\gamma$ -peak heights change by 70%, 26% and -51% (where an increase in peak height with heating rate is defined as a positive number), respectively.

Thermal desorption data for 1,4-dioxane are illustrated in Figure 6A for various heating rates. For this compound, as heating rate increases the  $\delta$ -state grows at the expense of the  $\gamma$ -state. This is also represented in Figure 6B, where normalized peak intensity is plotted as a function of heating rate. In this graph, the  $\alpha_2$ -state points are offset slightly to the right for clarity. The change in the relative height of the  $\alpha_2$ -state (12%) is insignificant. For comparison, the  $\delta$ - and  $\gamma$ -peak heights increase by 72% and -36%, respectively.

Analogous data are shown in Figure 7A and B for 1,3,5-trioxane. Figure 7A shows the thermal desorption spectra for the different heating



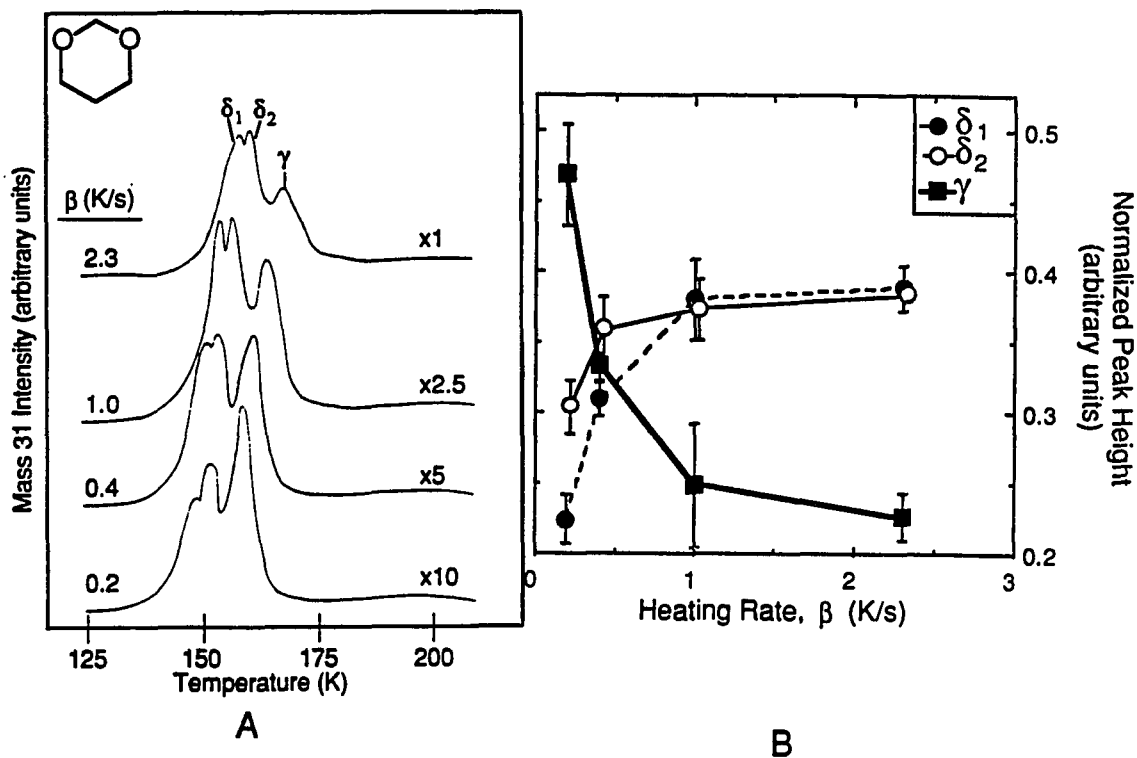


Figure 5. The effect of heating rate on the thermal desorption spectra of 1,3-dioxane

(A) Thermal desorption spectra following an 0.82 L exposure of 1,3-dioxane. Each spectrum is acquired using the indicated heating rate. Note the relative scales for each spectrum. (B) Normalized peak height vs. heating rate for the  $\delta_1$ -,  $\delta_2$ - and  $\gamma$ -states.

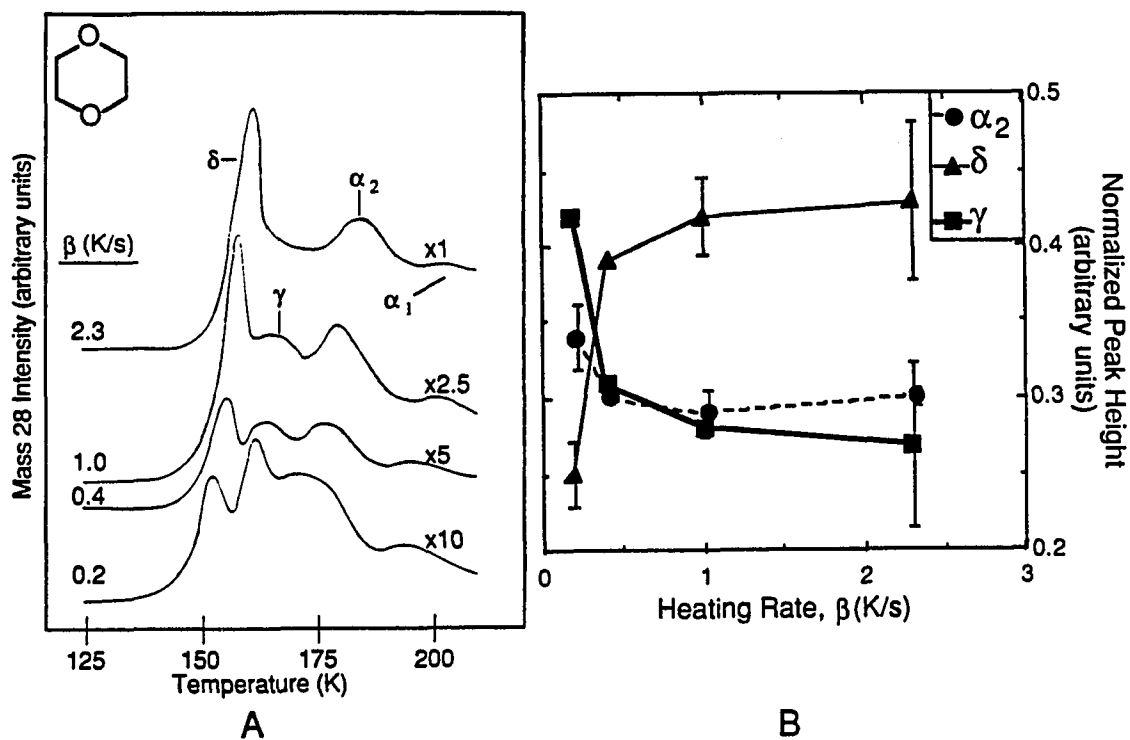


Figure 6. The effect of heating rate on the thermal desorption spectra of 1,4-dioxane

(A) Thermal desorption spectra following an 0.68 L exposure of 1,4-dioxane. Each spectrum is acquired using the indicated heating rate. Note the relative scales for each spectrum. (B) Normalized peak height vs. heating rate for the  $\alpha_2$ -,  $\delta$ - and  $\gamma$ -states.

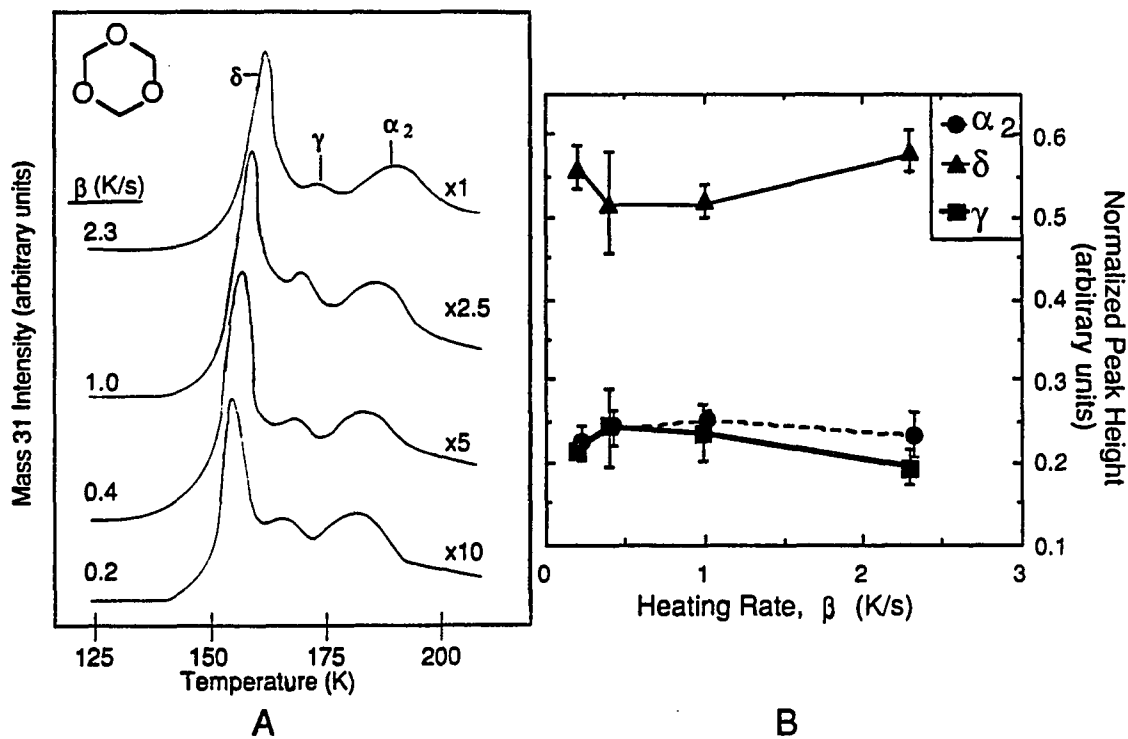


Figure 7. The effect of heating rate on the thermal desorption spectra of 1,3,5-trioxane  
 (A) Thermal desorption spectra following an 1.4 L exposure of 1,3,5-trioxane. Each spectrum is acquired using the indicated heating rate. Note the relative scales for each spectrum. (B) Normalized peak height vs. heating rate for the  $\alpha_2$ -,  $\delta$ - and  $\gamma$ -states.

rates; Figure 7B shows the changes in the normalized peak heights of the  $\alpha_2$ -,  $\delta$ - and  $\gamma$ -states. The data points for the  $\alpha_2$ -state are offset slightly to the right for clarity. The  $\alpha_2$ -,  $\delta$ - and  $\gamma$ -states change by 5%, 2% and -14%, respectively, as heating rate increases. These changes are significantly smaller than those observed for the dioxanes. As a result, the  $\delta$ -state of 1,3,5-trioxane is not metastable over this heating rate range, however the  $\delta$ -label is maintained for simplicity. For 1,3,5-trioxane, thus, no appreciable conversion between the  $\delta$ - and  $\gamma$ -states occurs when the experimental heating rate varies, within this range of heating rates.

The two dioxanes, however, do show distinct evidence of conversion between the  $\delta$ - and  $\gamma$ -states. The conversion of molecules in metastable states to the multilayer states suggest that the  $\delta$ -state molecules are less-stable than the  $\gamma$ -state molecules. It is conceivable that the ether molecules can be kinetically "frozen" in an unstable adsorption state. Slow heating rates allow the trapped molecules to convert to the more stable  $\gamma$ -configuration before desorption. In the simple picture illustrated in Figure 8, there is an energy barrier between the  $\delta$ - and  $\gamma$ -states of the dioxanes. Molecules in the metastable state can convert to the stable state or desorb into the gas phase as molecular energy (temperature) increases. More energy is required to desorb ( $E_d$ ) than to convert ( $E_c$ ) in the case of 1,3- and 1,4-dioxane (i.e.,  $\Delta E > 0$ ). When the sample is heated slowly, the metastable molecules can traverse  $E_c$  before gaining the energy required to move over  $E_d$ . With fast heating

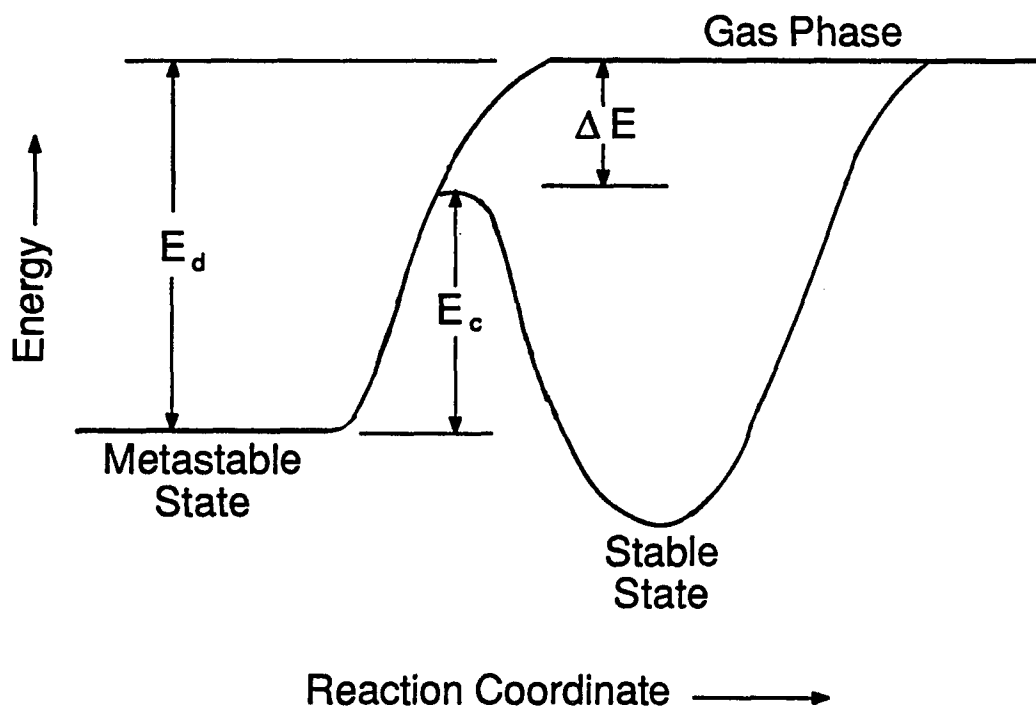


Figure 8. Energy diagram illustrating conversion between the metastable and stable states which can occur during the thermal desorption experiment

Molecules in the metastable state must cross the energy barrier  $E_c$  to convert to the stable state. The energy  $E_d$  is required for the unstable molecule to desorb. For fast heating rates, metastable dioxane molecules desorb directly into the gas phase. If the heating rate is slow, the metastable dioxane molecules can convert to the stable (multilayer) state before desorbing into the gas phase. The energy difference  $\Delta E = E_d - E_c$  is greater than zero for the dioxanes.

rates, the energy of the molecules changes more rapidly and the  $\delta$ -state molecules do not convert to the  $\gamma$ -state before desorption.

In many ways the thermal desorption features of the three cyclic ethers are similar. One exception, however, is that the  $\delta$ -state of 1,3,5-trioxane is not metastable within the experimental range of heating rates. This suggests that the energy barrier to conversion is greater than or equal to the energy barrier for desorption for this compound (see Figure 8).

What could account for this difference for 1,3,5-trioxane? A physical difference is that 1,3,5-trioxane is a solid at room temperature while the dioxanes are liquids. Further, the crystal structure of 1,3,5-trioxane is known [24], but the crystal structures of unsubstituted dioxanes have not been published. Presumably, this is a result of the difficulties encountered in preparing single crystals of the dioxanes. Thus, the metastability of the dioxane molecules may be associated with the relative instability of the solid (crystalline) phases.

A chemical difference in the 1,3,5-trioxane molecules is the presence of three oxygen atoms as compared to the two oxygen atoms in the dioxanes. The crystal structure of 1,3,5-trioxane [24] shows that the chair-configuration molecules are arranged in a three dimensional network. The distances between oxygen and hydrogen atoms in adjacent molecules indicate weak hydrogen bonding. Both hydrogen bonds and high symmetry may account for the inherent stability of the crystalline phase of 1,3,5-trioxane in comparison with the dioxanes.

## V. CONCLUSIONS

The cyclic ethers 1,3-dioxane, 1,4-dioxane and 1,3,5-trioxane adsorb on Ru(001) in several states. Majority chemisorption bond strengths are between 45 and 58 kJ/mol. These energies are consistent with adsorption via one oxygen-metal and one or two methylene-metal bonds or via a number of weak oxygen-metal bonds. The two dioxanes exhibit metastable  $\delta$ -states, in which adsorbed molecules can convert to the multilayer  $\gamma$ -state or desorb, depending on the experimental heating rate. The low-temperature state of 1,3,5-trioxane, on the other hand, does not exhibit metastability, within the experimental range of heating rates.

## VI. ACKNOWLEDGEMENTS

We thank J. L. Davis, T. Hendrixson, D. E. Sanders and W. S. Trahanovsky for valuable discussions. This research is supported by the Director for Energy Research, Office of Basic Energy Sciences. Ames Laboratory is operated for the U.S. Department of Energy by Iowa State University under Contract No. W-7405-ENG-82.



## VII. REFERENCES

1. T. W. G. Solomons, Organic Chemistry (John Wiley and Sons, New York, 1980) 105.
2. W. S. Johnson, J. L. Margrave, V. J. Bauer, M. A. Frisch, L. H. Dreger and W. N. Hubbard, *J. Am. Chem. Soc.*, 82 (1960) 1255.
3. T. E. Madey and J. T. Yates, Jr., *Surface Science*, 76 (1978) 397.
4. F. M. Hoffmann, T. E. Felter, P. A. Thiel and W. H. Weinberg, *Surface Science*, 130 (1983) 173.
5. J. A. Polta, D. K. Flynn and P. A. Thiel, *J. Catalysis*, 99 (1986) 88.
6. A. D. Mitchell and L. C. Cross, Eds., Tables of Interatomic Distances and Configurations in Molecules and Ions (Burlington House, London, 1958).
7. B. A. Sexton and A. E. Hughes, *Surface Science*, 140 (1984) 227.
8. H. Lüth, G. W. Rubloff, W. D. Grobman, *Surface Science*, 63 (1977) 325.
9. K. D. Rendulić and B. A. Sexton, *J. Catalysis*, 78 (1982) 126.
10. P. A. Thiel and T. E. Madey, *Surf. Sci. Reports*, 7 (1987).
11. J. A. Polta, P. J. Schmitz and P. A. Thiel, *Langmuir*, 3 (1987) 1178.
12. J. A. Polta and P. A. Thiel, *J. Am. Chem. Soc.*, 108 (1986) 7560.
13. A. C. Liu and C. M. Friend, *J. Chem. Phys.*, 89 (1988) 4396.
14. P. M. Blass, S. Akhter and J. M. White, *Surface Science*, 191 (1987) 406.
15. H. Herz, H. Conrad and J. Küppers, *J. Phys. E.*, 12 (1979) 369.

16. D. R. Sandstrom and S. P. Winthrow, *J. Vac. Sci. Technol.*, 14 (1977) 748.
17. The 1987 Omega Temperature Measurement Handbook (Omega Engineering, Inc., Stamford, CT, 1987).
18. P. A. Redhead, *Vacuum*, 12 (1962) 203.
19. A. Gavezzotti, M. Simonetta, M. A. Van Hove and G. A. Somorjai, *Surface Science*, 154 (1985) 109.
20. F. M. Hoffmann and T. H. Upton, *J. Phys. Chem.*, 88 (1984) 6209.
21. S.-L. Chang, Ph.D. Thesis, Iowa State University, Ames, Iowa, 1988.
22. J. B. Pedley, R. D. Naylor and S. P. Kirby, Thermochemical Data for Organic Compounds, 2nd edition (Chapman and Hall, Ltd., London, 1986).
23. P. W. Atkins, Physical Chemistry 2nd edition (W.K. Freeman and Co., San Francisco, 1978) 181.
24. V. Buseti, A. Del Pra and M. Mammi, *Acta Crystallogr.*, B25 (1969) 1191.

## CONCLUSIONS

In this dissertation, we investigate the interaction of oxygenated fluorocarbons and hydrocarbons with the Ru(001) surface in an attempt to model the tribological problem of computer disk lubrication. The main conclusions which can be drawn are summarized below:

(a) Adsorbate-metal bonds which occur primarily through oxygen lone pair electron donation to the surface are weakened on fluorination. Fluorinated ethers bond 8-18 kJ/mol less strongly to Ru(001) than analogous hydrogenated ethers in the limit of low exposures;  $\eta^1(O)$ -hexafluoroacetone is bonded 12 kJ/mol less strongly than  $\eta^1(O)$ -acetone. We attribute this bond weakening to inductive withdrawal of electron density at the oxygen by fluorine atoms.

(b) Adsorbate-metal bonds which have a significant backbonding contribution from the metal are strengthened on fluorination.  $\eta^2(C,O)$ -Hexafluoroacetone bonds 20 kJ/mol more strongly to Ru(001) than  $\eta^2(C,O)$ -acetone. We attribute this bond strengthening to the lowering of the acceptor  $\pi^*$  orbital energy levels of the fluorinated molecules which allows more effective backbonding.

(c) Oxygenated fluorocarbons decompose much less than analogous oxygenated hydrocarbons. The fluorinated molecules decompose insignificantly, but 0.04 to 0.17 monolayer of the hydrogenated molecules decompose. The stability of oxygenated fluorocarbons adsorbed at metal surfaces is attributed to the relative strengths of the adsorption bonds,

the higher strength of the C-F bond (relative to the C-H bond) or a difference in bonding geometry for oxygenated hydrocarbons and fluorocarbons.

(d) The fluorinated diether interacts with Ru(001) about as strongly as the fluorinated monoether. This suggests the fluorinated mono- and diether molecules bond to the surface in the same way, presumably through one ether linkage. Hydrogenated diethers, on the other hand, bond up to 35% more strongly to Ru(001) than the hydrogenated monoether. This increase suggests bonding via either two weak oxygen-metal bonds or bonding through one oxygen-metal bond and several methylene groups.

(e) The majority of the cyclic ethers 1,3-dioxane, 1,4-dioxane and 1,3,5-trioxane bond to Ru(001) by a 45 to 58 kJ/mol bond. The magnitude of this interaction suggests bonding by either a number of weak oxygen-metal bonds or through one oxygen metal bond and several methylene groups.

(f) 1,3-Dioxane and 1,4-dioxane exhibit metastable adsorption states which can be converted to the more stable multilayer state if the sample heating rate is slow. 1,3,5-Trioxane, on the other hand, desorbs in a low-temperature state which does not convert to the more stable phase in our range of heating rates. The stability of this 1,3,5-trioxane state is attributed to the molecular symmetry and the weakly hydrogen bonded crystalline structure of the compound.

(g) This fundamental research on the chemisorption of fluorinated ethers suggests that fluorinated mono- and diethers bond to Ru(001) via one oxygen-metal interaction. Thus, in a polymeric fluorinated ether, spacing ether linkages by two  $\text{CF}_2$  groups, as in the diether, may prevent bonding through both oxygen atoms. Perhaps spacing the oxygen atoms further along the chain may allow bonding via both oxygen atoms and, thus, a stronger bond. Furthermore, since the ether-surface bond consists of electron donation of the oxygen lone pair electrons to the metal, a high work function (electropositive) metal is expected to accept more electron density and form a stronger bond. Thus, electropositive metal particles on computer disks may enhance lubricant adhesion.

## REFERENCES

1. T. F. J. Quinn, The Application of Modern Physical Techniques to Tribology (Newnes-Butterworths, London, 1971).
2. E. R. Booser, Ed., CRC Handbook of Lubrication (Theory and Practice of Tribology) Vol. 1 (CRC Press, Inc., Boca Raton, FL, 1983).
3. D. Dowson, History of Tribology (Longman Group Ltd., London, 1979).
4. D. H. Buckley, ASLE Transactions, 13 (1970) 39.
5. D. H. Buckley, Friction, Wear, and Lubrication in Vacuum (National Aeronautics and Space Administration, Washington, D.C., 1971).
6. D. H. Buckley and S. V. Pepper, ASLE Transactions, 15 (1972) 252.
7. S. V. Pepper, J. Appl. Phys., 45 (1974) 2947.
8. D. H. Buckley, ASLE Transactions, 17 (1974) 36.
9. D. H. Buckley, ASLE Transactions, 17 (1974) 206.
10. S. V. Pepper, J. Appl. Phys., 47 (1976) 2579.
11. D. H. Buckley, ASLE Transactions, 21 (1978) 118.
12. K. Miyoshi and D. H. Buckley, ASLE Transactions, 22 (1979) 146.
13. K. Miyoshi and D. H. Buckley, Wear, 66 (1981) 157.
14. K. Miyoshi and D. H. Buckley, Appl. Surface Science, 10 (1982) 357.
15. K. Miyoshi and D. H. Buckley, ASLE Transactions, 26 (1983) 53.
16. G. W. P. Rengstorff, K. Miyoshi and D. H. Buckley, ASLE Transactions, 26 (1983) 509.
17. K. Miyoshi and D. H. Buckley, ASLE Transactions, 27 (1984) 295.
18. Krytox Technical Bulletin L6, Dupont Co., Wilmington, DE.

19. Y. Ohshka, T. Tohzuka and S. Takai, European Patent Application No. 84116003.9, Dakin Industries, Ltd., December 20, 1984.
20. D. Sianesi, R. Fontanelli, U.S. Patent No. 3,665,041, Montefluos, Inc., May 23, 1972.
21. W. R. Jones, Jr., K. J. L. Paciorek, T. I. Ito and R. H. Kratzer, Ind Eng. Chem. Prod. Res. Dev., 22 (1983) 166.
22. W. R. Jones, Jr., K. J. L. Paciorek, D. H. Harris, M. E. Smythe, J. H. Nakahara and R. H. Kratzer, Ind. Eng. Chem. Prod. Res. Dev., 24 (1985) 417.
23. W. R. Jones, Jr., K. J. L. Paciorek, J. H. Nakahara, M. E. Smythe and R. H. Kratzer, Ind. Eng. Chem. Res., 26 (1987) 1930.
24. K. J. L. Paciorek, R. H. Kratzer, J. Kaufman and J. H. Nakahara, J. Appl. Polymer Sci., 24 (1979) 1397.
25. W. R. Jones, Jr. and C. E. Snyder, Jr., ASLE Transactions, 23 (1980) 253.
26. C. E. Snyder, Jr., L. J. Gschwender and C. Tamborski, Lubrication Engineering, 37 (1981) 344.
27. C. E. Snyder, Jr. and R. E. Dolle, Jr., ASLE Transactions, 19 (1976) 171.
28. G. Caporiccio, C. Corti, S. Soldini and G. Carniselli, Ind. Eng. Chem. Prod. Res. Dev., 21 (1982) 515.
29. C. E. Snyder, Jr., C. Tamborski, H. Gopal and C. A. Svisco, Lubrication Engineering, 35 (1979) 451.

30. D. Sianesi, V. Zamboni, R. Fontanelli and M. Binaghi, *Wear*, 18 (1971) 85.
31. H. Lüth, G. W. Rubloff and W. D. Grobman, *Surface Science*, 63 (1977) 325.
32. B. A. Sexton and A. E. Hughes, *Surface Science*, 140 (1984) 227.
33. K. D. Rendulić and B. A. Sexton, *J. Catalysis*, 78 (1982) 126.
34. A. B. Anton, N. R. Avery, B. H. Toby and W. H. Weinberg, *J. Am. Chem. Soc.*, 108 (1986) 684.
35. M. A. Henderson, P. L. Radloff, J. M. White and C. A. Mims, *J. Phys. Chem.*, 92 (1988) 4111.
36. M. A. Henderson, P. L. Radloff, C. M. Greenlief, J. M. White and C. A. Mims, *J. Phys. Chem.*, 92 (1988) 4120.
37. A. B. Anton, J. E. Parmenter and W. H. Weinberg, *J. Am. Chem. Soc.*, 108 (1986) 1823.
38. N. R. Avery, *Langmuir*, 1 (1985) 162.
39. L. Ng, J. G. Chen, P. Basu and J. T. Yates, Jr., *Langmuir*, 3 (1987) 1161.
40. J. Hrbek, R. A. dePaola and F. M. Hoffmann, *J. Chem. Phys.*, 81 (1984) 2818.



APPENDIX A:

A COMPUTER PROGRAM FOR THERMAL DESORPTION EXPERIMENTS

## I. INTRODUCTION

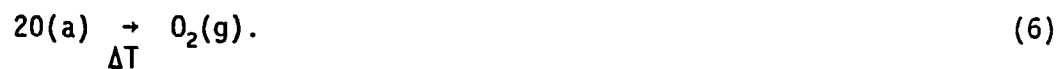
Thermal desorption spectroscopy (TDS) is a widely used surface science technique. During a TDS experiment the gas phase of a vacuum chamber is sampled with a mass spectrometer while an adsorbate-covered sample is heated. As the sample temperature increases, the adsorbate may desorb, decompose, or decompose and later recombine and desorb. For example, adsorbed water,  $H_2O(a)$ , may desorb,



decompose in one of two ways,



or recombine and desorb [1]



The thermal desorption spectrum is a measure of the partial pressure of a gas with a particular mass as a function of sample temperature, or as a function of time. A typical thermal desorption spectrum is shown, for instance, in Figure 2 on page 23 of the thesis. Computer interfacing of

the thermal desorption experiment allows "simultaneous" acquisition of spectra of several gas-phase species with different masses. In this way a complex reaction can be easily followed in one experiment instead of repeating the experiment to monitor each possible reaction product. For example, in the thermal desorption of water, described above, decomposition may occur which yields  $H_2$  and  $O_2$  on heating [1]. With a computer interfaced mass spectrometer, an experiment need only be done once to monitor the three possible desorption products:  $H_2O$ ,  $H_2$  and  $O_2$ .

A second advantage of a computerized data acquisition system is that data can be stored for future reference. Data simply plotted on a piece of paper could be lost or damaged and the experiment would have to be repeated. With a computer interfaced experiment, data files are stored on computer disks. The experimental data can be loaded from disk if plotted output is destroyed.

A third advantage derives from the fact that the area under a TDS peak is proportional to the number of desorbing molecules. Therefore, it is often useful to determine the peak area. Instead of using manual techniques, such as cutting and weighing a piece of paper the same size as the peak area, a computer can mathematically calculate the area under a peak. This saves time.

This appendix describes a TDS computer program which runs on a PDP-11/23 computer.

## II. EQUIPMENT

The PDP-11/23 is interfaced to a UTI-100C quadrupole mass spectrometer and a temperature controller [2] via D/A and A/D converters on ADAC 1030 and 1412 boards. The 1030 board has eight A/D channels and 2 D/A channels while the 1412 board had 4 D/A channels. The computer also controls a Houston Instruments 8 pen plotter and a Data South dot matrix printer. Figure 1 schematically illustrates the interface.

### A. Mass Spectrometer

Quadrupole mass spectrometers contain three components: the ionizer, the filter, and the multiplier, as shown in Figure 2. In the ionizer, electrons are ejected from a hot filament. The electrons travel around the ionizer region under the influence of a 70 eV electrostatic potential applied to a cylindrical grid around the filament (repeller grid in Figure 2). The electrons lose energy by colliding with and ionizing gas molecules. Electrons typically undergo several collisions before losing all their energy or striking the grid. Positive ions, created when the electron collides with a gas molecule, are accelerated away from the positively charged grid toward the negatively charged focusing plate into the filtering region (see Figure 2).

The voltages applied to four rods (hence, quadrupole) in the filtering region (see Figure 2) determine the mass-to-charge ratio of particles (ions) which pass through the filter. Two voltages are applied

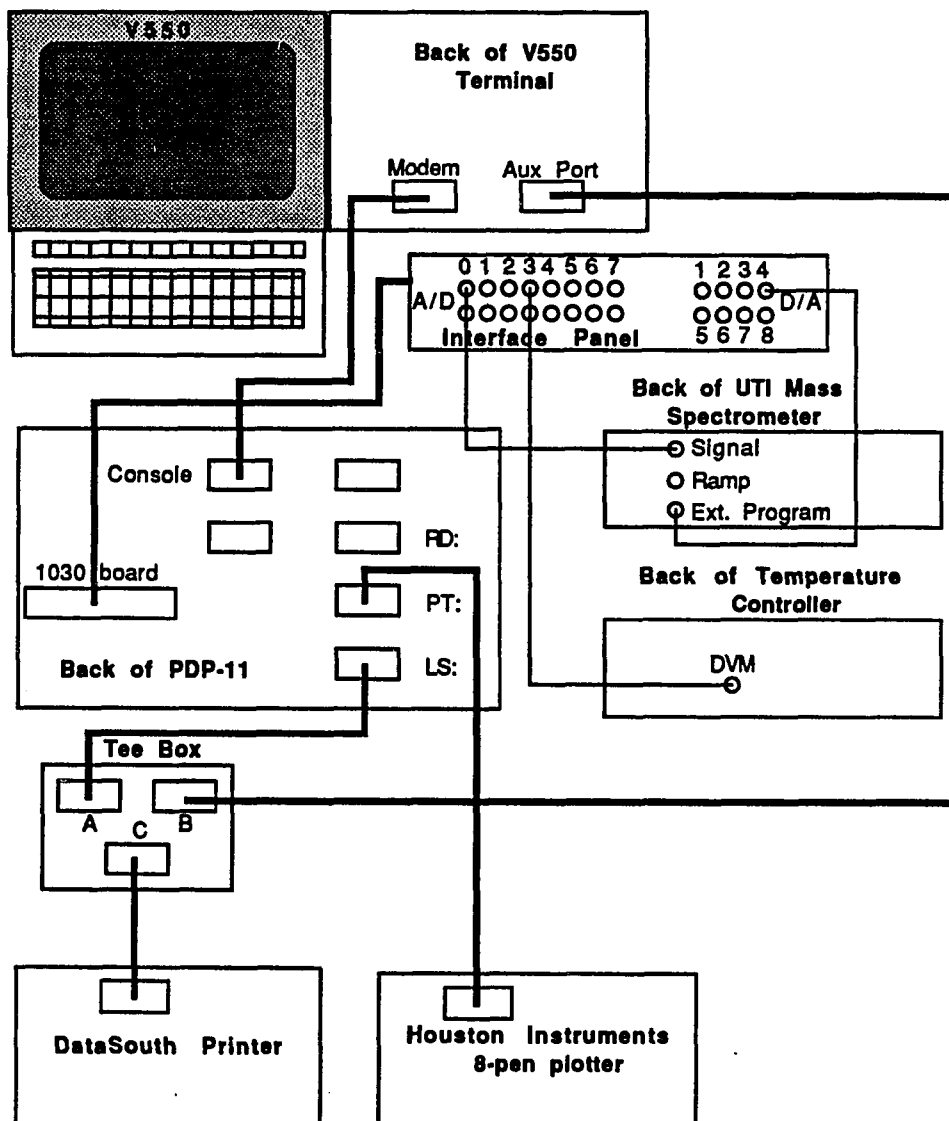


Figure 1. Schematic diagram of the PDP-11/23 computer interface and peripheral equipment  
 Heavy black lines represent 25 pin ribbon cables; narrow lines represent coaxial cables.

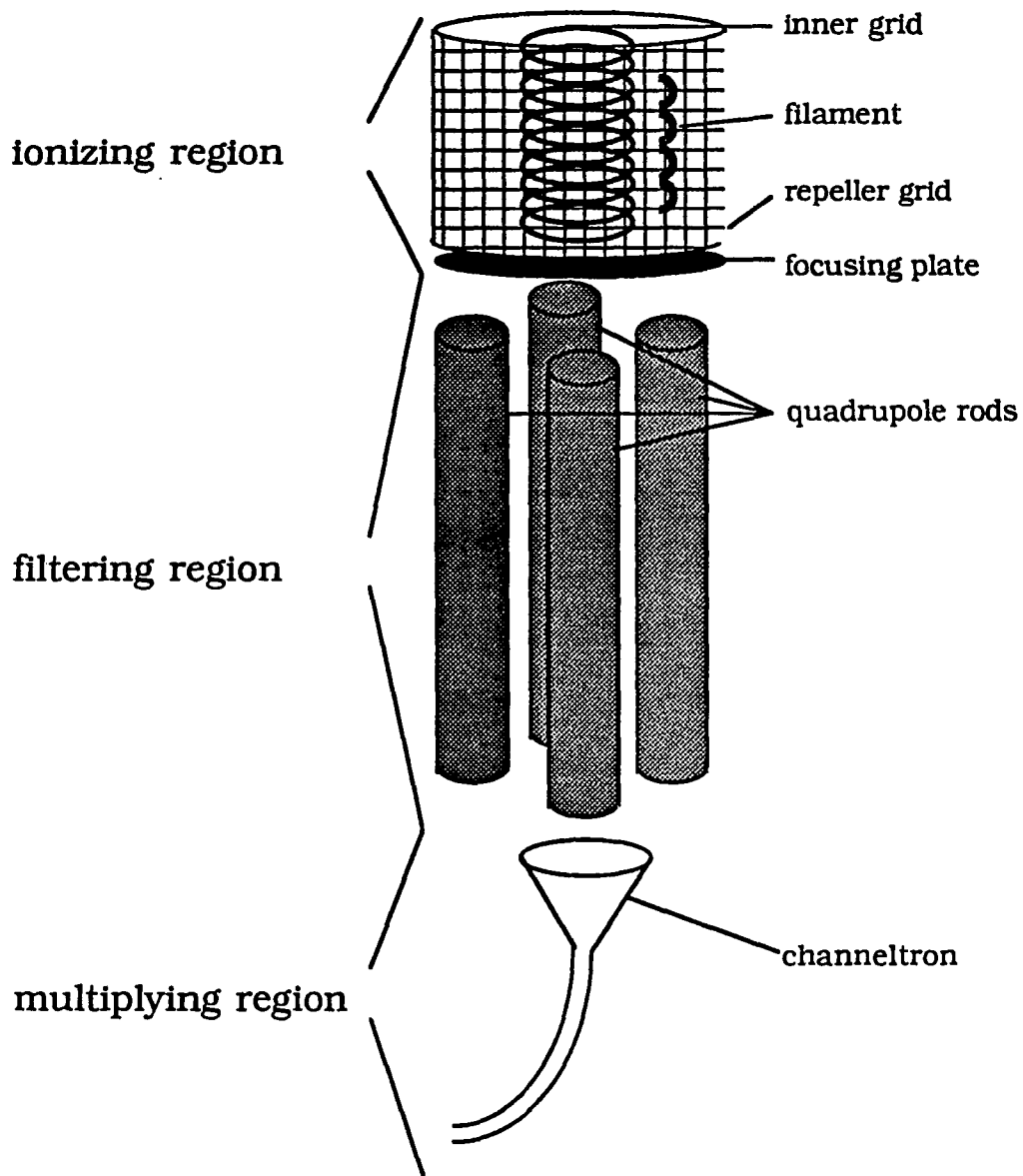


Figure 2. Schematic drawing of a quadrupole mass spectrometer  
Ions created in the ionizing region are focused into the filtering region. Only ions with the specified mass-to-charge ratio will successfully traverse through the filtering region and enter the multiplying region.

to the rods: a DC and a RF voltage. A positive DC voltage is applied to one pair of rods; a negative DC voltage is applied to the other pair of rods. In addition, the RF voltage is applied to both sets of rods. The ratio of DC voltage and RF amplitude is fixed for a given spectrometer. The ions spiral about the rods' central axis and only ions with the appropriate mass-to-charge ratio traverse the entire length of the rods.

Once an ion has successfully traveled through the filtering section, it collides with the entrance of the electron multiplier. Two distinct types of electron multipliers are commonly available: continuous and discrete dynode multipliers. Channel electron multipliers, also known as channeltrons, are continuous dynode devices made of lead-doped glass. Discrete dynode multipliers are made of copper-beryllium. Both materials have a high secondary electron emission ratio ( $r$ ). The secondary electron emission ratio is the number of ejected electrons per incident electron (or ion). The value of  $r$  depends on the multiplier material, but generally between 2 and 10 electrons are ejected per incident particle.

The ion striking the electron multiplier causes ejection of several secondary electrons which, in turn, strike another area of the multiplier ejecting more electrons. This process is known as electron cascading. Each ion striking the front of the multiplier results in  $10^6$  to  $10^8$  electrons exiting at the back of the multiplier after about 10 nanoseconds. As shown in Figure 2, the shape of a channeltron necessarily causes the electron cascade to continue. With a discrete

dynode multiplier, dynode position affects the electron cascade. In this way, the signal is converted to a measurable current by the multiplier. This signal current is further amplified and measured externally by a picoammeter. The measured signal is displayed on the front panel of the UTI-100C and is converted into a voltage. The 0-10 V analog output, labeled "signal out", is available for use with recording devices such as an oscilloscope, and XY recorder or a computer interface.

The higher the partial pressure of the selected mass in the vacuum chamber, the more ions with the selected mass are created in the ionizing region. Therefore, the signal current will be higher for the mass with the higher partial pressure. The voltage output by the spectrometer electronics is proportional to the partial pressure of the selected mass in the vacuum chamber. The partial pressure detection limit is about  $10^{-14}$  Torr.

#### B. Mass Control

D/A channel 1 on the 1412 interface board (labeled "4" on the interface panel shown in Figure 1) controls which mass is selectively filtered by the quadrupole. It is set up to put out 0-10 Volts to the connector labeled "external program" on the back of the UTI controller (see Figure 1). This voltage is internally scaled by the mass spectrometer electronics and applied to the rods, as described above.

Mass can be represented in several ways: atomic mass units, voltage (0-10 V) proportional to the voltage applied to the quadrupole mass



spectrometer, or DAC output (which can be represented in octal, hex, decimal or binary). The PDP-11/23 computer uses the decimal DAC output form to send the selected voltage to the mass spectrometer controller. Within the mass spectrometer electronics this voltage is scaled and the appropriate RF amplitude is generated. An external program "SCAN" is used to determine the relationship between DAC output and mass for a particular spectrometer.

The SCAN program typically is used to measure a mass spectrum of background gas in the vacuum chamber and write the DAC output and corresponding intensity to a data file. Using the PDP-11/23 "TYPE" command (e.g., TYPE FILE.FOR) the operator determines the DAC output corresponding to particular masses. Next, the operator determines the linear relationship between DAC output and mass and modifies the subroutine PEAKS. I usually use a pocket calculator with linear regression to determine the equation of the line. Since the DAC output corresponding to mass 2 does not fit the linear regression determined by the higher mass values for this particular mass spectrometer, a separate DAC value calculation is used when monitoring mass 2. The equation is found just before line 100 in PEAKS; the mass 2 DAC value is found in line 100 in PEAKS. The subroutine PEAKS is described below in the Run section.

### C. Mass Intensity and Temperature

All eight A/D channels on the 1030 interface board are read differentially. The high signal component is connected to the top BNC connector; the low signal component is connected to the bottom BNC connector. The A/D channels are set up to accept values between -10 and +10 Volts. The computer reads mass intensity with A/D channel 0 from the connector labeled "signal" on the back of the UTI controller (see Figure 1).

An independent temperature controller controls the sample heating rate [2] (see Figure 1). The computer reads temperature with A/D channel 3 from the connector labeled "DVM" on the rear of the temperature controller. The thermocouple output from "DVM" is amplified 100 times in the temperature controller.

### III. THE PDP-11/23 TDS PROGRAM

#### A. Program Overview

The PDP-11/23 TDS program is written in Fortran and uses subroutines extensively. There are two categories of subroutines in the program: minor and major subroutines. Minor subroutines are short and contained within the program TDSSUB. Some of these subroutines convert the thermocouple reading, in mV, to temperature, in Kelvin, (ITOK) or change various parts of the menu display (AMUP, COP, CHARTP, RISEP, OFFP, SMPLSP, etc.). Table 1 lists the subroutines in this program, along with a brief description of each subroutines purpose. Major subroutines are, in general, longer and exist in external programs. Some of these subroutines are used to collect data (PEAKS), read or store data on disks (INOUT), and plot data on the Houston Instruments plotter (HIPLT). The remainder of this section is devoted to describing the program.

#### B. Menu

When the operator runs TDSR, the main program, the computer displays an initial checklist of things required to take data, as shown in Figure 3. The initial checklist text is defined on line 9000 of the program. After the list is displayed, the message "ENTER ANY KEY TO CONTINUE" is written and the operator must type a character and press "Return" to continue. Throughout this program entries are typed and the "Return" is

Table 1. TDS program subroutines

---

Subroutine	Purpose
ABSCSR	Moves cursor to specified screen position
AMUP	Displays amu values
AREADM	Reads interface
CHARTP	Displays chart size value
COP	Displays comments
DATEP	Displays date
ERASE	Clears video screen
FNAMEP	Displays file name
FTEMP	Displays final temperature
HIPLT	Plots data on 8-pen plotter
ITEMPP	Displays initial temperature
ITOK	Converts thermocouple output (mV*100) to temperature (K)
KTOMV	Converts temperature (K) to thermocouple output (mV*100)
LOAD	Loads data file
MONPLT	Plots data on monitor
NMASSP	Displays number of masses
OFFP	Displays Y-offset
OPRARP	Displays operator
PEAKS	Data acquisition
PICOP	Displays picoammeter setting
RISEP	Displays rise time
SCROL	Defines scrolling region
SHOW	Updates menu
SLOPEP	Displays heating rate slope
SMPLSP	Displays number of samples
SPRINT	Prints data file
STORE	Stores data file
VIDATR	Sets video attributes
YSCP	Displays Y-scale

---

**\*\*\*\*\*INITIAL CHECKLIST\*\*\*\*\*****TURN ON UTI 100C MASS SPECTROMETER****SET EMISSION CURRENT TO 2 mA****SET ELECTROMETER TO APPROPRIATE RANGE****SET PROGRAMMING MODE TO EXTERNAL****TURN ON TEMPERATURE CONTROLLER****MASS SELECTION IS CONTROLLED BY D/A LABELED 4****MASS SPEC SIGNAL IS INPUT TO COMPUTER BY A/D LABELED 0****TEMPERATURE SIGNAL IS INPUT TO COMPUTER BY A/D LABELED 3****ENTER ANY KEY TO CONTINUE**

Figure 3. Thermal desorption program initial checklist

This information is displayed on the computer screen when the TDS program is run.

pressed. In the remainder of this appendix the use of the Return key will not be explicitly stated.

After a character is typed the computer displays the menu with the default parameters, shown in Figure 4. The default parameters are formatted in lines 25 and 1000-1003 of TDSR. Once the menu is written to the screen, the prompt "TYPE THE FIRST TWO LETTERS OF REQUESTED OPTION (CR)" appears at the bottom of the screen in a 3-line scrolling region. The letters CR refer to the implied carriage Return. All the prompts are displayed in this region of the screen.

To change a parameter, the user must type the first two letters. The computer then displays a prompt for that item and the operator enters the new value. The computer writes the new value to the screen and displays the prompt "TYPE THE FIRST TWO LETTERS OF REQUESTED OPTION (CR)". For example, to change the filename the operator types FI, and the computer prompts "ENTER FILENAME". The operator types the new filename, and the computer writes the new filename to the screen in the appropriate place. This sequence occurs starting at line 31 in TDSR. The subroutine FNAMEP in TDSSUB is called to write the new name to the screen.

The DATE, OPERATOR, VOLTS/AMP, SLOPE, RISE, SAMPLINGS, INITIAL and END TEMPERATURE, NUMBER OF MASSES, CHART SIZE, Mass Values 1-8, Y-SCALE, OFFSET and COMMENTS parameters all are changed in the same way as FILENAME, described above. Table 2 lists the location of each of these parameters in the TDSR program as well as the subroutine called from

<p style="text-align: center;"><b>PHI:TDS-DEC</b> by <b>JAP/MJSJ/MMW</b></p>
--

<b>FILENAME: LD1:DECTDS.000</b>		
<b>DATE: MM/DD/YY</b>		
<b>OPERATOR: MWALCZAK</b>	<u>MASS#</u>	<u>AMU</u>
<b>VOLTS/AMP: 6</b>	1	0
<b>SLOPE: 6</b>	2	0
<b>INITIAL TEMP: 298</b>	3	0
<b>END TEMP: 600</b>	4	0
<b>NUM. OF MASSES: 2</b>	5	0
<b>RISE TIME: 1</b>	6	0
<b>SAMPLINGS: 20</b>	7	0
<b>CHART SIZE: SMALL</b>	8	0
<b>OFFSET Y: 0</b>		
<b>Y-SCALE: 1.00</b>		
<b>COMMENTS:</b>		

**AREA EXIT LOAD K-PLOT T-PLOT PRINT**  
**QUIT RUN STORE UPDATE**

**TYPE THE FIRST TWO LETTERS OF REQUESTED OPTION (CR)**

Figure 4. Thermal desorption program main menu

The main menu displays important information about the data file, such as filename, date and which masses are monitored.

Table 2. PDP-11 parameter locations in TDSR and related subroutines from TDSSUB

Parameter	TDSR Line No.	Subroutine in TDSSUB
FILENAME	31	FNAMEP
DATE	32	DATEP
OPERATOR	35	OPRARP
VOLTS/AMP	36	PICOP
SLOPE	38	SLOPEP
INITIAL TEMP	40	ITEMPP
END TEMP	42	FTEMP
NUMBER OF MASSES	44	NMASSP
CHART SIZE	48	CHARTP
1-8	51-85	AMUP
Y-SCALE	510	YSCP
OFFSET	600	OFFP
RISE	630	RISEP
SAMPLINGS	650	SMPLSP
COMMENTS	700	COP



TDSSUB to write the new values to the menu. Several of the parameter functions are briefly discussed below.

VOLTS/AMP refers to the UTI electrometer gain. If the gain is set to  $10^{-8}$  A, input "8". This is not important within the program, but the value is used to calculate intensity scales plotted on the plotter and in integrating peak areas. To accurately compare experiments the correct gain should be used. Note that the computer does not control the electrometer gain setting. Internally, the interface board amplifies the incoming signal by a factor of 10, 5, 2 or 1 before digitizing the analog signal. Thus, an order of magnitude of computer controlled gain is available. Switching gain in this way is controlled in the subroutine PEAKS, as described below in the Run section.

SLOPE refers to the heating rate setting on the temperature controller. Again, the program is not dependent on this value, but the program uses this variable to determine both RISE and SAMPLINGS in the lines following 25 and 39 in TDSR. RISE is related to the delay before reading intensity. For slower heating rates the program can delay between data points to allow A/D settling. This becomes important when the computer reads masses with different conversion gains. SAMPLINGS refers to the number of voltages read and averaged per data point.

The INITIAL TEMPERATURE is automatically calculated and displayed by the computer at the end of an experiment. The operator need not enter this temperature. The END TEMPERATURE, however, is crucial to the

experiment. Data acquisition terminates when the end temperature is equal to the sample temperature.

The NUMBER OF MASSES must be entered correctly because the intensity collection loop depends on this value. If the number of masses is listed as 2, the computer collects intensity data for the first two masses only, even if more masses are listed in the menu.

CHART SIZE refers to the chart dimensions plotted on the 8 pen plotter. Small charts measure  $8\frac{1}{2}$  x 11 inches; large charts measure 11 x 17 inches.

The Y-SCALE and OFFSET refer to the scale and position of the plotted curves. A Y-SCALE value of 2 doubles the size of the curve. An OFFSET of 1000 raises the curve by one inch (units are 1/1000 of an inch).

Four COMMENT lines are available for free text description of the experiment. For example, the operator can identify the adsorbate, substrate, exposure and any special conditions for the experiment.

At the bottom of the menu several options are listed including AREA, EXIT, LOAD, K-PLOT, T-PLOT, PRINT, QUIT, RUN STORE and UPDATE (see Figure 4). The remainder of this section describes these functions. Table 3 lists the location of the functions in TDSR and the major subroutines involved in function execution.

Table 3. PDP-11 Options from the bottom of the menu and corresponding line numbers in TDSR and major subroutines called

Option	TDSR Line No.	Subroutines called
AREA	530	None
EXIT	990	None
LOAD	400	LOAD (INOUT)
K-PLOT	100	MONPLT HIPLT
T-PLOT	520	MONPLT HIPLT
PRINT	200	SPRINT
QUIT	750	None
RUN	90	PEAKS
STORE	300	STORE (INOUT)
UPDATE	500	SHOW (TDSR)

## C. AREA

The AREA routine displays intensity vs. temperature data on the monitor and calculates the area under the curve specified by the operator. Note that integration takes place with respect to time, although thermal desorption data is usually displayed as a function of temperature. After typing "AR" the operator is asked to "ENTER PEAK #". The computer then prompts "CLEAR GRAPHICS (1/0)". Typing "1" clears the graphics screen; typing "0" leaves the existing images on the screen. The computer displays the curve and crosshairs on the screen. The operator moves the crosshairs using the keypad arrows. The computer also displays a small menu containing the options: (I) INITIAL POINT, (F) FINAL POINT, (E) ERASE PREVIOUS POINT, (A) COMPUTE AREA and (X) EXIT. Pressing X exits the integration routine and rewrites the menu.

To find the area under a peak the operator moves the crosshairs to the point to start integration and presses "I". The operator then moves the crosshairs to the final point for integration and presses "F". Note in this routine the Return key is not needed. If the indicated point is incorrect, pressing "E" will erase the previously marked point and allow repositioning. Once the integration endpoints are marked, pressing "A" computes the area under the peak as described below. When the area is calculated, the computer re-writes the menu, displaying the computed area.

The integration routine is described below for data plotted in Figure 5. The integration begins with the computer averaging the five

intensities centered around the initial and final integration points. Next, the computer calculates a straight baseline between the averaged initial and final points. The averaged baseline is illustrated in Figure 5. Next, the baseline intensity is calculated for the first two data points. The computer subtracts the baseline intensity from the measured intensity for the first two data points. The area of the first rectangle in Figure 5 is found by averaging the adjacent intensities and multiplying by the time interval between the first two points. This sequence is continued for every pair of data points between the initial and final points. The area under the peak is thus the sum of the average intensities of each pair of adjacent points multiplied by the time interval between the points. After the entire interval between end points is integrated, the computer scales the area to the proper units in the lines following 905 in TDSR and displays one number for the resultant area, in microamps\*sec, on the screen.

This integration technique is illustrated in Figure 5. The area calculated is the total area of all the rectangles. For this example, the peak area is 66.16 microacmps\*sec.

#### D. EXIT and QUIT

The EXIT and QUIT options are two ways to stop the TDS program. The exit option saves all the parameters in the menu in the file

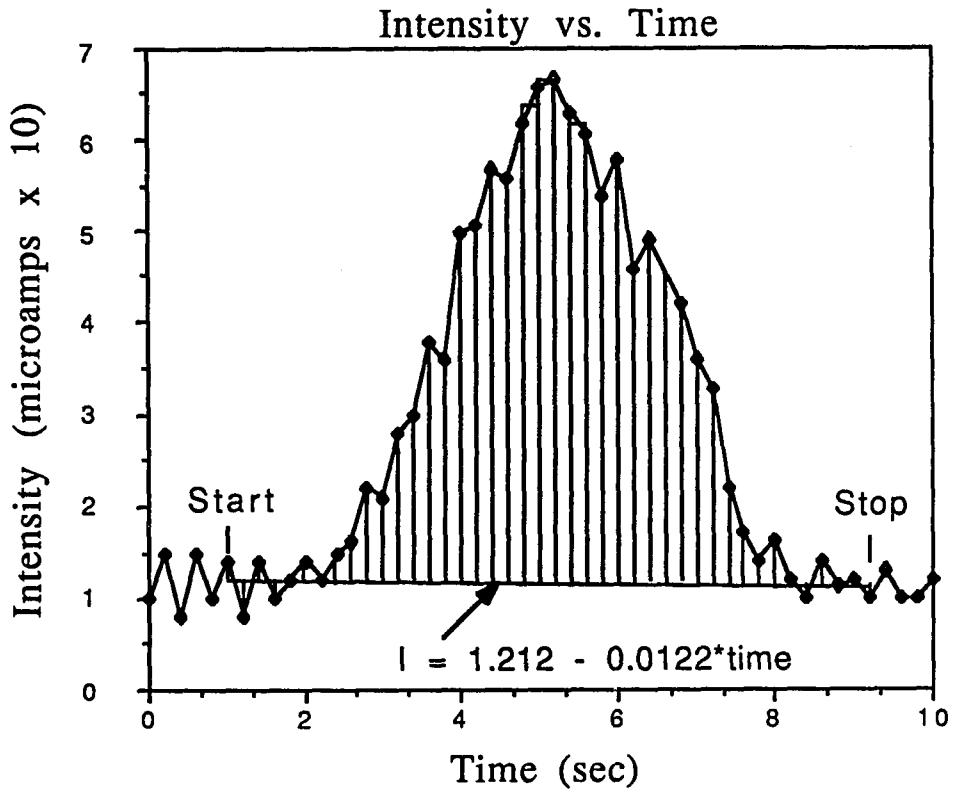


Figure 5. Sample integration

Integration of the area under a TDS curve involves multiplying the average intensity of two adjacent points (corrected for background subtraction) by the time interval between them and summing over the specified integration range.

LD1:FILTMP.DAT on exiting the program. An exit flag is set in the file LD1:EXIT.000. The exit flag is read on program re-entry. If the exit flag is set, the initial checklist is bypassed and the screen is updated with the parameters stored in the file LD1:FILTMP.DAT.

Selecting QUIT exits the TDS program without saving the current parameters. Upon program re-entry the computer displays the initial checklist and the menu containing the default parameters.

#### E. LOAD and STORE

The LOAD and STORE options allow data retrieval and storage on disks. When LOAD is selected the computer calls the subroutine LOAD, in the file named INOUT. The computer prompts "YOUR DATA IS ROUTED BY YOUR FILENAME--OK? (1/0)". If the filename listed in the menu is the desired datafile, the operator types "1". If the filename is incorrect, the operator types "0". If the filename is correct and the operator enters "1" the computer prompts "IS THE TEMPORARY DATA EXPENDABLE (1/0)?" If the data stored in memory are not longer necessary the operator types "1" and the new data are read.

The subroutine STORE in the file named INOUT is called when Store is selected. The computer prompts "YOUR DATA IS ROUTED BY YOUR FILENAME--OK? (1/0)", and the operator responds appropriately. If the operator replies "1" the computer opens the file on the disk. If this file name already exists the computer prompts "THIS FILE ALREADY EXISTS--OVERWRITE (1/0)". If the file exists the operator can either overwrite it (1) or

abort the Store sequence (0) and return to the menu. If the file did not already exist or if the existing file is overwritten, the computer prompts "YOU HAVE THREE OPTIONS 1=REGULAR, 2=T-I, 3=t-T". In this way all the parameters as well as time, temperature and intensity data (1), temperature and intensity data only (2) or time and temperature data only (3) can be stored. Once the data are stored the program returns to the menu.

#### F. K-PLOT and T-PLOT

K-PLOT and T-PLOT allow plotting intensity vs. temperature or time, respectively, on the monitor or the 8 pen plotter. The computer prompts "ENTER PEAK #" and the operator types the mass desired, 1-8. The computer then prompts "AUTO SCALING (1/0)?". Auto scaling plots the entire temperature (time) range. If the operator answers "0" the computer asks "ENTER LOWER TEMPERATURE (TIME), HIGHER TEMPERATURE (TIME)". After the operator enters the temperature (in Kelvin) or the time (in seconds) range, the computer asks "OUTPUT TO MONITOR(=0) OR PLOTTER(=1) (QUIT=2)". The operator enters 0 to plot on the monitor, 1 to plot on the 8 pen plotter and 2 to quit the plotting routine.

If the monitor (0) is selected, the subroutine MONPLT is called and the operator is asked "CLEAR GRAPHICS (1/0)". Clearing the graphics screen erases the existing graphs. When the plot is finished the computer asks "DO YOU WANT A HARD COPY (1=YES)". If the operator requests a hard copy the computer begins the 8 pen plotter sequence,



described below. If the operator does not request a hard copy the program returns to the menu.

If the 8 pen plotter (1) is selected, the subroutine HIPLT is called. The computer prompts "DO YOU WANT A NEW PLOTTER FRAME (1/0)". Answering yes (1) advances roll paper in the plotter, if used. The computer then prompts "DO YOU WANT LABELS (Y=1)?". Labels include axis labels, temperature (time) axis markers, as well as filename, date, and slope. Finally, the computer prompts "ENTER PEN#". Once the pen number is entered the curve is drawn on the plotter. After the plot is finished the computer returns to the menu.

#### G. PRINT

Selecting PRINT allows data file printing. When PRINT is selected the computer calls the subroutine SPRINT. The computer prompts "ENTER TEMPERATURE RANGE (LOW,HIGH) (0,10000=WHOLE)". After the operator enters the range, the computer prompts "OUTPUT TO MONITOR (=0) OR PRINTER (=1) (QUIT=2)". Once the output device is selected, the computer prints the data and returns to the menu.

#### H. UPDATE

Selecting UPDATE results in the computer reading and displaying the parameters of the file LD1:FILTMP.DAT on the screen. After each experiment and when the operator exits the program (see EXIT and QUIT, above), the computer writes the current parameters to this file.

## I. RUN

Selecting RUN begins the data acquisition routine. The computer displays the prompt "IS THE TEMPORARY DATA EXPENDABLE (1/0)?". Answering "0" returns the program to the menu. If the data are expendable "1" is entered and data acquisition begins by calling the subroutine PEAKS. PEAKS is the heart of the data acquisition routine. The subroutine PEAKS begins by initializing the array of gain changes, IGA. For each mass I there are 4 values of IGA labeled IGA(I,1) through IGA(I,4). These variables are initially set to 1,0,0,0 (i.e., IGA(I,1)=1, IGA(I,2-4)=0). At the end of the experiment IGA(I,1) contains the final gain code +1 for that mass. A gain of 10, 5, 2 and 1 corresponds to a gain code of 0, 1, 2, and 3, respectively. IGA(I,J) for J=2,3,4 contains the data point number at which the gain changed. For example, imagine an experiment where a single mass I was monitored. The intensity was initially read with a gain of 10, but it switched to a gain of 5 at point 100 because the signal became too large (see below). Later the gain was changed to 2 at point 200, and at point 300 the gain was reduced to 1. The vector IGA(I,1-4) for this experiment is (4,100,200,300), since the final gain is 1 (gain code+1=4) and gain changes occurred at points 100, 200 and 300.

Next, the computer calculates the DAC output for each mass based on the linear relationship between DAC output and mass determined using the SCAN program, described above.

The next step is to set the temperature gain code ITCON to zero, which corresponds to a gain of 10. Now the thermocouple voltage signal is 1000 times its actual value ("DVM" output on the back of the temperature controller already multiplies by 100). When thermocouple voltage measurements are taken later in the experiment, the values are monitored and the computer reduces the gain when the signal reaches 90% of the A/D limit (10 V).

The program then measures the initial temperature. Using the subroutine AREADM the thermocouple voltage is read 20 times from channel 3 with a gain of 10 and the values are stored in the array AINP. The values in AINP are summed, averaged, scaled and converted to a Kelvin temperature.

Millivolt to Kelvin conversion is done with the ITOK subroutine. Three conversion equations are used over the entire temperature range. The equations are listed in Table 4. These equations were derived empirically by fitting thermocouple output and temperature data to polynomials [3].

The point count, SCNT, is set to 1 for the first data point and the data file VMO:TDSTEM.DAT is opened. If there are not 300 blocks of contiguous space in VMO the computer will abort the data acquisition sequence and return to the menu, displaying an error message. If there is enough space to open the file on VMO the program begins the data acquisition loop.

Table 4. Conversion equations for converting thermocouple output T(mV) to Kelvin temperatures T(K)

Temperature Range	Conversion Equation
$T(\text{mV}) < 0$	$T(\text{K}) = 6.12045 \cdot T(\text{mV})^5 + 10.375 \cdot T(\text{mV})^4 +$ $5.8413 \cdot T(\text{mV})^3 - 15.5473 \cdot T(\text{mV})^2 +$ $78.0728 \cdot T(\text{mV}) + 272.8$
$0 \leq T(\text{mV}) \leq 9.2$	$T(\text{K}) = 7.281 \times 10^{-4} \cdot T(\text{mV})^5 - 0.027478 \cdot T(\text{mV})^4 +$ $0.44519 \cdot T(\text{mV})^3 - 4.14974 \cdot T(\text{mV})^2 +$ $74.0594 \cdot T(\text{mV}) + 273.1$
$T(\text{mV}) > 9.2$	$T(\text{K}) = 2.786 \times 10^{-5} \cdot T(\text{mV})^5 - 0.0027614 \cdot T(\text{mV})^4 +$ $0.121904 \cdot T(\text{mV})^3 - 2.43646 \cdot T(\text{mV})^2 +$ $72.9746 \cdot T(\text{mV}) + 257.9$

The data acquisition loop controls the mass spectrometer voltage, measures the ion intensity and measures the sample temperature in a series of eight steps. First, the appropriate DAC output is sent to the mass spectrometer. Second, the computer waits for a specified settling time delay, which is based on the value of RISE. Third, the gain code for ion intensity, ICONV, is set by subtracting 1 from IGA(I,1).

Fourth, the ion intensity is measured to determine which gain code should be used. The subroutine AREADM is used to read channel 0, 50 times, with a gain code ICONV, and the values are stored in AINPUT. The 50 values in AINPUT are summed and averaged and compared with 1840 counts, which is ca. 90% of saturation (2047) counts. If the intensity is less than 1840 counts, the gain code, ICONV, is appropriate for that ion intensity, and the program continues with the fifth step, below.

If the ion intensity is greater than 1840 counts the gain code is increased by 1 (decreasing the gain), IGA(I,1) is decreased by 1, the point at which the decrease in gain occurs is written to IGA(I,2-4) and the intensity is re-read with the new gain setting. If IGA(I,1) is 4 (gain code = 3, gain = 1), the gain cannot decrease further so the program continues. To sum up, in order to continue with data acquisition, the intensity must be less than 1840 counts with a gain code of 10, 5 or 2, or must be read with a gain of 1.

Fifth, the intensity is read again, with AREADM, at channel 0, SMPLS times with a gain code ICONV, and the data are stored in AINP. The values are summed, averaged and written to VMO:TDSTEM.DAT. The program

then repeats the intensity reading sequence (steps four and five, above) for the number of masses specified.

Reading the time, the sixth step, occurs once all the masses are read. The RT-11 subroutine GTIME [4] is used to read the time elapsed since data acquisition began.

The seventh step is reading the sample temperature. Using the AREADM subroutine, 100 thermocouple voltages are read from channel 3 with the gain code ITCON and stored in the array AINP. Since the first values read are often very scattered, the 25th through 90th values are summed and averaged. This method results in less scatter in temperature. The computer converts the average value to millivolts, which is written, along with the previously read time, to the data file.

The eighth step is to convert the thermocouple voltage into degrees Kelvin using the subroutine ITOK. After conversion is complete, the temperature is compared with the end temperature. If the temperature is greater than or equal to the end temperature, the program jumps to the final sequence of data acquisition, described below. If the temperature is less than the end temperature, the program continues by incrementing the point count.

Since the thermocouple voltage is initially read with a gain of 10 (gain code = 0), the gain may need to be decreased during the course of the experiment, as the sample temperature increases. With a gain of 10, the actual temperature is multiplied by 1000, since the DVM output multiplies the signal by 100. Thus, the A/D maximum value of 10 V

corresponds to a sample voltage of 10 mV. To avoid saturating the A/D, the program checks each voltage against 9 mV (800 K) and decreases the gain to 5 when this voltage is reached. With a gain of 5, the voltage is multiplied by 500, and A/D saturation occurs at 20 mV. Thus, the temperature is also checked against 18 mV (1200 K) and the gain is decreased to 2 when the sample voltage reaches 18 mV. With a gain setting of 2, the sample voltage can be reach 50 mV before saturation occurs. Since the melting point of the W-5% Re vs. W-26% Re thermocouple is 2600 K (37 mV) [3], a gain of 2 is adequate for the remainder of the experiment.

When the final temperature is reached, the program jumps out of the data acquisition loop and reads the final time. The data file VMO:TDSTEM.DAT is closed and the file parameters written to LD1:FILTMP.DAT. The program returns from the PEAKS subroutine to line 95 in TDSR, where the SHOW subroutine is called. SHOW updates the menu with the parameters written to LD1:FILTMP.DAT. The program then calls the STORE subroutine, described above. The computer automatically calls the subroutine STORE when data acquisition is completed, so data are stored immediately and not inadvertently destroyed.

#### IV. CONCLUSIONS

Although the PDP-11/23 TDS program is structurally complex, the menu-driven approach makes the program easy to run. By selecting options from the menu, the operator can change file characteristics, write or read data files to or from a disk, plot data or take data besides monitoring multiple masses. The program stores accumulated data on disks for future reference. This type of computer-interfaced approach to the TDS experiment facilitates data acquisition and manipulation enormously.



## V. ACKNOWLEDGEMENTS

This program is a modified version of another program written by Dr. John A. Polta. The assistance of Michael J. Selner, Jr. in modifying the TDS program is sincerely appreciated. We thank Dr. J. T. Lloyd for providing the "SCAN" program.

## VI. REFERENCES

1. P. A. Thiel and T. E. Madey, Surface Science Reports, 7 (1987).
2. H. Herz, H. Conrad and J. Küppers, J. Phys. E, 12 (1979) 369.
3. The temperature and thermocouple output data for W-5% Re vs. W-26% Re thermocouple are found in: (a) D. R. Sandstrom and S. P. Winthrow, J. Vac. Sci. Technol., 14 (1977) 748 (below room temperature) and (b) The 1987 Omega Temperature Measurement Handbook (Omega Engineering, Inc., Stamford, CT, 1987) (above room temperature).
4. RT-11 Programmer's Reference Manual (Digital Equipment Corp., Maynard, MA, 1983).

APPENDIX B:

THE INTERACTION OF  $\text{NF}_3$  WITH  $\text{RU}(001)$ : ORDER AT STEPS

THE INTERACTION OF  $\text{NF}_3$  WITH  $\text{Ru}(001)$ : ORDER AT STEPS

M. M. Walczak<sup>1,2</sup>, A. L. Johnson<sup>1</sup>, P. A. Thiel<sup>2</sup>, and T. E. Madey<sup>1</sup>

<sup>1</sup>Surface Science Division  
National Bureau of Standards  
Gaithersburg, Maryland 20899

<sup>2</sup>Department of Chemistry and Ames Laboratory  
Iowa State University  
Ames, Iowa 50011

This appendix appears in volume 6 of Journal of Vacuum Science and Technology A on pages 675-680, 1988.

## ABSTRACT

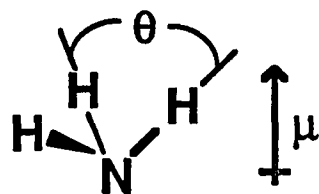
As part of a larger study of small fluorinated molecules on metal and semiconductor surfaces we investigated the adsorption of  $\text{NF}_3$  on Ru(001) using measurements of Electron Stimulated Desorption Ion Angular Distributions (ESDIAD), Low Energy Electron Diffraction (LEED), Thermal Desorption Spectroscopy (TDS) and Auger Electron Spectroscopy (AES). At 100 K,  $\text{NF}_3$  adsorbs with a high sticking probability. Some molecular  $\text{NF}_3$  desorbs on heating, with a peak maximum at 200 K. All molecular desorption is complete by 400 K, but AES shows that nitrogen and fluorine remain on the surface up to 1100 K. The LEED pattern of the majority of the surface remains (1x1) at all coverages and annealing conditions. At most locations on the Ru(001) surface (planar regions), ESDIAD is dominated by  $\text{F}^+$  emission normal to the surface over the temperature range 100-1100 K. On stepped regions of the surface (near edges and defects) highly directional and intense hexagonal patterns of  $\text{F}^+$  emission are observed (200-1100 K). The off-normal beams desorb at  $67 \pm 3^\circ$  away from the surface normal. It appears that most ESDIAD patterns in this system are derived from F or  $\text{NF}_x$  ( $x < 3$ ) fragments.

## I. INTRODUCTION

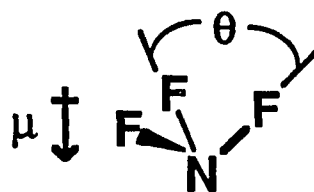
We have investigated the surface chemistry of nitrogen trifluoride ( $\text{NF}_3$ ) on Ru(001) as part of a larger study of small fluorinated molecules on metal and semiconductor surfaces, and as a comparison with previous work on  $\text{NH}_3$  surface chemistry [1-20].

$\text{NH}_3$  chemisorbs on many transition metal surfaces via the nitrogen lone pair electrons [5-18], and adsorption is accompanied by a decrease in work function [1]. Very little decomposition occurs when  $\text{NH}_3$  is adsorbed on Ru(001) [1,7,19], Pt(111) [15], Ni(100) [12], Ni(110) [4], or Ni(111) [8,9], while some  $\text{NH}_3$  decomposition occurs on Al(111) [18], Fe(110) [17] and at steps on the Fe(100) [3,16] surface. Electron Stimulated Desorption Ion Angular Distribution (ESDIAD) studies of  $\text{NH}_3$  on clean Ru(001) [1] show a halo-like pattern of  $\text{H}^+$  ions for low  $\text{NH}_3$  coverages. This indicates that the N-H bond is inclined with respect to the surface normal and the nitrogen end of the molecule is directed toward the surface. On some metal surfaces, including Ru(001) [1,19], the presence of small quantities of oxygen induce azimuthal orientation in adsorbed  $\text{NH}_3$  molecules, resulting in a number of well defined ESDIAD beams [10,11,19].

There are several important differences between  $\text{NH}_3$  and  $\text{NF}_3$ , as shown in Figure 1. The FNF bond angle is  $4.8^\circ$  smaller than the corresponding  $\text{NH}_3$  angle [21,22]. More dramatic is the difference in dipole moments. The  $\text{NH}_3$  molecule is electron rich at the nitrogen end, while the fluorine



$\theta = 107.3^\circ$   
 $\mu = 1.47 \text{ D}$   
 $T_b = 240 \text{ K}$   
**basic**



$\theta = 102.5^\circ$   
 $\mu = 0.234 \text{ D}$   
 $T_b = 66 \text{ K}$   
**non-basic**

Figure 1. Some of the physical differences between NH<sub>3</sub> and NF<sub>3</sub> [4,21,22]

end of  $\text{NF}_3$  is partially negative [3,22]. This fact is manifested in that  $\text{NH}_3$  is a basic molecule (in both the Brønsted and Lewis senses) while  $\text{NF}_3$  is not basic [21].

The surface chemistry of another related molecule, phosphorous trifluoride ( $\text{PF}_3$ ), has been studied on a number of metal surfaces [23-27]. Most recently Alvey et al. have studied the interaction of  $\text{PF}_3$  with Ni(111) [26,27].  $\text{PF}_3$  adsorbs molecularly on Ni(111) at 85 K; a molecular desorption state is observed below 500 K. ESDIAD patterns of  $\text{PF}_3$  on Ni(111) exhibit hexagonal symmetry.  $\text{PF}_3$  molecules decompose on electron beam bombardment, resulting in hexagonal ESDIAD patterns rotated  $30^\circ$  from the original  $\text{PF}_3$  patterns. The surface chemistry of  $\text{PF}_3$  is dominated by the ability of the phosphorous to both donate electrons to the metal (8a orbital) and accept backdonation from the metal (7e orbital) [23-27]. In this way the surface phosphorous trifluoride is stabilized.

Are  $\text{NF}_3$  molecules intact on Ru(001) like  $\text{PF}_3$  molecules on Ni(111)? Is the surface chemistry of  $\text{NF}_3$  dominated by the nitrogen lone pair, as it is for  $\text{NH}_3$ ? Our investigation is aimed at answering these questions. Our experiments combine several surface-sensitive techniques: Thermal Desorption Spectroscopy (TDS) [27], Auger Electron Spectroscopy (AES) [28], Low Energy Electron Diffraction (LEED) [28], and ESDIAD [29]. The ESDIAD method provides direct information about the structure of surface molecules via measurements of the angular distribution of ions ejected from adsorbates during electron beam excitation [28]. The initial ion



trajectory is believed to be along the adsorbate bond vector which is cleaved to create the ion [30-36]. The ejected ions reflect the molecular orientation. Thus, ESDIAD can image the local geometry of the adsorbed  $\text{NF}_3$  molecules and fragments, elucidating the interaction between the molecule and the surface. It is important to note that the polar angle of the exiting ion's trajectory is perturbed by the image force [37] and reneutralization probability [38]. Thus, the observed polar angle of ion desorption differs from the polar angle of the adsorbate bond.

We report evidence that  $\text{NF}_3$  surface chemistry on Ru(001) is significantly different from the surface chemistry of  $\text{NH}_3$  on Ru(001) [1,7,19] and  $\text{PF}_3$  on Ni(111) [26,27]. Some  $\text{NF}_3$  decomposes on clean Ru(001), while little or no decomposition is observed for  $\text{NH}_3$  [1,7,19] or  $\text{PF}_3$  [23,26,27]. In contrast to the  $\text{H}^+$  ESDIAD halo observed for  $\text{NH}_3$  on Ru(001) and the hexagonal  $\text{F}^+$  ESDIAD pattern of  $\text{PF}_3$  on Ni(111),  $\text{NF}_3$   $\text{F}^+$  ESDIAD emission is directed along the surface normal. We find off-normal ion emission only at defect sites near crystal edges or spot welds.

## II. EXPERIMENTAL

The experiments are performed in an all stainless steel UHV chamber equipped with a cylindrical mirror Auger spectrometer, a quadrupole mass spectrometer, and LEED/ESDIAD optics. Ion angular distributions are imaged directly with a microchannel plate multiplier and a phosphor screen.

The details of the video data acquisition system are reported elsewhere [39]. The ESDIAD patterns can be either recorded in real time on videotape for later digitization or input directly into a computer. The electron energy in the ESDIAD experiments is 310 eV, which includes a 160 eV compression bias voltage applied to the sample [30,31]. The ion masses are determined by rotating the sample to face the mass spectrometer, located near the LEED/ESDIAD optics [40], and detecting the ion emission with the mass spectrometer ionizer off. The electron beam diameter is 0.3 mm; the current density for both ESDIAD and LEED is 6  $\mu\text{A}/\text{cm}^2$ .

Moving the electron beam, either by changing the voltage on the deflection plates or by translating the crystal, allows bombardment of the entire crystal surface. In this way we are able to observe ESDIAD/LEED patterns of the majority (flat) regions and minority (defect) regions.

The 5 mm by 8 mm Ru(001) crystal is aligned and polished to within  $\pm 0.5^\circ$  of the (001) face. The crystal is spot welded to two 0.020 inch Ta

wires which are attached to a rotatable feedthrough allowing resistive heating and liquid nitrogen cooling to 100 K. A W-5% Re vs. W-26% Re thermocouple is spotwelded to the back of the crystal. The crystal is cleaned initially by argon ion bombardment and heating both in oxygen and in vacuum [41]. The criteria for a clean surface are the disappearance of the oxygen Auger signal at temperatures between 1500-1600 K [42] and the absence of any N or F Auger signal. Based on these Auger criteria, the surface is cleaned sufficiently between  $\text{NF}_3$  experiments by heating in vacuum to 1600 K. After cleaning the surface in this manner there is no detectable ESDIAD emission.

The etchant grade  $\text{NF}_3$  is supplied from Air Products, Inc. [43] and used without further purification. To avoid contamination of the gas handling manifold, an independent dosing line is used for  $\text{NF}_3$ . After extensive conditioning of the handling line, the  $\text{NF}_3$  mass spectrum agrees with published spectra [44].  $\text{NF}_3$  is introduced into the chamber by a directed doser [40] consisting of a 6 mm o.d. stainless steel tube connected to the high vacuum side of a leak valve. The tube outlet is flared to 1 cm in diameter and is 1 cm away from the sample. The  $\text{NF}_3$  exposures reported here, in Langmuir ( $1 \text{ L} = 1 \times 10^{-6} \text{ Torr*s}$ ), are the product of uncorrected ion gauge pressure and time. The reported exposures are lower than actual exposures due to the high local pressure at the sample. We estimate that the actual  $\text{NF}_3$  exposures are 30 times higher than the apparent (reported) exposures. An exposure begins after the gas flow is started, when the sample is rotated to face the doser.

After the required time elapses the sample is rotated away and the gas flow is stopped. During a typical experiment the background pressure returns to its original value within 30 to 60 seconds.

The Auger data are reported as peak height ratios (N or F to Ru). The Auger spectra are recorded with a 0.1 to 1  $\mu\text{A}$  beam current and 3 kV beam voltage. Since fluorine-containing molecules are often extremely sensitive to electron beam damage, the 647 eV fluorine signal is recorded first, the 379 eV nitrogen signal is recorded next, and the 273 eV ruthenium signal is recorded last. We find the fluorine Auger signal unusually stable in this case. After 9 minutes of electron beam bombardment the fluorine Auger signal is still ca. 70% of its original height. Since the nitrogen peak lies near a Ru diffraction feature, the nitrogen height is difficult to measure reliably. For these reasons the coverage data are based on the F/Ru Auger ratio. For the temperature dependence studies, both F/Ru and N/Ru ratios are reported since the two would not necessarily change in the same way or at the same rate in cases involving decomposition.

### III. RESULTS

#### A. Auger Uptake Curves

The Auger F/Ru ratios as a function of  $\text{NF}_3$  exposure are shown in Figure 2. In the low exposure regime, shown in Figure 2a, saturation occurs by 0.05 apparent Langmuir. The low exposure required for saturation implies a high sticking coefficient for  $\text{NF}_3$  on Ru(001) at 100 K. Higher exposures (Figure 2b) confirm that the surface is saturated after only ca. 0.05 apparent L. This indicates that no  $\text{NF}_3$  multilayer forms, as expected, since the vapor pressure of  $\text{NF}_3$  is about 10 Torr at 100 K [22].

#### B. Thermal Desorption Spectroscopy

Figure 3 shows thermal desorption spectra for  $\text{NF}_3$  from Ru(001). Mass 52 ( $\text{NF}_2^+$ ) is the most intense peak in the  $\text{NF}_3$  cracking pattern [44]. The parent mass (mass 71 =  $\text{NF}_3^+$ ), monitored in other experiments, is found to follow the mass 52 fragment. The peak maximum occurs at ca. 200 K; all molecular desorption is complete by 400 K. The exposures shown here (0.02 and 0.10 apparent L) are near and above saturation, respectively, as indicated in the Auger experiments. The 0.02 apparent L peak area represents 60% of the 0.10 apparent L peak area. No mass 19 ( $\text{F}^+$ ) desorbs above background at any temperature up to 1600 K.

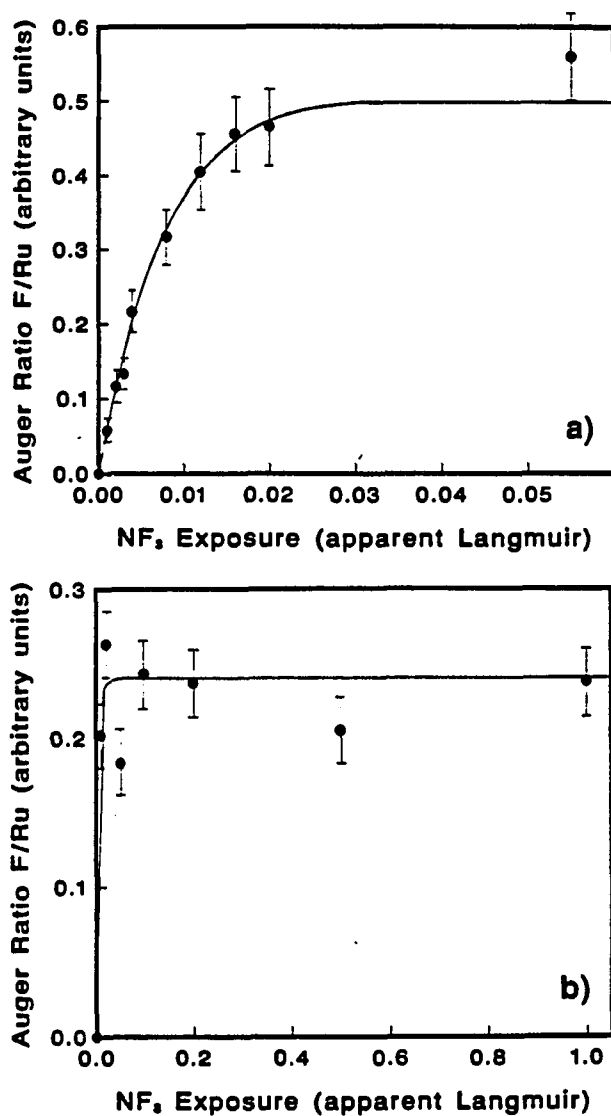


Figure 2. F/Ru Auger peak ratios as a function of  $\text{NF}_3$  exposure

- (a) F/Ru Auger peak ratios as a function of  $\text{NF}_3$  exposure in a low exposure regime.
- (b) F/Ru Auger peak ratios as a function of  $\text{NF}_3$  exposure over the entire exposure regime.

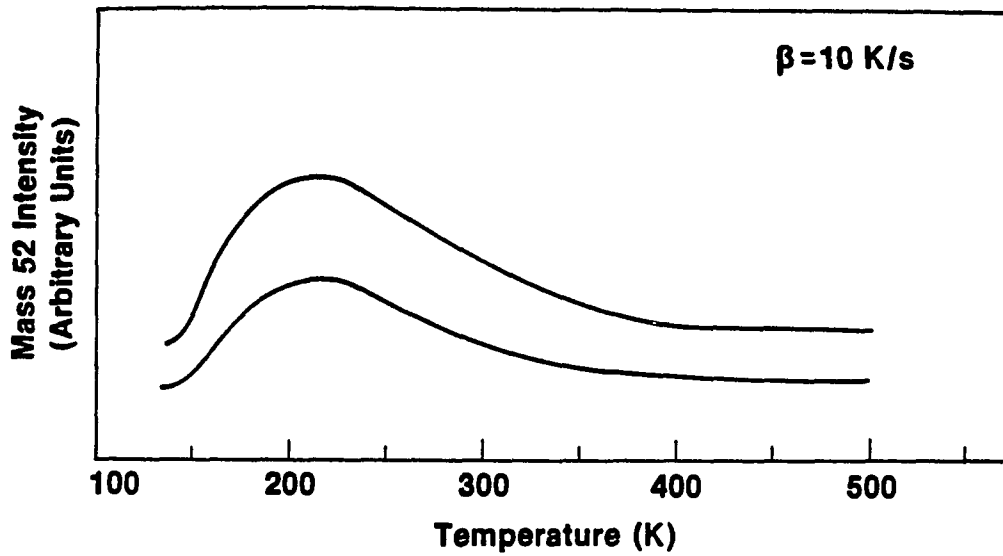


Figure 3. Thermal desorption of  $\text{NF}_3$  from  $\text{Ru}(001)$

The lower curve represents 0.02 apparent Langmuir  $\text{NF}_3$  while the upper curve follows a 0.10 apparent Langmuir exposure.

### C. Auger Temperature Dependence

Data illustrating the temperature dependence of the Auger signals for F and N are plotted in Figure 4. After an initial 0.02 apparent L  $\text{NF}_3$  exposure the sample is heated to the indicated temperature and allowed to cool to 100 K. The three Auger peaks are then recorded (F, N, Ru) and the sample is heated to the next temperature. For each data point the crystal is moved so that a new spot is sampled by the Auger electron beam. Both the N/Ru and F/Ru ratios decrease by ca. 60% on heating to 200 K. Since this is the temperature range where thermal desorption occurs, we estimate that 50% of the  $\text{NF}_3$  molecules desorb molecularly. After the initial drop, the Auger ratios remain constant until about ca. 600-700 K where the signal falls off.

### D. LEED

For all the  $\text{NF}_3$  exposures and all annealing conditions, the LEED pattern of the majority of the surface is (1x1). Near the edges of the crystal and in the regions of spotwelds the LEED pattern contains extra spots, which we attribute to steps in the damaged areas. Less than 10% of the surface shows defective LEED patterns. Extra spots corresponding to steps in all three domains of the (001) surface are observed at different positions in the defect region. Alternatively, the spots could result from impurities, but Auger analyses in the damaged regions show no detectable impurity signal.



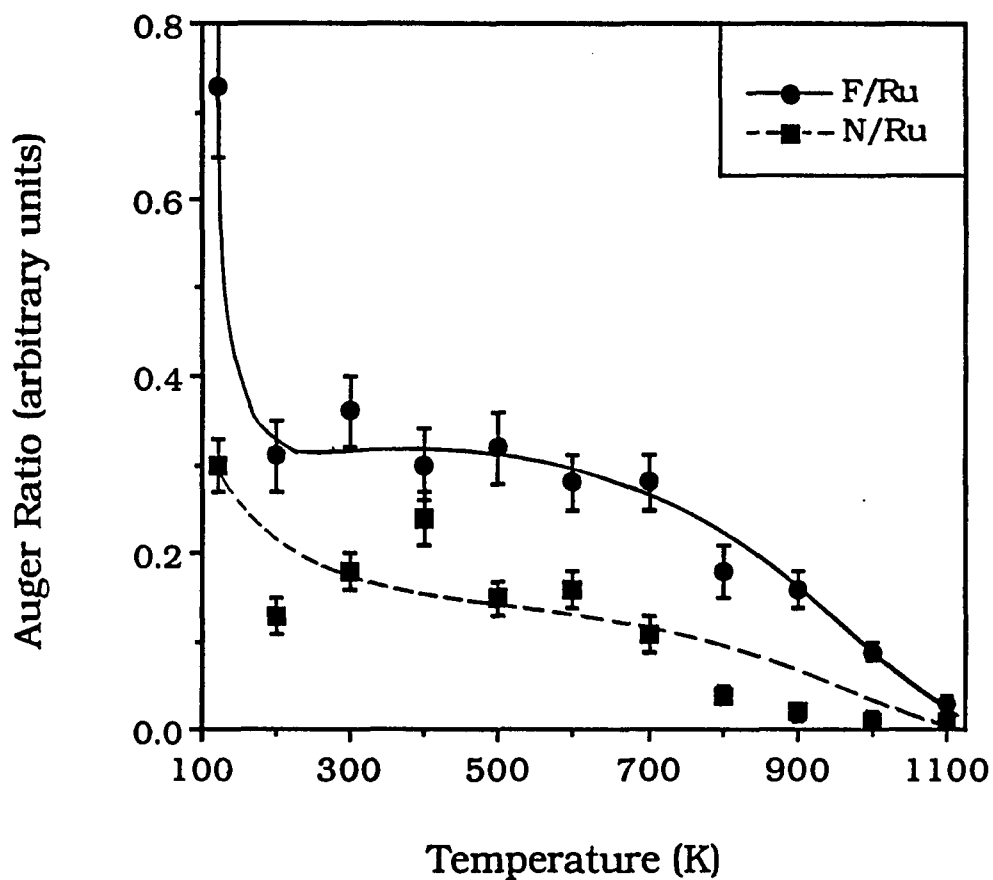


Figure 4. F/Ru and N/Ru Auger peak ratios as a function of temperature. Each data point represents a different spot on the crystal and follows cooling to 100 K.

### E. ESDIAD

The ESDIAD pattern of the  $F^+$  ions shown in Figure 5 is representative of all  $NF_3$  exposures at 100 K. This normal emission pattern is observed on the majority (flat regions) of the crystal. Annealing to 200 K decreases the intensity of the patterns slightly (see below) but does not change the overall appearance. The pattern disappears upon heating above 1100 K.

The  $F^+$  ESDIAD pattern for the defective areas is shown in Figure 6a and b. This hexagonal pattern is observed after heating to 300 K, and also persists to 1100 K. Before annealing to 300 K the pattern is hexagonal but the beams are not resolved. The angle between the outer beams and the surface normal is  $67 \pm 3^\circ$ . The angle determination is done under zero field conditions, and angles are measured by rotating the crystal to center the ion beam on the optics. The hexagonal pattern exhibits a reversible temperature dependence [45], both in beam widths and relative intensities. This phenomenon is a consequence of temperature-dependence of the vibrational amplitudes of the surface species.

Both the normal beam of Figure 5 and hexagonal pattern of Figure 6a and b persist up to 1100 K. In Figure 7 the maximum ESDIAD ion intensity of the normal F beam observed for the Ru(001) terraces is plotted as a function of temperature. For each data point the sample is heated to the indicated temperature, held for 5 seconds, cooled to 100 K, and then the ion intensity is measured using the video data system. A small intensity

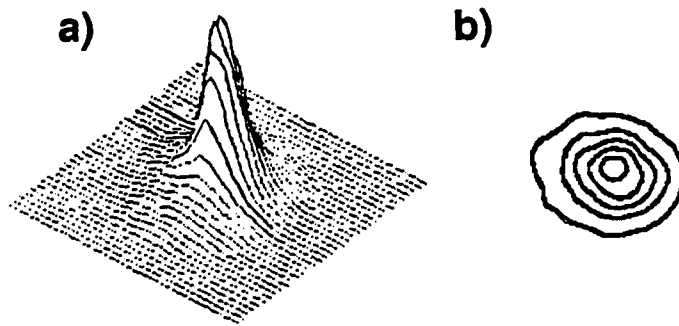


Figure 5.  $F^+$  ESDIAD image on the crystal terraces

Part (a) is a perspective plot of the  $F^+$  ESDIAD image; part (b) is a contour plot.

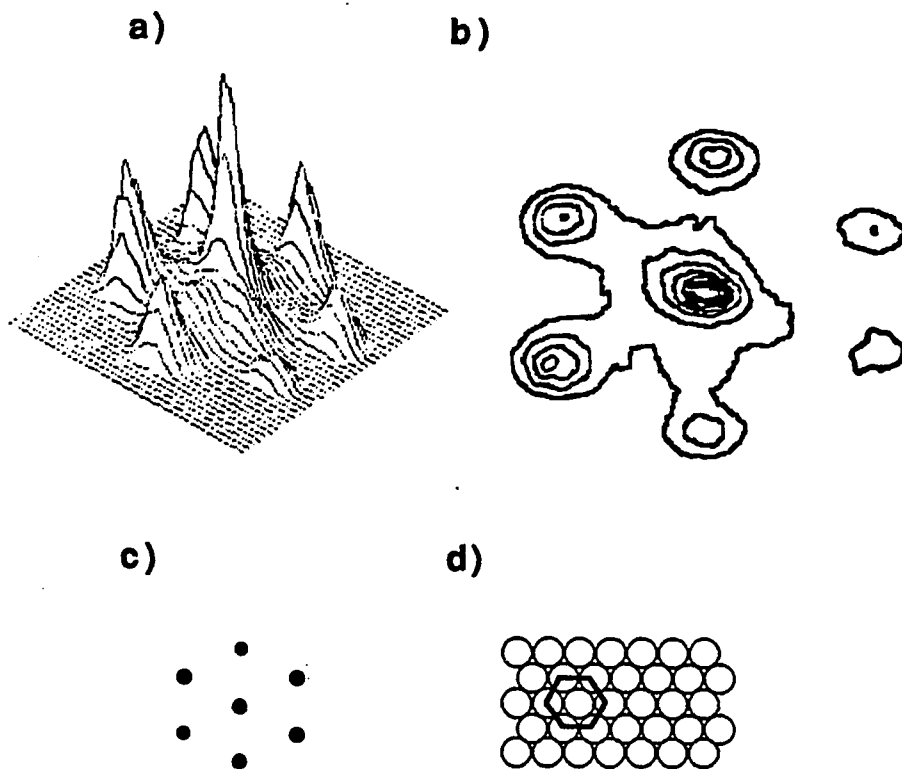


Figure 6.  $F^+$  ESDIAD image on the damaged areas of the crystal

Part (a) is a perspective plot of the  $F^+$  ESDIAD image; part (b) is a contour plot. In this ESDIAD pattern there is a 50-75% decrease in gain in the ESDIAD optics toward the lower right. This effect is an artifact of the optics and not due to adsorbate structure. Part (c) is a representation of the (1x1) LEED pattern of Ru(001) crystal (reciprocal space). Part (d) corresponds to the real space crystal lattice.

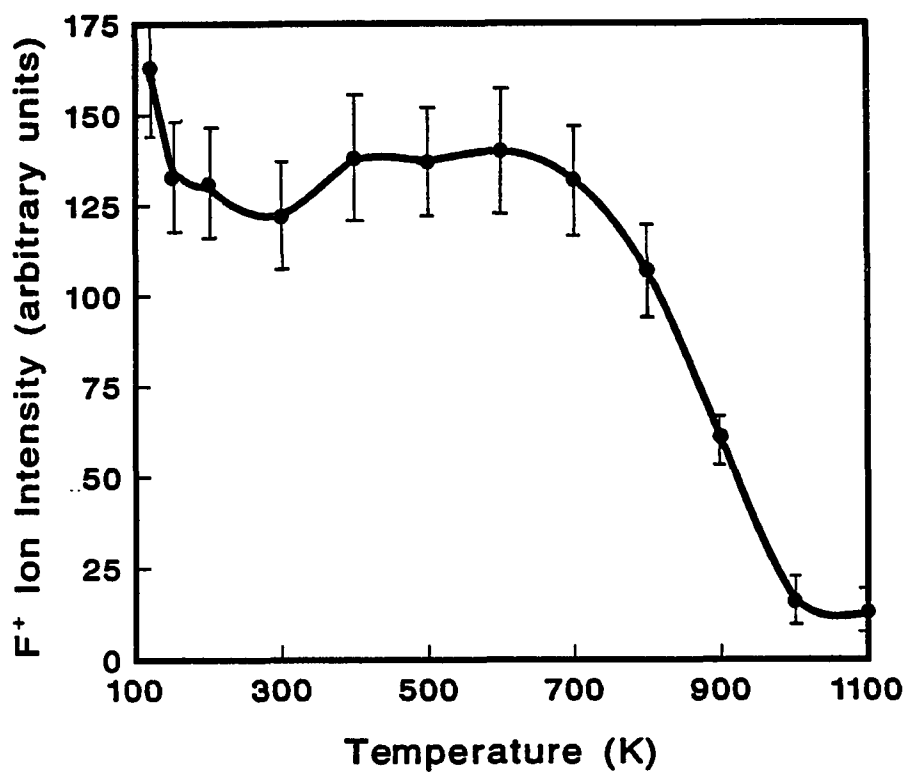


Figure 7. ESDIAD F<sup>+</sup> ion intensity as a function of temperature

The data points are taken after cooling to 100 K. The data shown in this Figure are for the normal F<sup>+</sup> beam associated with the Ru(001) terraces.

decrease is observed between 100 and 200 K. The maximum intensity remains constant until about 700 K where it falls off. In a retarding field ion energy study, the  $F^+$  ions are shown to have ca. 6 eV kinetic energy.

#### F. Coadsorption with Oxygen

Experiments have been performed to see if oxygen coadsorption leads to a preferred azimuthal orientation of  $NF_3$  molecules in ESDIAD. These studies are motivated by previous experiments involving  $NH_3$  and oxygen on metals, in which the impurity oxygen orients the  $NH_3$  molecules so the N-H bond vectors are along specific azimuths of the substrate [10,11,18,19,46]. After a 0.3 L oxygen exposure to the surface, no  $NF_3$  adsorbs as indicated by the lack of an ESDIAD pattern and the absence of a N or F Auger peak. After dosing 0.1 L oxygen and annealing to 300 K,  $NF_3$  does adsorb. A centro-symmetric (normal emission) ESDIAD pattern is observed on dosing at 100 K both on the flat and defective regions before annealing. After annealing to 300 K the hexagonal pattern appears around the edges of the crystal in the defect region. This pattern has the same appearance as the one shown in Figure 6a and b. After prolonged electron beam exposure, the hexagonal ESDIAD pattern appears over the entire surface, accompanied by a (2x2) LEED pattern.

## IV. DISCUSSION

Taken together, the AES, TDS and ESDIAD data indicate that a substantial fraction of  $\text{NF}_3$  dissociates and that molecular fragments remain on the surface up to 1100 K. At exposures greater than 0.005 apparent Langmuir a molecular state is seen in TDS. The disappearance of the N and F Auger signals between 600-1100 K is consistent with desorption of nitrogen [47-50] and fluorine [51,52] from metal surfaces.

On the terraces, normal emission of  $\text{F}^+$  ions suggest the adsorbate is F atoms or NF fragments. The rich order in the defect regions is explained by F atoms, NF and/or  $\text{NF}_2$  fragments. Figure 8 shows several bonding mode possibilities. The hexagonal ESDIAD ion beams are in the same spatial arrangement as the (1x1) LEED beams. Since ESDIAD images are in real space while LEED patterns are in reciprocal space, the azimuths of ion beams are rotated  $30^\circ$  from the underlying lattice (see Figure 6c and d) and pointed perpendicular to Ru step edges. Highly ordered ESDIAD patterns in the defect regions of the sample suggest a stabilization of  $\text{NF}_x$  fragments at steps. A few possible arrangements are illustrated in Figure 8. Off-normal  $\text{F}^+$  emission is possible for  $\text{F}^+$  atoms or NF fragments inclined at steps. The normal emission observed in the center of the hexagonal pattern could be due to  $\text{NF}_2$  fragments at step edges or on the terrace regions near the steps.

The polar angle of the hexagonal pattern,  $67 \pm 3^\circ$ , is large. Because post-ionization effects distort the trajectories of the ion





angular distributions (image force, reneutralization) [34,37,38], we do not relate the measured desorption angle,  $67 \pm 3^\circ$ , to the surface polar bond angle quantitatively.

It should be noted from the data in Figures 4 and 7 that the F/Ru Auger and  $F^+$  ESDIAD ion intensities have similar temperature dependencies. This supports the contention that the ESDIAD pattern on the terraces indeed represents majority species, not minority states. Assuming the AES cross sections for  $NF_3$  molecules and fragments are equivalent, comparison of these Figures illustrates that the ESDIAD  $F^+$  cross section for molecular  $NF_3$  is significantly smaller than for  $NF_3$  fragments. On heating to 200 K the  $F^+$  ion intensity drops to about 80% of the initial value, while the F/Ru Auger ratio drops to ca. 40% of the initial value in the same temperature range.

The oxygen coadsorption results indicate no coadsorption induced orientation, in contrast to the  $NH_3$  systems [10,11,18,19,46]. We note, however, that on the oxidized and annealed  $NF_3$  covered surface, the hexagonal pattern is observed over the entire surface after prolonged electron beam exposure. The observation of the hexagonal pattern on the terraces suggests that oxygen stabilizes a different decomposition product than on the clean surface. The most obvious product is  $NF_2$  fragments, since a hexagonal pattern is easily formed if the nitrogen bonds to the surface leaving the two fluorine atoms directed away from the surface. If the fluorine atoms in  $NF_2$  are positioned between adjacent Ru atoms in the three possible orientations, an ESDIAD hexagon,

having the orientation of Figure 6b, is expected. This structure also accounts for the coincidence of the real space ESDIAD pattern and the reciprocal space LEED pattern (see Figures 6c and d). The normal component of the pattern could result from some NF fragments or F atoms on the surface. Either a steric or an electronic effect could cause this change in the surface chemistry of  $\text{NF}_3$ . Oxygen may occupy sites active in the decomposition pathway which occurs on the clean surface. Alternatively, the presence of electronegative oxygen can deplete electron density at decomposition sites. Our results cannot distinguish between these two cases. The presence of oxygen does not appear to affect the decomposition of  $\text{NF}_3$  at the steps.

Our results point to a strong contrast in the surface chemistry of  $\text{NF}_3$  on Ru(001),  $\text{NH}_3$  on Ru(001) [1,7,19] and  $\text{PF}_3$  on Ni(111) [26,27]. About 50% of the  $\text{NF}_3$  molecules dissociate on adsorption on Ru(001) at 100 K, and the dissociation fragments are the source of most of the ESDIAD patterns. Our results indicate that  $\text{NF}_3$  molecules decompose on the surface leaving F, NF, or  $\text{NF}_2$  fragments. Little or no  $\text{NH}_3$  decomposition is observed on Ru(001) [1,7,19];  $\text{PF}_3$  remains molecular on Ni(111) [26,27]. In the  $\text{NF}_3$  case, a centro-symmetric normal emission  $\text{F}^+$  ESDIAD pattern is seen over the majority of the surface. With low  $\text{NH}_3$  coverages on Ru(001) a halo  $\text{H}^+$  ESDIAD pattern is observed [1]. A hexagonal  $\text{F}^+$  ESDIAD pattern is seen for  $\text{PF}_3$  on Ni(111) [26,27]. The differences in the surface chemistry of  $\text{NF}_3$  and  $\text{NH}_3$  undoubtedly relate to the different chemical properties illustrated in Figure 1, particularly the relative

dipole moments. For  $\text{NF}_3$ , bonding to the surface through the nitrogen is less favorable since there is a depletion of electron density at the nitrogen lone pair, relative to  $\text{NH}_3$ . The differences in the surface chemistry of  $\text{NF}_3$  on  $\text{Ru}(001)$  and  $\text{PF}_3$  on  $\text{Ni}(111)$  are probably primarily due to differences in the molecular orbitals of the two adsorbates.

## V. CONCLUSIONS

We find that  $\text{NF}_3$  adsorbs with high sticking probability on Ru(001) at 100 K. For a saturated  $\text{NF}_3$  layer about half of the fluorine desorbs as molecular  $\text{NF}_3$  between 100-400 K. Decomposition fragments remain on the surface to 1100 K. The LEED pattern of both the clean and adsorbate-covered Ru(001) shows evidence of steps near spotwelds and edges (i.e., in the regions of the hexagonal ESDIAD pattern). On the terraces, the LEED pattern is (1x1) at all coverages and annealing conditions. Only  $\text{F}^+$  ions are detected desorbing from the surface during electron bombardment. There are two characteristic ESDIAD patterns. The first pattern, centro-symmetric normal emission, is seen on the majority of the (smooth) surface, and is due to adsorption of  $\text{NF}_3$  and molecular fragments on the planar terraces. The second pattern, consisting of seven well-defined beams arranged in a filled hexagon, occurs in damaged regions of the crystal after heating to 200 K; this pattern is due to molecular fragments ( $\text{F}$ ,  $\text{NF}_x$ ) adsorbed at step sites. The off-normal beams of the seven beam hexagonal pattern arise from  $\text{F}^+$  ions desorbing  $67 \pm 3^\circ$  from the surface normal.

The surface chemistry of  $\text{NF}_3$  on Ru(001) is significantly different from  $\text{NH}_3$  on Ru(001) and  $\text{PF}_3$  on Ni(111). The difference in the surface chemistry of these molecules is not surprising: although these molecules are structurally similar, they are chemically very different.

## VI. ACKNOWLEDGEMENTS

This work was performed at the National Bureau of Standards. Ames Laboratory is operated for the U.S. Department of Energy by Iowa State University under contract number W-7405-ENG-82. This research has been supported by the Office of Basic Energy Sciences, Department of Energy.

## VII. REFERENCES

1. C. Benndorf and T. E. Madey, *Surface Science*, 135 (1983) 164.
2. T. E. Madey, C. Benndorf and S. Semancik, in: Kinetics of Interface Reactions Vol. 8, Eds. M. Grunze and H. J. Kreuzer (Springer, Berlin, 1987) 175.
3. C. Benndorf, T. E. Madey and A. L. Johnson, *Surface Science*, 187 (1987) 434.
4. K. Jacobi, E. S. Jensen, T. N. Rhodin and R. P. Merrill, *Surface Science*, 108 (1981) 397.
5. T. E. Madey and J. T. Yates, Jr., in: Proceedings of the 7th International Vacuum Congress and 3rd International Conference on Solid Surfaces Eds. R. Dobrozemsky, F. Rudenaüer, F. P. Ziehböck and A. Breth (Burger, Vienna, 1977) 1183.
6. L. R. Danielson, M. J. Dresser, E. E. Donaldson and J. T. Dickinson, *Surface Science*, 71 (1978) 599.
7. L. R. Danielson, M. J. Dresser, E. E. Donaldson and D. R. Sandstrom, *Surface Science*, 71 (1978) 615.
8. T. E. Madey, J. E. Houston, C. W. Seabury and T. N. Rhodin, *J. Vacuum Sci. Technol.*, 18 (1981) 476.
9. C. W. Seabury, T. N. Rhodin, R. J. Purtell and R. P. Merrill, *Surface Science*, 93 (1980) 117.
10. F. P. Netzer and T. E. Madey, *Phys. Rev. Lett.*, 47 (1981) 928.
11. F. P. Netzer and T. E. Madey, *Surface Science*, 119 (1982) 422.

12. M. Grunze, P. A. Dowben and C. R. Brundle, *Surface Science*, 128 (1983) 311.
13. G. B. Fisher and G. E. Mitchell, *J. Elec. Spec. Rel. Phen.*, 29 (1983) 253.
14. R. J. Purtell, R. P. Merrill, C. W. Seabury and T. N. Rhodin, *Phys. Rev. Lett.*, 44 (1980) 1279.
15. G. B. Fisher, *Chem. Phys. Lett.*, 79 (1981) 452.
16. M. Grunze, F. Bozso, G. Ertl and M. Weiss, *Appl. Surface Science*, 1 (1978) 241.
17. M. Weiss, G. Ertl and F. Nitschke, *Appl. Surface Science*, 2 (1979) 614.
18. F. P. Netzer and T. E. Madey, *Chem. Phys. Lett.*, 88 (1982) 315.
19. C. Benndorf and T. E. Madey, *Chem. Phys. Lett.*, 101 (1983) 59.
20. M. Grunze, in: The Chemical Physics of Solid Surfaces and Heterogenous Catalysis Vol. 4, Eds. D. A. King and D. P. Woodruff (Elsevier, New York, 1982) 143.
21. W. R. Jolly, The Inorganic Chemistry of Nitrogen (W. A. Benjamin, Inc., New York, 1964) 47.
22. R. C. Weast and M. J. Astle, Eds., CRC Handbook of Chemistry and Physics 62nd edition (Chemical Rubber Publishing Company, Boca Raton, FL, 1981).
23. F. Nitschké, G. Ertl and J. Küppers, *J. Chem. Phys.*, 74 (1981) 5911.
24. G. Ertl, J. Küppers, F. Nitschké and M. Weiss, *Chem. Phys. Lett.*, 52 (1977) 309.

25. G. Blyholder and R. Sheets, *J. Colloid Interface Sci.*, 46 (1974) 380.
26. M. D. Alvey, J. T. Yates, Jr. and K. J. Uram, *J. Chem. Phys.*, 87 (1987) 7221.
27. M. D. Alvey and J. T. Yates, Jr., *J. Am. Chem. Soc.*, 110 (1988) 1782.
28. Thermal Desorption Spectroscopy Review: D. A. King, *Surface Science*, 47 (1975) 384. Electron Spectroscopies Review: G. Ertl and J. Küppers, *Low Energy Electrons and Surface Chemistry* (Verlag Chemie, Weinheim, 1974).
29. T. E. Madey, D. E. Ramaker and R. Stockbauer, *Ann. Rev. Phys. Chem.*, 35 (1984) 215.
30. J. J. Czyzewski, T. E. Madey and J. T. Yates, Jr., *Phys. Rev. Lett.*, 32 (1974) 777.
31. T. E. Madey and J. T. Yates, Jr., *Surface Science*, 63 (1977) 203.
32. T. E. Madey in: *Inelastic Particle-Surface Collisions* Eds. W. Heiland and E. Taglauer (Springer-Verlag, Berlin, 1981) 80.
33. T. E. Madey, F. P. Netzer, J. E. Houston, D. M. Hanson and R. Stockbauer in: *Desorption Induced by Electronic Transitions DIET-I* Eds. N. H. Tolk, M. M. Traum, J. C. Tully and T. E. Madey (Springer Verlag, Heidelberg, 1983) 120.
34. T. E. Madey, C. Benndorf, N. Shinn, Z. Misković and J. Vukanić, in: *Desorption Induced by Electronic Transitions DIET-II* Eds. W. Brenig and D. Menzel (Springer-Verlag, Heidelberg, 1985) 104.



35. T. E. Madey, *J. Vacuum Sci. Technol.*, A4 (1986) 257.
36. T. E. Madey, *Science*, 234 (1986) 316.
37. Z. Misković, J. Vukanić and T. E. Madey, *Surface Science*, 169 (1986) 405.
38. Z. Misković, J. Vukanić and T. E. Madey, *Surface Science*, 141 (1984) 285.
39. A. L. Johnson, R. Stockbauer, D. Barak and T. E. Madey, in: Desorption Induced by Electronic Transitions DIET-III Eds. M. Knotek and R. Stulen (Springer Verlag, New York, 1988) 130.
40. A. L. Johnson, M. M. Walczak and T. E. Madey, *Langmuir*, 4 (1988) 277.
41. E. D. Williams and W. H. Weinberg, *Surface Science*, 82 (1979) 93.
42. T. E. Madey, H. A. Engelhardt and D. Menzel, *Surface Science*, 48 (1975) 304.
43. Specification of the manufacturer is included to specify experimental conditions and does not imply endorsement of the product by NBS.
44. S. R. Heller and G. W. A. Milne, EPA/NIH Mass Spectral Data Base NSRDS-NBS63, Vol. 1 (U.S. Government Printing Office, Washington, D. C., 1978).
45. T. E. Madey, M. Polak, A. L. Johnson and M. M. Walczak, in Desorption Induced by Electronic Transitions DIET III Eds. M. Knotek and R. Stulen (Springer Verlag, New York, 1988) 120.
46. T. E. Madey and C. Benndorf, *Surface Science*, 152/153 (1985) 587.

47. K. L. Shanahan, Ph.D. Thesis, University of California, Berkeley, 1984.
48. M. Grunze, R. K. Driscoll, G. N. Burland, J. C. L. Cornish and J. Pritchard, *Surface Science*, 89 (1979) 381.
49. C. Egawa, T. Nishida, S. Naito and K. Tamaru, *J. Chem. Soc. Faraday Trans. 1*, 80 (1984) 1595.
50. J. E. Parmenter and W. H. Weinberg, *J. Am. Chem. Soc.*, 110 (1988) 7583.
51. E. Bechtold and H. Leonard, *Surface Science*, 151 (1985) 521.
52. E. Bechtold, *Appl. Surface Science*, 7 (1981) 231.

## ACKNOWLEDGEMENTS

I am grateful for all the guidance and support my research advisor, Professor Patricia A. Thiel, has given me over the last four and a half years. I sincerely appreciate her inexhaustible patience in reading manuscripts.

I have enjoyed being a member of the Thiel group. I am especially indebted to Dr. Sheng-Liang Chang, Mike Columbia, Dr. Jim Dyer, Pam Leavitt, Dr. Wai-Yan Leung, Barb Nielsen, Diane Sanders and Pete Schmitz for graciously offering assistance when requested.

I especially thank the group bakers Mike Columbia, Pam Leavitt and Barb Nielsen whose chocolate creations have beckoned me away from my work countless times.

I appreciate the companionship and unending patience of Daniel E. Walczak. I am grateful for the moral support of my family: Mom, Dad, Mike, Dan, Kirsten, Greg, Aimee and Beth Selner. They have helped me keep the important things in life in perspective. The friendship of Diane and David Sanders has made the last five years enjoyable.

I am grateful for the opportunity to spend the spring of 1987 working with Dr. Theodore E. Madey and Dr. Allen L. Johnson at the National Bureau of Standards in Gaithersburg, Maryland. Under the guidance of Drs. Madey and Johnson I learned the art of ESDIAD experiments. I am deeply indebted to Allen, a truly exceptional scientist, for teaching me how to approach problems in new ways.

I thank the Procter and Gamble Companies for financial support.

This work was performed at Ames Laboratory under contract No. 7405-ENG-82 with the U.S. Department of Energy. The United States government has assigned the DOE Report number IS-T-1386 to this dissertation.